

Fatima-GB: Searching Clarity within Marine Fog

H.J.S. Fernando¹, C. Dorman¹³, E. Pardyjak¹⁶, L. Shen¹⁵, Q. Wang⁷, E. Creegan³, S. Gaberšek⁸, I. Gulpepe^{1,11}, S. Hoch¹⁶, L. Lenain¹³, D. Richter¹, R. Chang⁵, T.C. VandenBoer¹⁷, S. Bardeel¹, A. Barve¹⁵, B. Blomquist⁹, T. Bullock⁶, Z. Chen¹⁷, L. Colosi¹³, R.S. Coppersmith¹, I. Crawford¹⁴, L.R. Crilley¹⁷, R. Dimitrova¹, A. Dowling¹, D. Eleuterio¹⁰, S. Fiorino², M. Gallagher¹⁴, N. Gapp¹², G. Giacosa⁵, A. Grachev³, L. Grare¹³, T. Hintz¹, C. Hocut³, K.Y. Huang¹, O. Hyde¹, K. Keefer², D.G. Ortiz-Suslow⁷, A. Perelet¹⁶, W. Perrie⁴, J. Ruiz-Plancarte⁷, L. Salehpoor¹⁷, D. Singh¹⁶, N. Statom¹³, P. Taylor¹⁷, S. Wang¹, R. Yamaguchi⁷



¹University of Notre Dame, Notre Dame, IN 46556, USA

²Air Force Institute of Technology, Wright Patterson Air Force Base, Dayton, OH 45433, USA

³Army Research Laboratory, White Sands Missile Range, NM 88002, USA

⁴Bedford Institute of Oceanography, Dartmouth, NS B2Y 4A2, Canada

⁵Dalhousie University, Halifax, NS B3H 4R2, Canada

⁶Digital Environment, WSP Canada Inc., St. John's, Newfoundland & Labrador, A1B 3X4, Canada

⁷Naval Postgraduate School, Monterey, CA 93943, USA

⁸Naval Research Laboratory, Monterey, CA 93943, USA

⁹NOAA Physical Sciences Laboratory, Cooperative Institute for Research in Environmental Sciences, University of Colorado, Boulder, CO 80305, USA

¹⁰Office of Naval Research, Arlington, Virginia, VA 22203-1995, USA

¹¹Ontario Technical University, Oshawa, ON L1G 0C5, Canada

¹²Science Applications International Corporation (SAIC), San Diego, CA

¹³Scripps Institution of Oceanography and University of California, San Diego, CA 92037

¹⁴University of Manchester, Manchester, M13 9PL, UK

¹⁵University of Minnesota, Minneapolis, MN 55414, USA

¹⁶University of Utah, Salt Lake City, UT 84112, USA

¹⁷York University, Toronto ON, M3J 1P3, Canada

Corresponding Author:

Harindra J.S. Fernando

Departments of Civil and Environmental Engineering and Earth Sciences,
and Aerospace and Mechanical Engineering

University of Notre Dame, Notre Dame, IN 46556

Phone: 574-631-9346; Fax: 574-631-9236

e-mail: fernando.10@nd.edu

1

Early Online Release: This preliminary version has been accepted for publication in *Bulletin of the American Meteorological Society*, may be fully cited, and has been assigned DOI 10.1175/BAMS-D-23-0050.1. The final typeset copyedited article will replace the EOR at the above DOI when it is published.

© 2025 American Meteorological Society. This is an Author Accepted Manuscript distributed under the terms of the default AMS reuse license. For information regarding reuse and general copyright information, consult the AMS Copyright Policy (www.ametsoc.org/PUBSReuseLicenses).

Abstract

Fog constitutes a thick, opaque blanket of air hugging the Earth's surface, laden with small water droplets or ice crystals. Fog disrupts transportation, poses security threats, disorients human perception and impacts communications and ecosystems. Collusion of atmospheric, terrestrial and hydrologic processes produces fog droplets that pullulate over hygroscopic aerosols that act as condensation nuclei. Marine fog is particularly complex, since underlying dynamic, thermodynamic and (bio)physicochemical processes span fifteen decades of spatial scales, from megameter-sized synoptic weather systems to nanometer-scale bioaerosols. This paper overviews the first international field campaign (Fatima-GB) of the project dubbed Fatima (Fog and turbulence interactions in the marine atmosphere) conducted during 01-31 July, 2022 in the Grand Banks region of North Atlantic. Therein, weather systems and commingling cold and warm oceanic waters provide entrée for fog genesis. Measurement platforms included an islet southwest of Nova Scotia (Sable Island), a research vessel (Atlantic Condor), an offshore Oil Platform and autonomous surface vehicles. The instrument array comprised of extant remote and in-situ sensors augmented by novel sensing systems prototyped and deployed in marine fog to penetrate the smallest scales of turbulence, examine aerosols, and quantify radiation budget. The comprehensive data set so gathered, together with satellite and reanalysis products, mesoscale-model and large-eddy simulations demonstrated that the long-held hypotheses of marine fog formation by warm air advection over colder water and in areas of enhanced (shelf) turbulence need to be revisited. The study also elicited new phenomena, for example, the Fog Shadow (clearings of fog downstream of islands).

Significance Statement

Fog research has escalated recently per climate-change implications and directed-energy (electromagnetic systems) applications. Here we report selected findings of Fatima-GB, a comprehensive multidisciplinary field campaign conducted in Grand Banks, one of the world's foggiest areas, for improving the understanding and predictability of marine fog. Our findings indicate historical understanding of marine-fog lifecycle requires a fundamental rethink to incorporate complexities of scale interactions. Fog covers 15 decades of spatial scales, wherein megameter-scale synoptic systems sway millimeter-scale turbulent eddies, within which micron-scale fog droplets spawn on either tens (bioaerosols) or hundreds (sea salt) of nanometers sized marine aerosols. We demonstrate the collusion of meteorological, oceanographic, turbulence, thermodynamic and (bio)physicochemical processes during marine fog evolution, which should help develop future sub-grid parameterizations for numerical weather prediction models (NWP).

Introduction

Fog is a collection of small airborne water droplets (size $\sim 1\text{-}30\ \mu\text{m}$) that forms near the earth's surface when an air mass becomes cooled and saturated, causing the horizontal near-surface visibility to drop below 1km (Myers 1968, WMO 1992). Aerosols are essentials for fog genesis, since they form the substrate (or fog condensation nuclei FCN) on which water vapor condenses to form droplets (Pruppacher and Klett 2010). The droplet growth is dependent on the (bio)physiochemical properties of atmospheric aerosols, meteorology, radiative forcing and turbulence. Hygroscopic aerosols are considered 'activated' when droplets reach a size conducive for further growth (Gerber 1981; Poku et al. 2019), while un-activated aerosols take up water and may remain airborne or settle through deposition processes (Farmer et al. 2021).

While the physical appearance of fog and clouds is nominally the same, profound dynamical differences exist between the two, due mainly to the earth's surface influence on fog. Fog occupies the lower Atmospheric Boundary Layer (ABL), and processes therein undergird the *lifecycle* of fog, namely, the formation, evolution/maturation and dissipation (Nakanishi 2000). The vertical air velocities in the lower ABL are much smaller than the horizontal velocities, causing fog to be deprived of the main cooling mechanism that drives clouds: adiabatic expansion of ascending air (Rodhe 1962). Instead, fog relies on surface processes such as ground radiative cooling, moisture/heat fluxing, mixing of air masses, and surface turbulence (MacDonald et al. 2020). Additionally, such local mechanisms are synoptically regulated, making fog a veritable multiscale phenomenon across a wide spatial continuum of fifteen decades – from global ($10^7\ \text{m}$) to microphysical (aerosols, $10^{-8}\ \text{m}$) scales.

Fog is broadly [and probably subjectively] classified into three categories: radiation, advection and mixing fogs (Fernando et al. 2021). Nocturnal radiative cooling of a moist surface air layer leads to *radiative fog*. Advection of warmer air over colder water causes *advection fog*. Nonlinear mixing between nearly saturated warm and colder air masses produces *mixing fog* (Taylor 1917). Special categories are also common, for example, clouds of ice crystals near the surface (*ice fog*), fog droplets freezing on surfaces (*freezing fog*), steam streaks arising within colder fog (*steam fog*), rain evaporating into drier air (*precipitation fog*) as well as location-based fogs such as valley, upslope and land fogs (Gultepe et al. 2016; Pu et al. 2023). Location fogs also include fog in the Marine ABL (MABL), *Marine Fog* – a type of extreme complexity and amongst the least predictable in meteorology.

Contributing to intricacy of marine fog are a myriad of upper-ocean, air-sea interaction and MABL processes illustrated in Fig. 1. Additional phenomena may appear at the transition

between ocean and land (Coastal Zone). Koračin et al. (2014) and Koračin & Dorman (2017) provide extensive reviews of marine fog. Coastal fog has been studied extensively, e.g., along the US West (Leipper 1994) and East coasts (Fernando et al. 2021) and elsewhere (Spirig et al. 2019). Both the *Sea Fog*, marine fog in the shallower “green” water away from the coastal zone, and *Open-Ocean Fog* over the deeper “blue” water remain under-researched. The megaproject described in this article, dubbed Fog and turbulence interactions in the marine atmosphere (Fatima), shifts attention to these understudied deeper waters, and explores new frontiers of knowledge on Sea Fog; see Appendix A. For general acronyms, see Appendix L.

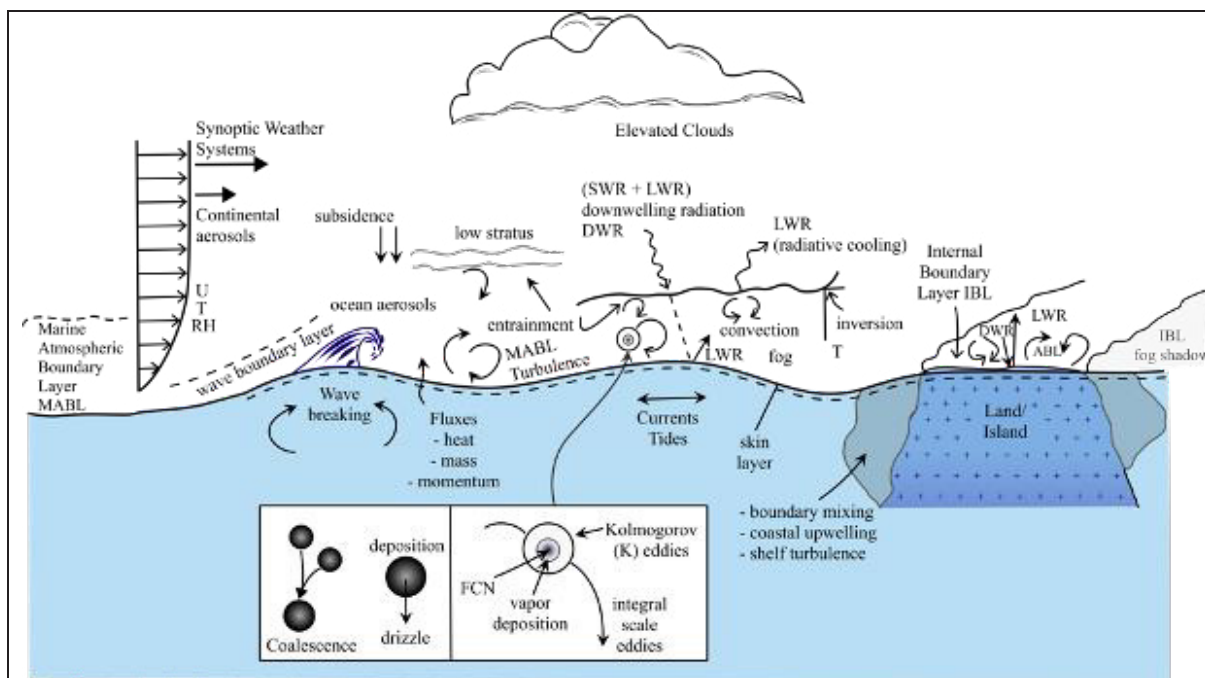


Figure 1: Marine Fog Processes - Advected continental or marine hygroscopic aerosols act as FCNs. Water droplets grow around FCNs by diffusional deposition of vapor (inset). Kohler (1936) argued that droplet growth requires exceeding of a critical radius determined by opposing effects of surface tension and solute concentration (whence droplet vapor pressure increase/decrease, respectively). The role of smallest turbulent (Kolmogorov or K) eddies in the ABL, within which FCNs are imbedded, however, is yet to be understood (inset). Note that, for the air, K scales and (Obukhov-Corrsin O-C) temperature dissipation scales are of the same order, and hence temperature within the K eddies or immediately surrounding FCNs is homogeneous. Spawning droplets undergo coalescence and settling (inset). Contributing upper-ocean processes/phenomena include waves and breaking, nocturnal convection, turbulence and mixing, tides, and currents. The corresponding lower-atmospheric phenomena include wave boundary layer and shear and convective turbulence. At the air-sea interface, turbulent heat, mass, momentum and aerosol exchanges occur by wave breaking and surface renewal via [molecular] skin layer, which fuel air-sea interactions. Short/Long Wave Radiative (SWR/LWR) and advective processes also affect Sea Surface Temperature (SST). Vital contributions of MABL come from synoptic and mesoscale [advective] systems including fronts, highs and lows, inversions, heating/cooling of the sea surface and fog top, diel cycle, clouds, turbulence and aerosols. If present, coastal contributions from boundary mixing, upwelling, escalated wave breaking, land/ocean [differential] heating, and internal boundary layers (IBL) have significant impacts on fog life cycle.

Low visibility in fog disrupts all modes of transportation, critical industrial operations such as oil platforms and free-space optical communications (Gultepe et al. 2009). The hazardous human health impacts of chemically active, pollutant-trapped, *smoky fog* (smog and thicker super fogs, visibility < 3.3 m) have been well documented (NWS 2024). Coastal fog has profound ecological consequences (Torregrosa et al. 2014). Marine fog is considered as an ‘unknown’ in asymmetric warfare, for example, when a swarm of small boats or UAVs are the blurred threat whence, for defense, directed energy systems such as High Energy Lasers (HEL) and optically-guided weapons are tools of choice (Pawlak 2012; Niece & Kaiser 2018). The shorter the wavelength, the higher the intensity of Lasers on the target (Jumper & Gordeyev 2017), and thus HELs applications prefer near-IR and visible wavelengths; such beams are stymied by the presence of fog (Perram et al. 2010). Fog is also evaluated as a potable water source amidst dwindling water supplies due to climate change (Bhushan 2020).

Understanding the nexus between fog, aerosols, radiation, flow and turbulence is critical for prediction of fog life cycle. Notwithstanding, owing to lack of high-resolution data and solid theoretical bases, NWP models employ parameterizations based on cloud-research for fog prediction, and unsurprisingly struggle for accuracy (Gultepe et al. 2006, Van der Velde et al. 2010; Boutle et al. 2018). Modeling studies typically invoke similarities between stratocumulus clouds and fog (Karimi 2020). Thus, melding of knowledge from multiple disciplines -- meteorology (ABL and free atmospheric flow), fluid mechanics (advection, turbulence and instabilities), thermodynamics (heat transfer), microphysics (aerosols and droplets) and (bio)geochemistry (gas-aerosol production, interactions and transformations) -- is imperative for improvements in fog prediction, which was the approach used in Fatima.

Fatima focused on two geographical areas of highest summer marine fog occurrences in the world. Based on climatology maps, Dorman et al. (2017) identified sixteen fog maxima over shallower water during the warm season. The two most prevalent (excluding anti-access/area-denial) sites were the southeast of the Grand Banks off Newfoundland (~ 50 - 200 m water depth) with a peak fog occurrence of 45% during June-July-August (JJA) and the Yellow Sea with 18% fog occurrence (~10 - 80 m depth, JJA); both belong to the Sea Fog category. Field campaigns at both sites have been completed, with the Grand Banks Campaign (Fatima-GB) during 01-31 July 2022 and Fatima-YS during 20 June – 08 July 2023. Given different basin, geographic and synoptic settings, stark disparities between fog-generation mechanisms (e.g., oceanic versus continental aerosols) were expected from the two sites.

Given the intrinsic merits of each campaign, this article exclusively concerns Fatima-GB. Dorman et al. (2017, 2020) hypothesized that southerly/southwesterly airflow over the negative SST gradients in Grand Banks, caused by mingling between Gulf Stream and Labrador waters, are important contributors to Sea Fog therein (Appendix A). Contrary to common belief that fog correlates with low ABL turbulence, the fog maximum in Grand Banks occurs at relatively higher median wind speeds (Isaac et al. 2020) and elevated turbulence levels associated with cyclonic systems passing over toward the North Atlantic. This article summarizes the execution and a few representative results of Fatima-GB, simultaneously covering synoptic to microscales – a pioneering study of its kind. Continuing challenges to Sea Fog research are also discussed.

Design and Execution of Fatima-GB

Capturing larger-scale weather systems down to K scales (Van der Hoven 1957) and investigating regions of enhanced oceanic turbulence apropos of Grand-Banks summer fog were the principal design considerations. The selected geographic area of the campaign and the Canadian Research Vessel, Atlantic Condor (R/V-Condor), that traversed the domain are discussed in Appendix B. The principal measurement locations were the (i) Grand Banks, a region with complex topography on the North American Continental Shelf, and (ii) Sable Island, an isolated, Canadian-owned, croissant shaped sand bar well exposed to the advection path of fog. Both R/V-Condor (Fig. 2) and Sable Island (Fig. 3; Appendix C) were densely instrumented for capturing synoptic to mesoscale weather and ABL parameters such as turbulence and fluxes, turbulent kinetic energy (TKE) and temperature-fluctuation dissipations at K and O-C scales (at Sable), radiation, water vapor and hydrometeors, visibility, electro-optic and electro-magnetic (at Sable) propagation, (bio)physicochemical properties of aerosols, SST, hydro-physical and turbulence properties of upper ocean, and surface waves. Continuous meteorological and visibility data from cooperating offshore installations (e.g., Hibernia oil platform) were also available. Instruments are listed below, and further elaborated in Appendix K with acronyms. For research group acronyms, see Appendix A.

Instrumentation on R/V-Condor (Fig. 2)

Instruments:

UND: Microwave Rain Radar (MRR-PRO), Microwave Radiometer (MWR), Uprising Vertical Microstructure Profiler (VMP-250), Optical Disdrometer, CTD, 300-kHz ADCP, Sea Snake, Visible and Cloud/IR cameras, Remote Ocean Sensing Radiometer (ROSR), FD70 Visibility Sensor, Ceilometer-CL61

NPS: Small Moored Wave Buoy, Rawinsondes, Surface and Scene Visualization Cameras

UU: Pyrgeometer and Optical Particle Counter (OPC-N3) for Tethered Lifting System (TLS)

DU: Fog Water Collector, Scanning Mobility Particle Sizer (SMPS), Aerodynamic Particle Sizer (APS), Fog Monitor FM120

YorkU: Micro Orifice Uniform Deposit Impactor (MOUDI), Nano-MOUDI-II, Ion Chromatograph, Gas Monitors

AFIT/NPS: Integrating Nephelometer, Black Carbon Aethalometer, Condensation Particle Counter (CPC)

Instrument Systems:

UND: Doppler Lidar and W-Band (cloud) Radar, both on motion stabilized platforms

PSL-NOAA/UND: Bowmast (3D-Sonic, LiCOR-7500, Weather Transmitter WXT520, GPS, Pressure (HMP), Pyrgeometer, Pyranometer)

UU/ARL/UND: TLS with Meteorological and Turbulence packages. Gimballed Pyrgeometer

NPS: C-CAMS [Crane-based Cloud and Aerosol Measurement System - an in-house developed fog/aerosol/turbulence sampling system measuring CO₂ and water vapor fluctuations (IRGASON), Platform Motion (VN-300), Pressure fluctuations (MET4A), Radiometric SST (CT-15), Relative humidity (RH) and Temperature (T) (HMP155), Visibility and meteorology (CS-125), Upwelling Radiation (Infrared Pyranometer), Net Radiation, Surface elevation (Radar Altimeter), Aerosol Absorption (Soot Photometer), Aerosol size spectra (Portable Optical Particle Spectrometer, POPS), Fog droplet parameters (FM120)], D-CAMS (same as C-CAMS but Deck-mounted)

OntTechU: Backscatter Cloud Probe (BCP) and Cloud Droplet Probe (CDP-2) on the Gondola Platform

Scripps/UCSD: Instrumented wave gliders [3D Sonic, WXT530, CTD, Profiling CTD, 300KHz ADCP, Current Profiler, Dual-GPS receiver, GPS-IMU]; and Uncrewed Surface Vessel [A/V Wallace, L3Harris C-Worker-5 with 2xSonics on a Flux Mast, FM120, Towed CTD, 500 Hz ADCP, Visible and IR 360 Cameras, X-band Radar]

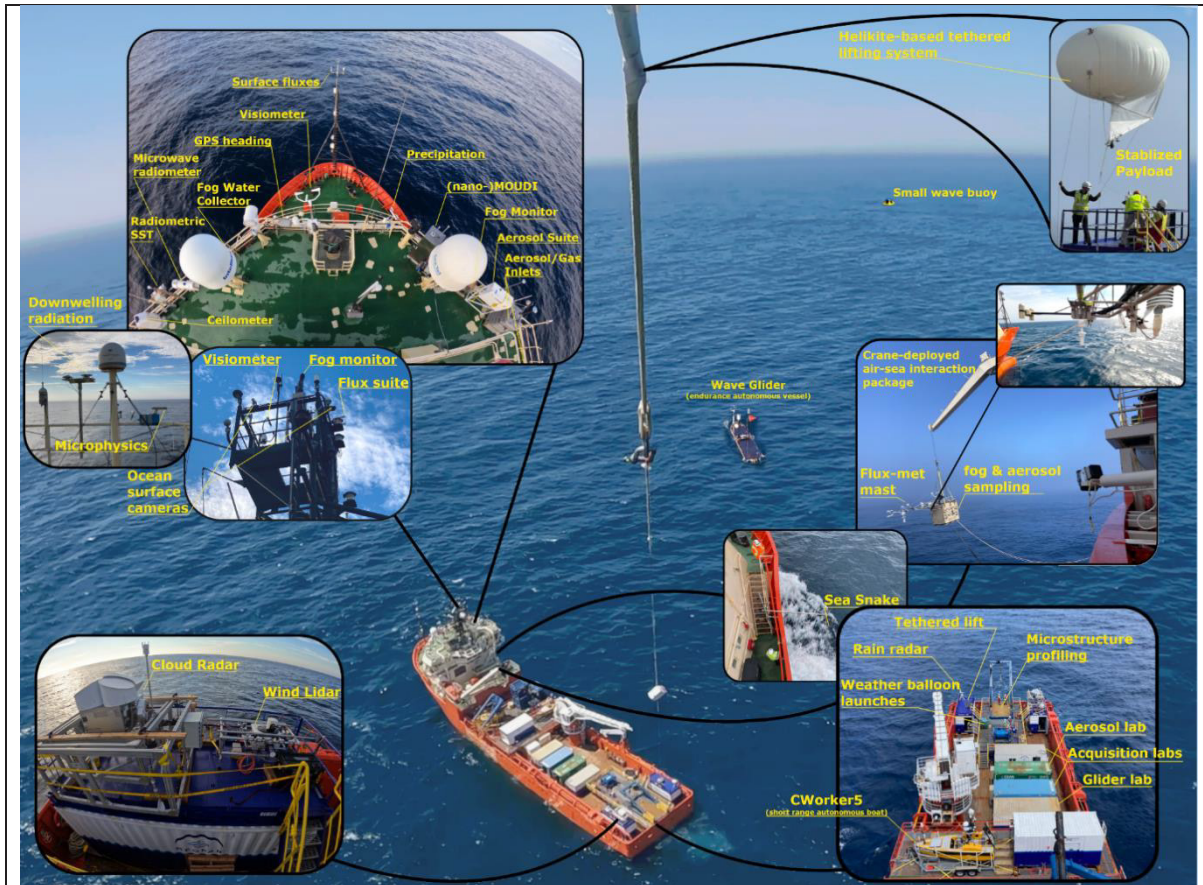


Figure 2: Instrumentation on R/V-Condor. This deep-sea supply vessel was converted to a research vessel by the Fatima group after extensive retrofitting. R/V-Condor was on lease from the Atlantic Towing Ltd. through the MEOPAR (Marine Environmental Observation, Prediction and Response), a Canadian National Network of Centers of Excellence on marine research. It was made available at a time when US vessels were unavailable due to Covid-related postponements/queuing.

Sable [Island] Campaign (Fig. 3)

Sable has an average width of ~ 700m (1.2 km at its widest point), length ~ 40 km, and is characterized by relatively simple topography with maximum elevation 30 m, minimal geographic changes from ocean to land, and low (~ 1 m height) grass coverage without vegetation. Being devoid of human footprint (i.e., anthropogenic heat and factitious elements that may alter fog thermodynamics), Sable is an ideal location to study marine fog and land interactions. Operated by the Parks Canada Agency as a strict Nature Reserve, it is a migratory bird sanctuary for over 2500 pairs each of terns and gulls nesting and breeding in the summer. During Fatima-GB, Sable was the homestead for 569 feral horses, with beaches roamed by a colony of harbor and grey seals.

Appendix C shows a plan view of Sable Island, along with two main deployment areas (Main Station and West Light), instruments and their owners. The Main Station was operated remotely, without disturbing tern nests that may eschew bird strikes. The backbone of West Light was an array of three (North, Center and South) towers along the climatologically streamwise

(southwest - northeast) transect, with instrument clusters surrounding them. Parks Canada required strict compliance with Canadian ecological conservation ordinances, accompanied by permits. Accordingly, instrument clusters were located in Parks-approved areas of little to no protected vegetation within electric-fenced enclosures to safeguard both the horses and equipment. Food and power are not available at Sable, and Parks-provided gas-powered generators were the electricity source. Routine charter aircraft services (and occasional helicopters in bad weather) were the reliable transportation link between mainland and Sable. An eight-member research team occupied an existing house in the West Light, with supplies flown in from Halifax. According to Parks Canada, Fatima-GB was the first large-scale meteorological field study ever conducted at Sable. The instrumentation listed below including acronyms are further detailed in Appendix K.

Instruments:

UND: FD70, PWD22 Visibility Sensors, Scanning Doppler Lidar, Net Radiometers, LiCOR, Sonics, Fine Wire T/RH sensors, Ceilometer-CL31.

NPS: MWR, Sodar, Scintillometer, Differential Image Motion Monitor, Wide Angle (Teleradiometric) Transmissometer, Non-coherent Extended Source Beacon, Rawinsondes, TLS, CS120 Visibility Sensor, CDP, transmissometer, differential temperature sensors, IRGASON, video cameras

UU: MRR-PRO, Ceilometer-CL31, Infrared Electromagnetic Propagation System (Scintillometer-BLS900), Microwave Scintillometer (RPG-MWSC-160), OPC-N3, visibility cameras, Liquid Water Content (LWC) probes, Soil Heat Flux Sensor, Soil moisture and temperature T Sensor (CS650), Soil T probe, CS125

AFIT: Cloud Ice Nucleation Characterization System (CINCS)

UMAN: Multi-parameter Bioaerosol Spectrometer (MBS)

Instrumented Systems:

UND: Super Combo Probe (In-house built) to capture T and scalar dissipation in turbulence

NPS/UU: TLS with temperature, RH, wind speed/direction, pressure, OPC-N3, pyrgeometer

UU/UND: Flux towers

UU: LEMS Automated Weather System; Precision Radiation Balance Sawhorse (4 components of SW, LW and net radiation)

OntTechU: Unmanned Aerial System UAV (with T, P, RH, OPC-N3 probes), Microphysics Supersite (Ceilometer-CL51, WXT520, PWD52, FM120, Ground Cloud Imaging Probe (GCIP), 3D Sonic, Sunshine Pyranometer, Digital Camera for local view)

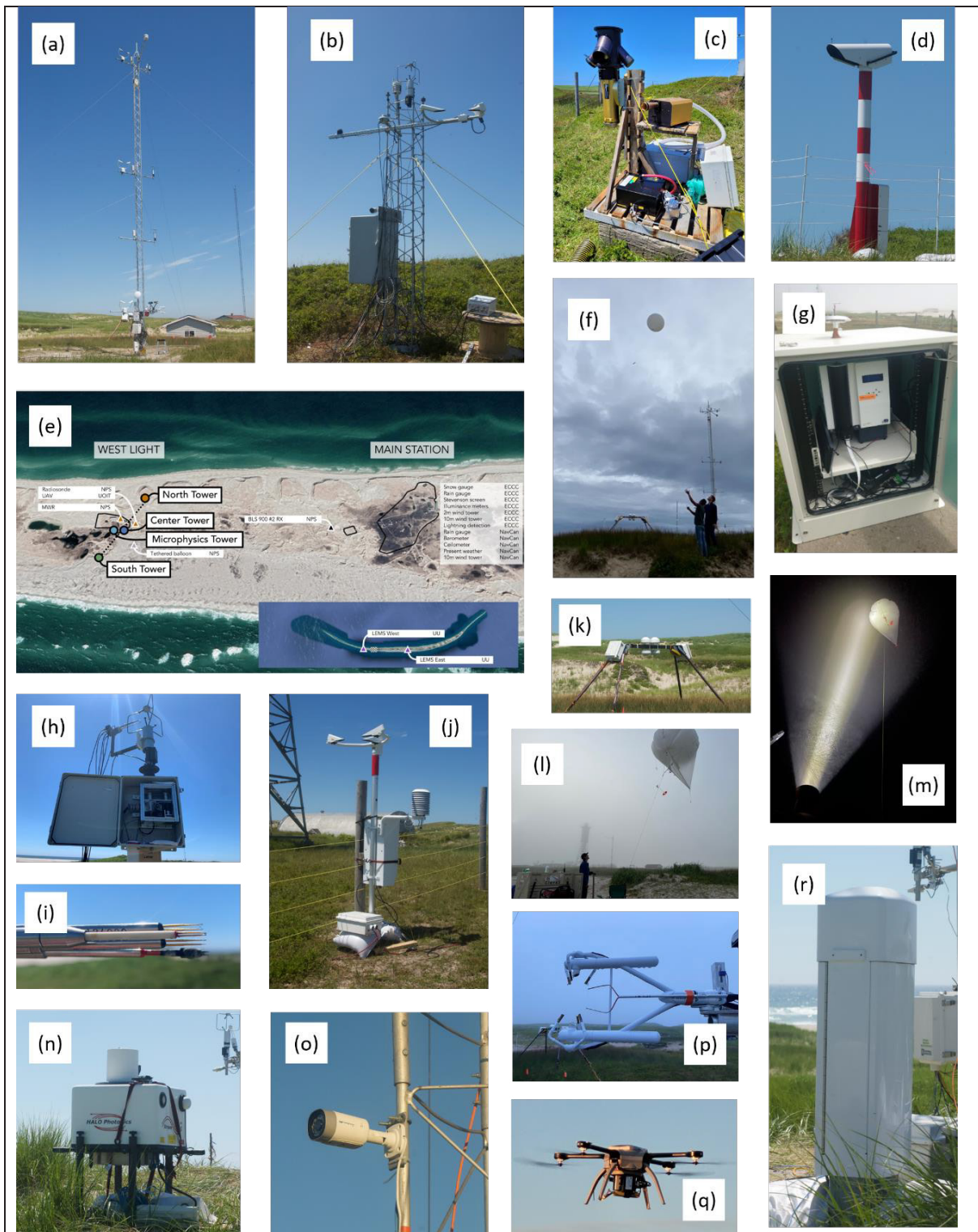


Figure 3: A sample of instruments at Sable. (a) The central flux tower; (b) the microphysics tower; (c) FM120 and GCIP; (d) Transmissiometer (LT31); (e) map showing the tower transect and two satellite sites; (f) rawinsonde releases; (g) CINCS; (h) Super combo system for TKE and T dissipation measurements; (i) Super combo probe ensemble; (j) FD70; (k) radiation balance measurements on saw-horse structure; (l) TLS profiling system; (m) TLS profiling with fog/mist visualization using a powerful flashlight; (n) Halo Photonics Doppler wind Lidar; (o) webcam; (p) LWC probe within an IRGASON probe volume; (q) UAV with meteorological instruments; (r) Vaisala CL31 ceilometer. Instruments on each tower are also in Appendix C.

Limited surface weather, visibility and microphysics data (from PWD50, FM120,

WXT520, CL31) at 1 minute, mixed with 15 minute and 1-hour data were provided by the Hibernia site during June-August 2022.

Intense Operational and Study Periods (IOPs and ISPs)

Although most instruments operated continuously, expensive, labor-intensive, and high-maintenance systems such as high-frequency rawinsonde launches (8-24/day instead of 4/day), VMP-250 and C-CAMS were operated only during IOPs. In general, IOPs were called during [virtual] weather briefings conducted daily at 1300 ADT by a group of ~ 13-20 participants. For guidance, NRL used COAMPS^{®1} operational mesoscale model at 1 km resolution with initializations at 48, 24 and 12 hrs ahead (Hodur 1997). YorkU used WRF model (Skamarock et al. 2008) with 10 km resolution, generating simulations from 1800 UTC to 1800 UTC next day after a spin-up time of 12 hrs. Both models used Global Forecast System (GFS) model for initial and boundary conditions, and generated hourly forecasts. Horizontal maps and vertical profiles at selected locations were examined. Also used were GFS (resolution 0.25°) output, GOES Satellite Imagery, Weather Radar, RAOB and NOAA HYSPLIT back-trajectories (UCSD and OntTechU). For Sable, an IOP was invoked by group consensus when conditions for capturing at least parts of the fog lifecycle appear favorable. IOPs typically lasted 24-36 hours, except for propitious 72-hour “Super-IOPs.” Table 1 lists the IOPs. Fog (Visibility < 1 km) appeared during 9 of the 14 IOPs.

Table 1: IOPs for Sable Island (in Atlantic Daylight time ADT = UTC - 3 hrs.)

IOP #	Start (ADT)	End (ADT)	Hydrometeor Type (PWD22/FD70)	UAV	TBS	Rawinsonde frequency	Observer notes	Synoptic Set up
1	J03 1800	J04 1800	FG/BR/DRZ/RN	√	x	√ (3 hr)	Mix hydrometeors	HP/MX
2	J06 1800	J07 1800	DRZ/RN	√	x	√ (3 hr)	Rain/mist	CG/MX
3	J09 2100	J11 0130	BR/patchy fog	√	√	√ (3 hr)	IOP-wavy structures	LP/ST
4	J12_1800	J13_1500	CLR	x	√	√ (3 hr)	Failed fog/reference case/visibility fluctuations	LP/ST
5	J13_1800	J15_1500	BR/CLR	x	√	√ (3 hr)	Super-IOP, excellent FG event	HP/MX
6	J15 1500	J16 0900	FG/BR/DRZ/RN	x	x	√ (3 hr)	FG but windy	HP/ST
7	J17 1800	J18 1800	FG/BR/DRZ/RN	x	√	√ (3 hr)	FG front, Ext IOP	HP/ST
8	J18 1800	J20 0900	FG/BR/DRZ/RN	x	x	√ (3 hr)	FG and high wind	HP/ST
9	J21_1500	J22_1500	FG/BR	x	√	√ (3 hr)	Excellent FG formation/persistent	HP/ST
10	J23_1200	J25_1800	FG/BR/DRZ/RN	x	√	√ (3 hr)	Super IOP, Advection FG; strong winds; FG shadow predicted	HP/ST

¹COAMPS is a registered trademark of the U.S. Naval Research Laboratory

11	J26_0600	J27_0600	BR	x	x	√ (1 hr)	Late FG shadow possible, dissipates early morning	CG/MX
12	J28_2100	J28_2330	FG/BR/DRZ/RN	x	√	√ (12 hr)	Thin barely visible FG layer/BR, Radiation impact, light drizzle	CG/ST
13	J29_1600	J30_1800	BR/RN	x	√	√ (3 hr)	Post frontal FG/Stratus lowering/light rain after fog	LP/MX
14	J30_1800	J31_0900	FG/BR/RN	x	x	√ (3 hr)	Rain and 1.5 hr FG on next morning	LP/MX

J = July. BR, FG, DRZ, and RN signify mist, fog, drizzle, and rain conditions, respectively. HP, LP, CG, MX, and ST refer to the high pressure, low pressure, convergence zone, mixing, and stable synoptic conditions, respectively. Local conditions may change over the course of IOPs. Note that FG, BR, and DRZ transitions (identified by FD70) are not very smooth and may be lumped all together.

Naturally, IOPs for Sable Island were not optimal for R/V-Condor, which trekked in and out of fog (Figs. 4a-c). As such, suitable study periods, dubbed Intense Study Periods (ISPs), were identified *posteriori* using the following criteria beneficial for later analysis: (i) visibility < 1 km, (ii) relative wind direction within $\pm 60^\circ$ of the bow course, and (iii) ship speed < 3 m s⁻¹ (and winds generally > 5 m s⁻¹). Fig. 4 shows the visibility, rawinsonde, meteorological, and microphysical information for six ISP periods identified using above criteria. A list of ISPs is in Table 2.

Table 2: ISPs at R/V Atlantic Condor

ISP	# of Rawinsondes	Start Time (UTC)	End Time	Comments
1	32	July 8, 06:10 am	July 14, 2:50 pm	Significant synoptic systems passing through (at the shelf break; Near Hibernia)
2	13	July 13, 03:10 pm	July 16, 07:00 pm	Approximately constant wind direction (at the shelf break; Near Hibernia)
3	15	July 21, 12:40 pm	July 23, 1:00 pm	Near Sable Island on the shelf
4	13	July 23, 09:00 pm	July 25, 08:30 pm	-ditto-
5	19	July 25, 09:30 pm	July 27, 01:30 pm	Sable Lee Observing Period (SLOP)

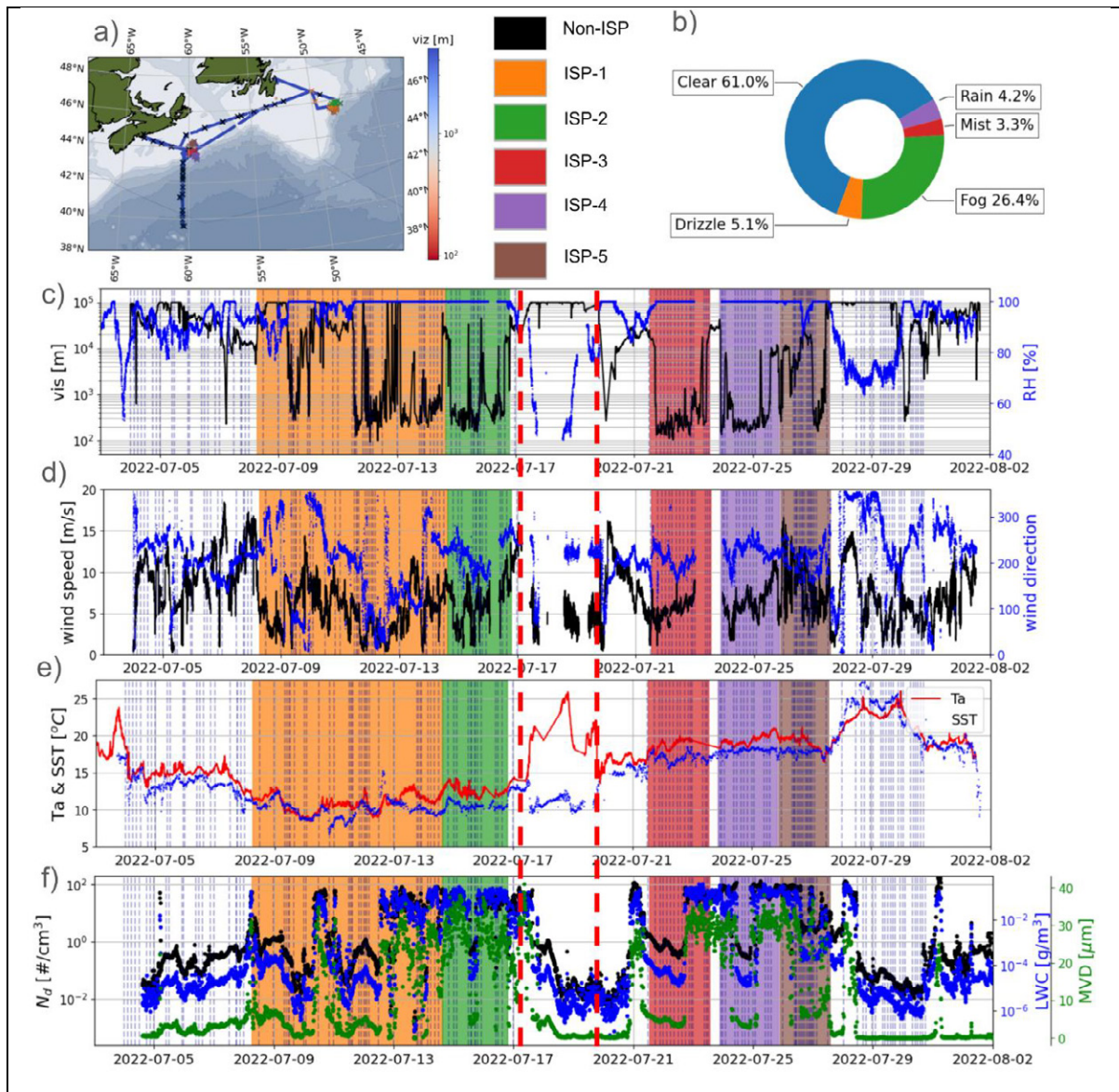


Figure 4: (a) Condor track with rawinsonde release locations (x), color at each location indicating visibility (from FD70); (b) Pie chart of hydrometeor status (FD70) during the campaign; (c) visibility (FD70) and ISP durations identified in color shading based on the criteria in the text (also see Table 2); (d) Ambient wind speed WS and direction WD (bow mast) (e) Air T and SST (bow mast and ROSR) (f) Aerosol number concentration (N_d), LWC (FM120) and Mean Volume Diameter (MVD). Red vertical broken lines demarcate the port call of R/V-Condor at St. Johns, Newfoundland. The vertical dashed lines indicate the times of radiosonde launches, corresponding to (a).

Data Repository

The primary means of data storage is a google drive, allowing quick and convenient access and secure cloud storage. At present, data from individual groups have been saved into a shared google drive. A mirrored hard drive is also maintained. Types of data being uploaded include raw data, processed intermediate data and quality-controlled data for improved accountability in data analysis. Supporting datasets such as satellite imagery and model

forecast/reanalysis used by the forecasting group are also catalogued and saved. All datasets will be available for the science community after 01 August, 2025.

General Observations

In addition to those of R/V-Condor shown in Fig. 4, representative observations at or near the Sable Island are shown in Fig. 5 as time series of meteorological, thermodynamic, turbulence, microphysical, and surface variables from the central tower, a total of 182 soundings, and by the wave glider “Carson” operating in the shallow waters southwest of Sable that provided nominal upwind upper-ocean and lower-atmospheric conditions. Shaded periods in Fig. 5 (a-o) are IOPs. Note the (i) predominant southerly/southwesterly wind direction (a), (ii) wind perturbations in response to diurnal temperature cycle at low wind speeds (a), (iii) weak diurnal variability of SST and marine T_{air} (l); (iv) elevated LWC, MVD and N_d during IOPs with fog, consistent with previous measurements (Gultepe et al. 2021) in marine fog in North Atlantic (g-i); (v) [predominant southwesterly/westerly] winds punctuated by occasional periods of heightened wind speeds aloft up to 20 m s^{-1} (p); and (v) persistently moist air ($\text{RH} > 80\%$) with propensity for saturation that frequently extends beyond 1.5 km (r). Extensive campaign-wide data of the ilk illustrated in Figs. 4 and 5 have motivated a variety of ongoing process- and numerical studies.

The daily averaged aerosol number concentration on the R/V-Condor is shown in Fig. 6a for both fog and no fog conditions. During 04-17 July, the R/V-Condor was in Grand Banks away from Sable Island (dubbed Grand-Banks Period) whereas it was in the vicinity of Sable Island during 19 July – 01 August (Sable Period). A larger aerosol concentration occurred in coastal areas close to Nova Scotia during 03-04 and 30-31 July, around Sable (21-25 July), and towards the Gulf Stream (27-29 July). Lower aerosol concentrations were observed in Grand-Banks (10-13 July), suggesting less continentally-influenced air, consistent with the CO measurements shown in Fig. 6b. In contrast, a higher aerosol concentration occurred in coastal areas close to Nova Scotia during 03-04 and 30-31 July, around Sable (21-25 July), and towards the Gulf Stream (27-29 July), suggesting more pollution influence, also consistent with the CO measurements (Fig. 6b).

Overall, $< 100 \text{ nm}$ aerosols accounted for $\sim 60\%$ and $100\text{-}200 \text{ nm}$ for $\sim 30\%$ of the total number concentration (Appendix D), demonstrating the controlling influence of smaller particles. During fog, the median particle number concentration decreased by 40% and 30% for particles in the ranges of $10\text{-}100 \text{ nm}$ and $100\text{-}200 \text{ nm}$, respectively, but did not show significant change for the larger particles. It appears that smaller particles were more

susceptible to losses due to Brownian diffusion leading to wet scavenging, as observed in clouds (Greenfield 1957). Conversely, particles > 200 nm were unaffected by fog, causing an increase of their relative contribution (Wu et al. 2022).

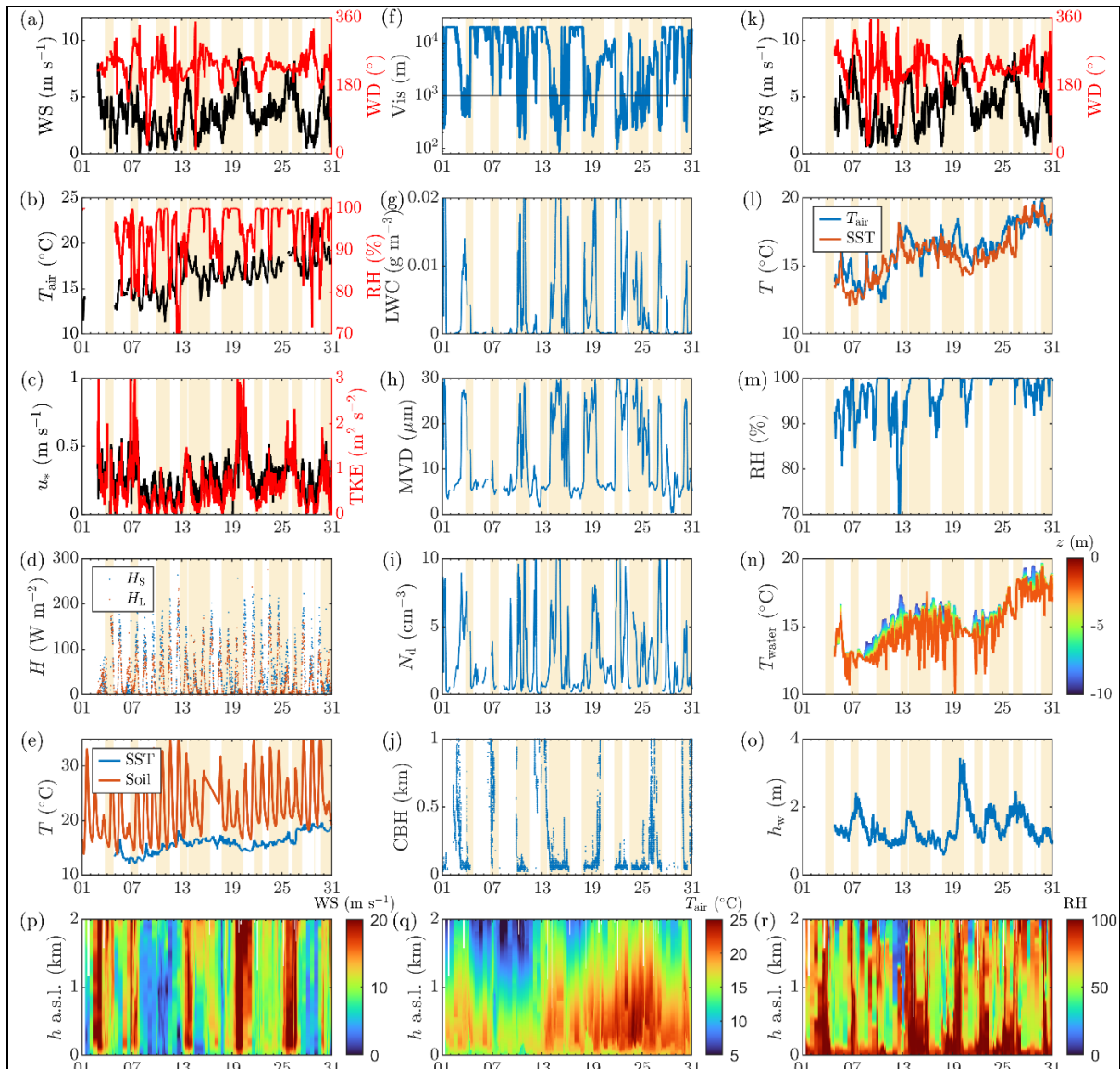


Figure 5: Data from the (a-e) center tower (15 m), (f-j) microphysics station, (k-o) wave glider Carson operating 30-60 km southwest of Sable (Grare et al. 2021), and (p-r) radiosondes (3-4/hour). (a) 2 m wind speed WS and wind direction WD; (b) 2 m air temperature T_{air} and relative humidity RH; (c) 2 m friction velocity u_* and turbulent kinetic energy TKE; (d) 2 m sensible and latent heat fluxes (H_s , H_L); (e) soil temperature T_s and SST; (f) visibility Vis (1 km threshold or fog is identified by a horizontal line); (g) liquid water content LWC; (h) MVD; (i) droplet number density N_d ; (j) cloud base height CBH; (k) WS and WD (k-o, from wave glider Carson); (l) T_{air} and SST; (m) RH; (n) water temperature T_{water} ; (o) significant wave height h_w ; (p) WS (p-r, from rawinsondes); (q) T_{air} ; and (r) RH. a.s.l – above sea level. For instrument details, see Appendix K.

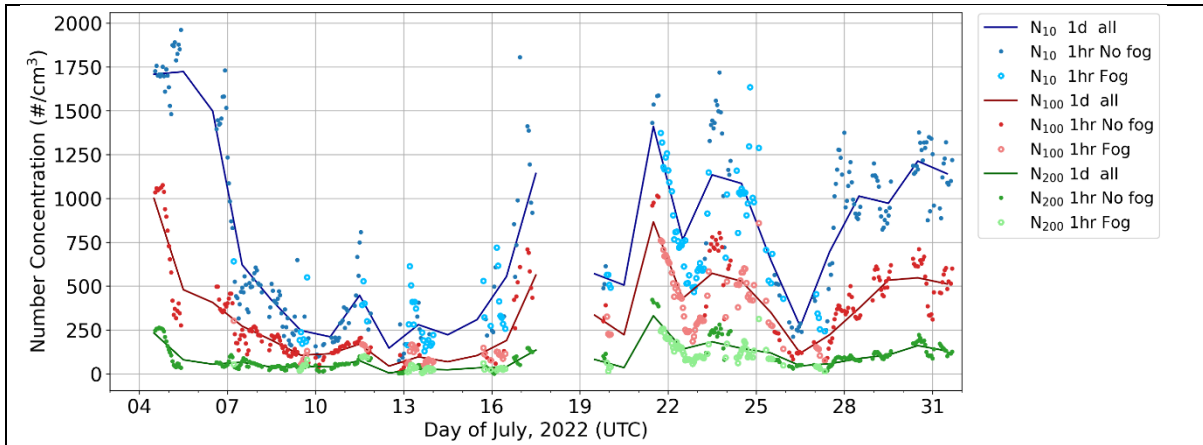


Figure 6(a): Aerosol number concentration from 10.6 to 496 nm measured with the SMPS on the ship bridge (Appendix K). N10 (blue), N100 (red) and N200 (green) indicate the number concentrations of all aerosols with diameter > 10 nm, 100 nm, and 200 nm, respectively. The solid lines represent daily (1d) averages, small dark solid circles are hourly (hr) averages during no fog, and large bright circles are hourly averages during fog. The aerosol inlet sampled dry aerosols at 19 m a.s.l. and travelled through 11.35 m of stainless-steel tubing before being measured by the SMPS. The gap of observations during July 17-19 was due to the port call.

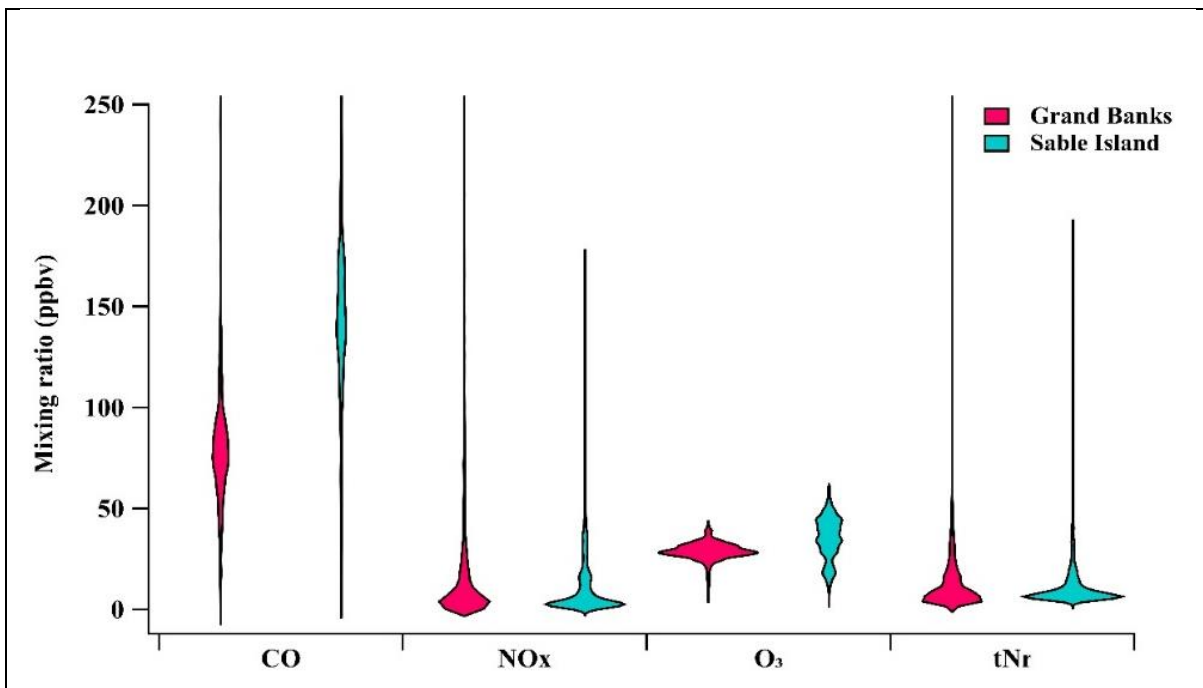


Figure 6(b): A Violin plot of atmospheric pollutant distributions of combustion product mixing ratios that are long-lived like carbon monoxide (CO) or moderately-lived like nitrogen oxides ($\text{NO} + \text{NO}_2 = \text{NO}_x$). NO_x was analyzed via chemiluminescence (Ecotech EC9841), ozone via nondispersive ultraviolet absorption (Ecotech S10) and carbon monoxide CO via infrared absorption spectroscopy (Ecotech EC9830). The instruments were on the ship bridge, and sampled outdoor air from a common sampling manifold passing through the ceiling to the deck above the pilothouse and positioned bow-side (upwind) of the ship exhaust. A custom-built instrument for measuring total gaseous reactive nitrogen (tNr) and its basic fraction (e.g., species like ammonia and amines; NH_3/NR_3) were also sampled from the manifold (Crilly et al. 2023).

In matters of gridded gas mixing-ratio observations (Fig. 6b), being further from major anthropogenic emissions regions, the Grand-Banks period is less burdened with the combustion tracer CO compared to the heavily trafficked Sable period (75 ppbv vs 140 ppbv), the latter being closer to the dominant continental outflow of the North American seaboard. Similarly, enhanced O₃ were present in the Sable region (40 ppbv vs 30 ppbv for Grand-Banks). Observations of NO_x and total reactive Nitrogen tN_r were similar in both locations, indicative of NO_x being the primary component of tN_r. Secondary photochemical species (e.g., O₃) are indicative of the pollution regime (Lakra and Avishek 2022), and novel chemical measurements such as tN_r accomplished in Fatima-GB enable the study of particle and droplet composition thermodynamics of fog.

Archetypal Process and Case Studies

Synoptic Weather Systems – A Trigger for Fog

Synoptic analyses during Fatima-GB suggest that the [longstanding] hypothesis – northward advection of air masses over Gulf Stream causes them to be warm and humid, which, when passing aloft colder Labrador water creates conditions for escalated summer fog in Atlantic Canada (Appendix A) -- is untenable. The bulk of the July 2022 surface winds at Sable were southwesterly, following the northward advection path, but fog occurred at Sable only 30% of the time. Fog genesis mostly required a synoptic trigger, a prospect being eastward propagating deep lows across Eastern Canada. Such systems have broad southward oriented trough that extend across the Atlantic coast and beyond Sable, almost-always accompanied by a broad cloud band with low overcast ceilings (~60 m) and lowered visibility (~1-3 km). After the leading edge passes over Sable, there are occasional fog periods, and a trailing ridge encroaching into the middle and lower layers lowers the cloud top and ultimately terminates fog and clouds.

An example is the IOPI, with a cloud band lowering over Sable at 0200 UTC 03 July, and dropping visibility below 4.8 km and ceiling below 915 m. There were two fog periods within this event, one long (1100 UTC 03 July to 0120 UTC 04 July) and the other short (0900 to 1145 UTC 04 July). At 1200 UTC 03 July, the driving Low was centered in northeastern Quebec with a deep trough (low) extending along the eastern coast of Quebec, off the Newfoundland eastern coast and southward in the Atlantic to 42°N (Fig. 7a), generating strong southwesterly surface winds over most of Atlantic Canada and a concomitant cyclonic cloud band along the Quebec coast and then extending to the southwest over water (Fig. 7b). This

was the first fog period, under a mid-level cloud band. Rawinsondes show that the saturated fog layer included a surface-based air temperature inversion, in the height range of 187-730 m.

With time, MSLP trough and cloud band moved eastward. A ridge on the westside of the cloud band began to encroach on the band, lowering the cloud top. A low cloud, fog bank appendage began to extend out from the cloud band, with the second fog forming at 0900 UTC 04 July. This is evident in 1200 UTC visual satellite image, extending well out from the sharp, western wall of the band (Fig. 7c). The second fog period had ended 16 minutes before this image. Sable was on the edge of the cloud bank in this image 5 minutes before. Rawinsondes show that the fog layer during this second period was a single isothermal layer 170 m deep capped by a dry air inversion. Thus, the two events differed in structure. While details vary, the broad features of the two events were captured by the WRF-ARW simulations (Appendix E) such as patchiness of fog and dry inversions aloft the potential fog layer. The visibility during 0000 UTC 2 July-0000 UTC 05 July was directly related to the divergence (Fig. 7d). The lowest visibility and fog occurred with the most negative divergence (i.e., convergence). The maximum visibility occurred with the greatest convergence that triggered surface layer lifting.

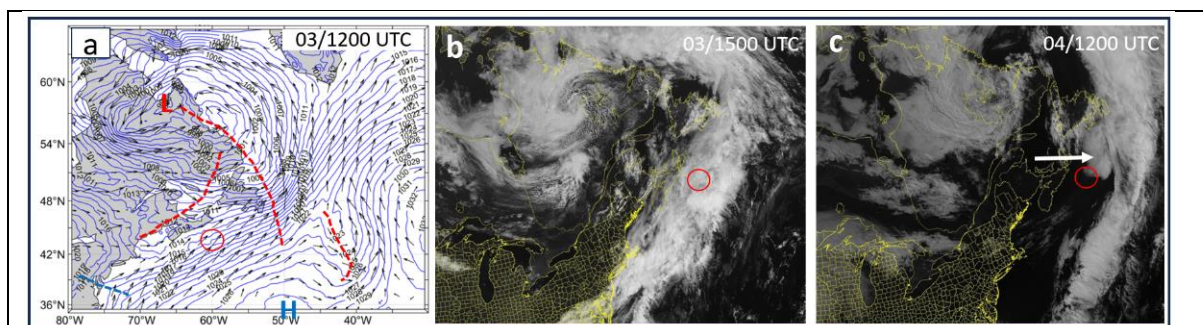


Figure 7: (a) A plot of the GFS Mean Sea Level Pressure (MSLP) at 1200 UTC 03 July 2022. L is a deep low pressure on northeastern Canada which dominates Atlantic Canada with a trough (dashed red line) extending to the south along the coastline past Newfoundland. A second trough (dashed red line) extends to the southwest toward New England coast. The H is the center of a high pressure to the South that dominates the surface layer over water. These features cause strong southwesterly surface winds off Atlantic Canada and over Sable (the center of the red circle). (b) GOES East satellite visual image at 1500 UTC 03 July. A high-topped cloud band extending from the US southwest follows the coastline over water, with Sable in fog, through the Labrador Sea, and cyclonically curls around to the center of the Low in a). (c) Same as (b) but at 1200 UTC 04 July when the cloud band shifted farther east offshore while anticyclonic conditions cleared the sky over Nova Scotia, the surrounding water and over a low cloud/fog bank extending from the main cloud band (white arrow) that contained a second fog period at Sable Island that ended soon afterward with clear sky. Almost all July fog at Sable occurred in the presence of a synoptic scale cloud.

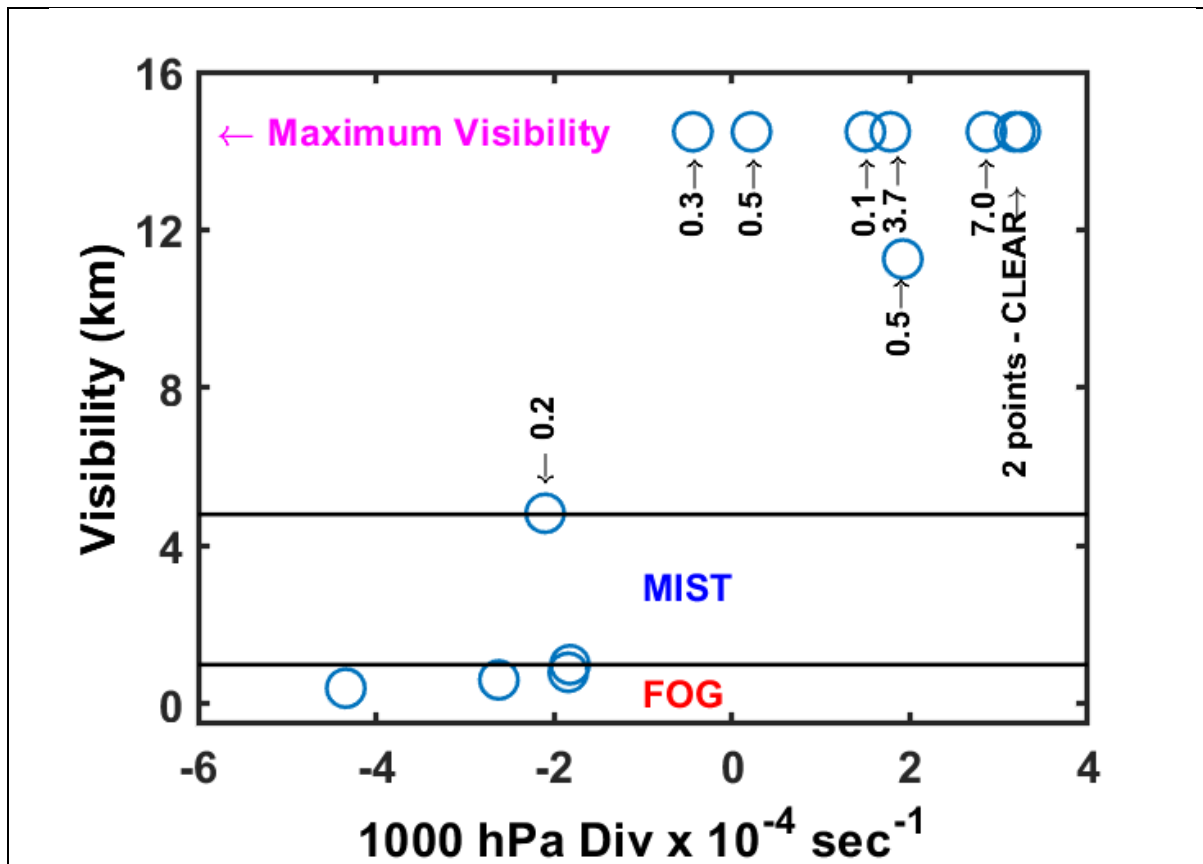


Figure 7(d): Visibility in Sable plotted against divergence based on the GFS 6-hourly 1000-hPa data for 0000 UTC 2 July - 0000 UTC 05 July. Fog visibility < 1 km and ‘mist’ visibility < 4.8 km are noted. Posted numbers are the cloud base ceiling heights in km. Not shown are the ceiling heights 0.06–0.09 km during fog. CLEAR denotes a cloudless sky. The maximum measured visibility is 14.5 km. The visibility was related to 1000 hPa divergence which was lowest with the most negative divergence (convergence) and fog and was greatest with the most positive divergence and a clear sky. Greater visibility also increased with cloud base ceiling heights.

Aerosols and their Evolution -- Seeds of Fog

A case study representative of size-resolved aerosol processing during IOP9 is shown in Fig. 8. Both MOUDI and nanoMOUDI that capture, respectively, particle sizes ranging from 0.1 to 100 μm (including fog) and 0.01 to 0.1 μm (ambient aerosols) were used. The samples were chemically characterized using ion chromatography applied to aqueous extracts to yield size-distributed mass loadings of major cations (Na^+ , NH_4^+ , K^+ , Mg^{2+} , and Ca^{2+}) as well as alkylamines such as dimethylamine DMAH^+ and diethylamine DEAH^+ (Salehpoor & VandenBoer 2023) and anions ($\text{CH}_3\text{SO}_3^- = \text{MSA}^-$, Cl^- , NO_2^- , Br^- , NO_3^- , SO_4^{2-} (Place et al. 2018)). Fig. 8 covers the ambient conditions, followed by onset, persistence and dissipative conditions of fog.

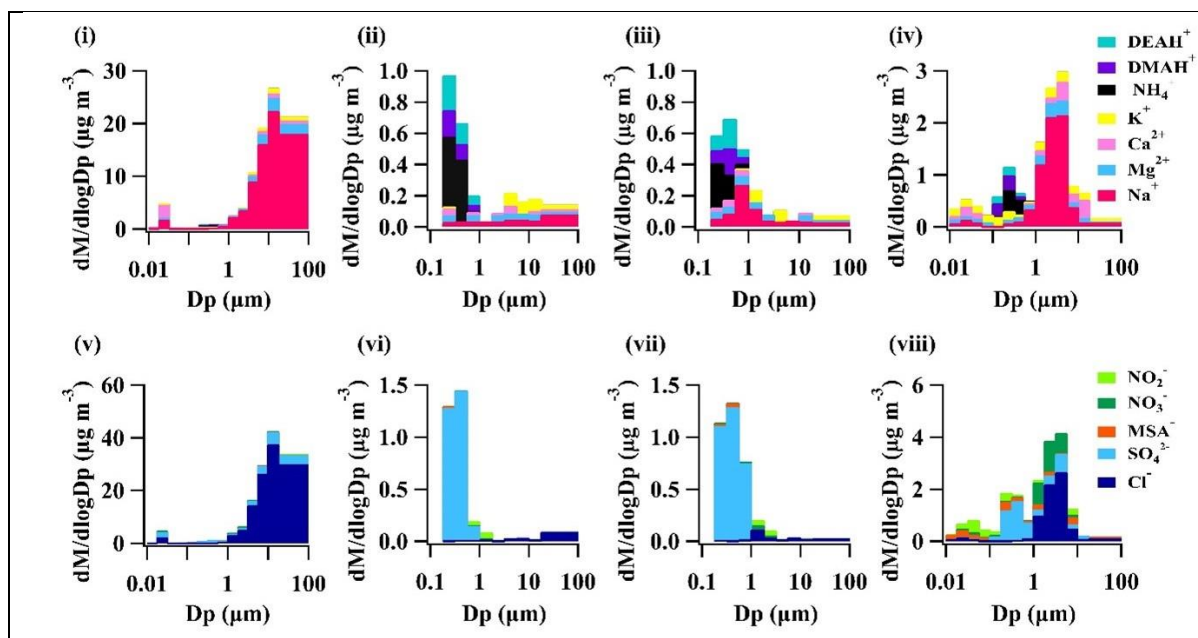


Figure 8: Ion mass loading ($\mu\text{g m}^{-3}$) data samples taken near the Sable Island during IOP9 (19-23 July) by R/V Condor: Ion mass loading of major cations (top row) and anions (bottom row) taken under ambient conditions (pre-fog; i and v, covering 19-21 July), during the fog persistence period sampled during two consecutive intervals (ii and vi during 21-22 July, and iii and vii during 22-23 July), and after the dissipation of fog (iv and viii, 23-24 July) are shown.

A MOUDI and nanoMOUDI II was positioned within a weatherproof enclosure mounted to the railing on the deck above pilothouse (~ 10 m asl) were used. Samples were collected using MOUDI during fog events while nanoMOUDI sampled ambient aerosols, both instruments sampling with a flow rate of 30 L min^{-1} . The MOUDI uses 9 impaction stages to capture particles of aerodynamic diameters from 0.1 to $100 \mu\text{m}$ (Chisholm et al. 2021) whereas nanoMOUDI uses additional 5 impaction stages to collect $0.01 - 0.1 \mu\text{m}$ particles. Fifteen samples during fog events and fourteen ambient samples were collected with durations spanning 197 to 2490 min.

During the fog event, the mass loading of sea-salt ions like Na^+ , Mg^{2+} , Cl^- , and sea salt sulfate (ss-SO_4^{2-}) in the coarse mode ($1-100 \mu\text{m}$) decreased by two orders of magnitude compared to pre-fog conditions due to scavenging and deposition. Following fog dissipation, sea salt aerosols returned, but their mass loadings were lower by a factor of ten compared to the pre-fog period. These findings are consistent with the expected role of sea salt aerosols acting as effective FCN, given their high hygroscopicity (Zhao et al. 2022; Sasakawa et al. 2003; Jung et al. 2013). In the fine mode ($0.1-1 \mu\text{m}$), the mass loadings of reduced nitrogen (NH_4^+ , DMAH^+ , and DEAH^+) and processed sulfur (MSA^- and non-sea salt sulfate) increased during the fog event compared to the boundary periods, suggesting that droplets and meteorological conditions supporting fog formation potentially facilitate gases and interstitial aerosol to participate in chemical reactions and gas-to-aqueous partitioning (Ge et al. 2012; Meng & Seinfeld 1994). The mass loading of interstitial aerosol, therefore, increased during fog events and persisted afterwards. This confirms the well-known fog scavenging mechanisms of supermicron sea salt aerosols into droplets beyond $20 \mu\text{m}$ in diameter (Richter et al. 2021;

Wagh et al. 2021). The findings are also consistent with marine fog-facilitated gas-particle partitioning recently reported in the Arctic (Kecorius et al. 2023). Upon fog dissipation, supermicron sea-salt aerosols were generated faster than their losses and returned to observable levels.

In addition to aerosols $> 0.1 \mu\text{m}$ discussed above, attempts were made to characterize bioaerosols using novel, high-resolution detection technologies. Biological species and organic compounds with sizes from tens of nanometers to $100 \mu\text{m}$ are prevalent in sea spray aerosols (SSA), thus making nascent growth factors (e.g., hygroscopicity and nucleation) for SSA deviate from pure salt particles (Bertram et al. 2018). The roles of bioaerosols as CCN or FCN are poorly characterized at present (Schiffer et al. 2018), but bioaerosols containing ice nucleating proteins are known to act as ice nuclei and possibly FCNs for rapid mixed-phase cloud/ice-fog formation via heterogeneous processes (Knopf et al. 2018; Huang et al. 2021; Crawford et al. 2020, 2023). Two bioaerosol instruments were deployed: CINCS, a novel instrument designed for sizing, and MBS designed for concentration. Imitating the human lung, CINCS ingests biological cells with minimal stress to the organism, thus maintaining their viability and facilitating post-collection analysis using standard techniques. *Pseudomonas syringae* (PS), known to be conducive for ice-nucleation, was selected as the target bioaerosol (Soveizi et al. 2023). The second, MBS is a biofluorescence spectrometer that detects and classifies bioaerosols in real-time time via the collection of autofluorescence spectra, size, and morphological parameters on a single particle basis. Following Freitas et al. (2022), MBS data were classified into following representative groups: weakly fluorescent populations (e.g., SSA with organic content), fluorescent sea spray aerosols (FSSA), highly fluorescent sea spray aerosols (HFSSA), primary biological aerosol particles (PBAP) and non-fluorescent aerosols.

Initial analysis of CINCS data from 25-30 July suggested an increased presence of PS on 29 and 30 July (IOPs 13/14) as compared to the other days, suggesting microphysical enhancing capability may have had more of a hand in Fatima-GB rain events as much or more so than the onset/presence of fog (Appendix F(i)). The processed MBS data indicate notable PBAP events during 07-08, 28-29 and 30-31 July, and 31 July – 01 Aug, which are consistent with CINCS PS observations (Appendix F(ii)). There are more frequent, and extended HFSSA events throughout the deployment. Interestingly, while HFSSA concentrations are generally greater than PBAP, during the PBAP emission events the PBAP concentration significantly exceeds that of HFSSA. Increase of PBAP during drizzle or rain events is generally evident, while both HFSSA and PBAP are suppressed by fog via nucleation or scavenging/deposition.

These observations provide pointers for future multi-instrument interrogations on fog-bioaerosol nexus.

Lifecycle of Fog – Pursuing a Stratus-Cloud-Lowering Event

IOP13 encompassed a stratus-cloud lowering event, a common mechanism of fog formation (Koračin et al. 2001; Fathalli et al. 2022; Singh et al. 2024), as evidenced by synoptic analysis (not shown). Ceilometer backscatter, Doppler Lidar velocity vectors and contours of vertical velocity variance s_w show that preceding the event (2100 UTC, 29 July), the surface winds were southerly with RH \sim 85% while winds aloft were southwesterly/southerly (Fig. 9a). Rawinsondes indicate an unstable surface layer up to \sim 50 m with an overlying inversion up to \sim 200 m, topped by a relatively mixed layer up to \sim 300 m (Fig. 9b). Around 2230 UTC, winds aloft shifted more westerly and a stratus cloud appeared at 600-800 m (Fig. 9a), accompanied by stratus top cooling and temperature inversions beneath (see Singh et al. 2024), as evident from the 2058 UTC sounding (Fig 9b). Ensuing top-down convection (note the s_w contours) concomitant with light precipitation moistened the lowest 600 m (Figs. 9b, Appendix G). Convective turbulent mixing was observed both aloft by the Doppler Lidar (Fig. 9a) and at the surface by sonic anemometers (TKE, Appendix G). The stratus cloud descended approximately 600 m in 3.5 hours (starting 0030 UTC), leading to a dense, persistent, \sim 125 m thick fog layer. With the appearance of stratus, turbulence levels decreased and the winds throughout the lowest km shifted westerly.

The fog event was rather homogenous across Sable, based on visibility from the FD70 and BLS900 (Appendix G). The significant deviation between the BLS900 and FD70 at 1000 UTC was due to the full attenuation of BLS900 signal where lower visibility could not be resolved. The LWC at lower heights during most of the fog event was dominated by larger droplets (10-20 μ m) captured by FD70. In combination, FM120 and FD70 data painted a clearer picture of what was occurring, especially near the dissipation of fog just after sunrise (1030 UTC) when the fog layer began to lift (Fig. 9a).

During fog dissipation, TLS captured the profiles of T, RH, WS, LWC, and the net longwave radiation LWnet (Fig. 9c). Between 1130 and 1200 UTC, when the fog was still relatively dense, the LWnet profiles showed relatively strong radiative cooling. As the fog dissipation began, the larger droplets evaporated to augment the smaller-particle population and hence an increased LWC (by FM120) and an abrupt drop of visibility (Appendix G).

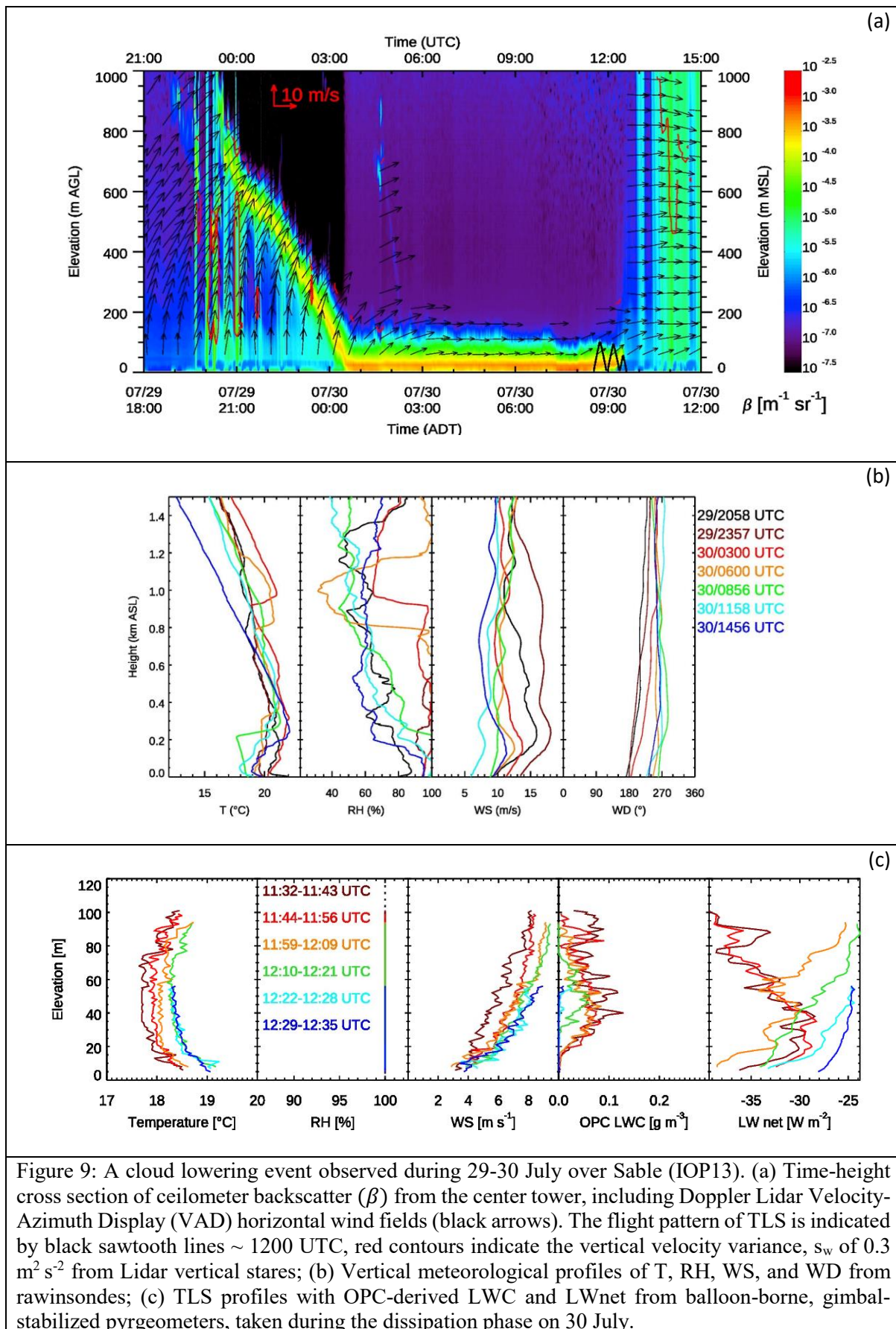


Figure 9: A cloud lowering event observed during 29-30 July over Sable (IOP13). (a) Time-height cross section of ceilometer backscatter (β) from the center tower, including Doppler Lidar Velocity-Azimuth Display (VAD) horizontal wind fields (black arrows). The flight pattern of TLS is indicated by black sawtooth lines ~ 1200 UTC, red contours indicate the vertical velocity variance, s_w of $0.3 \text{ m}^2 \text{ s}^{-2}$ from Lidar vertical stares; (b) Vertical meteorological profiles of T , RH, WS, and WD from rawinsondes; (c) TLS profiles with OPC-derived LWC and LWnet from balloon-borne, gimbal-stabilized pyrgeometers, taken during the dissipation phase on 30 July.

Concomitant were a LWnet profiles shift (Fig 9c) and tendency toward radiative heating. By 1200-1300 UTC, incoming SWR further increased, the concentration of larger droplets disappeared, resulting in a complete evaporation/dissipation of the fog layer. Interestingly, as a result of being optically thin, the fog layer eroded from the bottom (Fig. 9a,c), permitting sufficient surface heating to trigger an increased sensible heat flux and radiative heating over Sable.

A Tale of the Unexpected – Fog Shadow

During 1-km resolution COAMPS[®] mesoscale model simulations (Appendix H) conducted during 30 June to 31 July to support IOP forecasts, a clearing in an otherwise reduced horizontal visibility could be frequently noticed downstream of Sable Island. After 22 July, this phenomenon became conspicuous, and was dubbed *fog shadow*. Eight consecutive forecasts starting 1200 UTC 22 July consistently predicted, at least in initial runs, this [unanticipated] phenomenon. For example, in Fig. 10, a large, uniform patch of dense fog (visibility < 500 m) is visible to the east of Nova Scotia, in a clearing downstream of Sable Island.

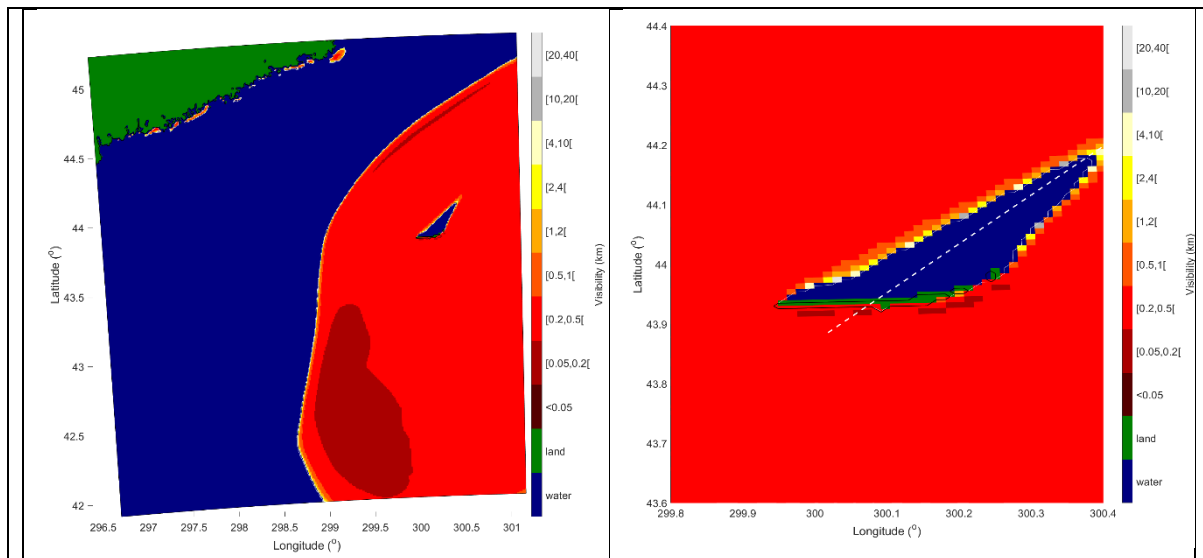


Figure 10: A 27-hour COAMPS[®] forecast of the horizontal visibility at the lowest thermodynamic level (1.5 m) valid at 15 UTC on 24 July 2022. A full innermost nest with 1 km grid spacing (left panel), and an enlarged area centered over Sable (right panel). Nests are depicted in Appendix H. The dashed white line in the right panel shows the location of the southwest-northeast vertical cross-section used for studies. A black solid line indicates coastline, and a white solid line in the left panel represents the fog (appear in red around the island) boundary. At this resolution in the innermost nested grid, Sable Island is barely resolved and the eastern flank of the island is narrower than the rest of the island. It appears as separate small islands in the model because even at 1 km the grid resolution is too coarse to resolve the actual width.

An in-depth analysis of fog shadow, including hindcasts using finer, sub-1-km horizontal grid spacing will be presented in Gaberšek et al. (2024). The investigator zeal

following the observance of fog shadows in simulations led to a super-IOP (IOP10) on the 23 July. In addition, fortuitously, R/V-Condor was slated to sail southward on the 22 July to make its final N-S transect south of Sable Island across the Gulf Stream, and an intrepid decision was made to change its course for a coordinated [sub]campaign between SI and R/V-Condor crews to hunt for the fog shadow.

During IOP10, the fog shadow was unequivocally observed, mostly in the early afternoon, by instrumentation at Sable Island and in satellite imagery, with its streamwise length close to the predictions (Appendix I). Two mechanisms of fog-shadow genesis were hypothesized, namely: (i) evaporation of fog during (adequate) land surface heating, and (ii) increased turbulence as a result of the development of IBLs at the leading and lee edges of Sable. Extensive observations supported the former (discussed in Bardoel et al. 2024), and thus the fog shadow here appears to have similarities to fog holes over urban areas due to heat island (Gautam & Singh 2018; Theethai et al. 2023).

The R/V-Condor arrived northeast of Sable at the wee hours of 26 July to begin IOP11/ISP5 sub-campaign, named “Sable Lee Observing Period (SLOP)” wherein synchronized rawinsonde launches were made, 38 each, from the Sable Island and R/V-Condor. Fig. 11(a-c) provides a measurement summary of SLOP. The data prompted a unique case study of IBLs in the presence of fog and highly localized surface heterogeneity at coastal margins.

While the ship was enroute toward Sable, disappointingly, the 24 July forecast made for the 26 July was reversed on 25 July, to a no-fog/shadow day, which was prescient. On the Sable, the visibility was in the ‘mist’ regime until 1000 UTC 26 July and the same with occasional fog patches prevailed at R/V-Condor (Fig 11e). Thereafter, the visibility at both the ship and Sable was high (~ 5-15 km), indicating no fog shadow. Fog appeared on Sable at 2100 UTC 26 July but with high visibility on the ship until 0100 27 July UTC, thus suggesting a different fog-shadow genesis mechanism than the land heating mechanism above. The ship and Sable captured horizontal (positive) gradients in visibility downstream of the island, which holds implications for IBL effects on fog shadow, optical propagation, and fog-surface interactions. The synoptic conditions, rather than local thermodynamics (Sable heating), seemingly played a decisive role in fog-shadow suppression on 26 July. More details of SLOP study will be presented in Ortiz-Suslow et al. (2024).

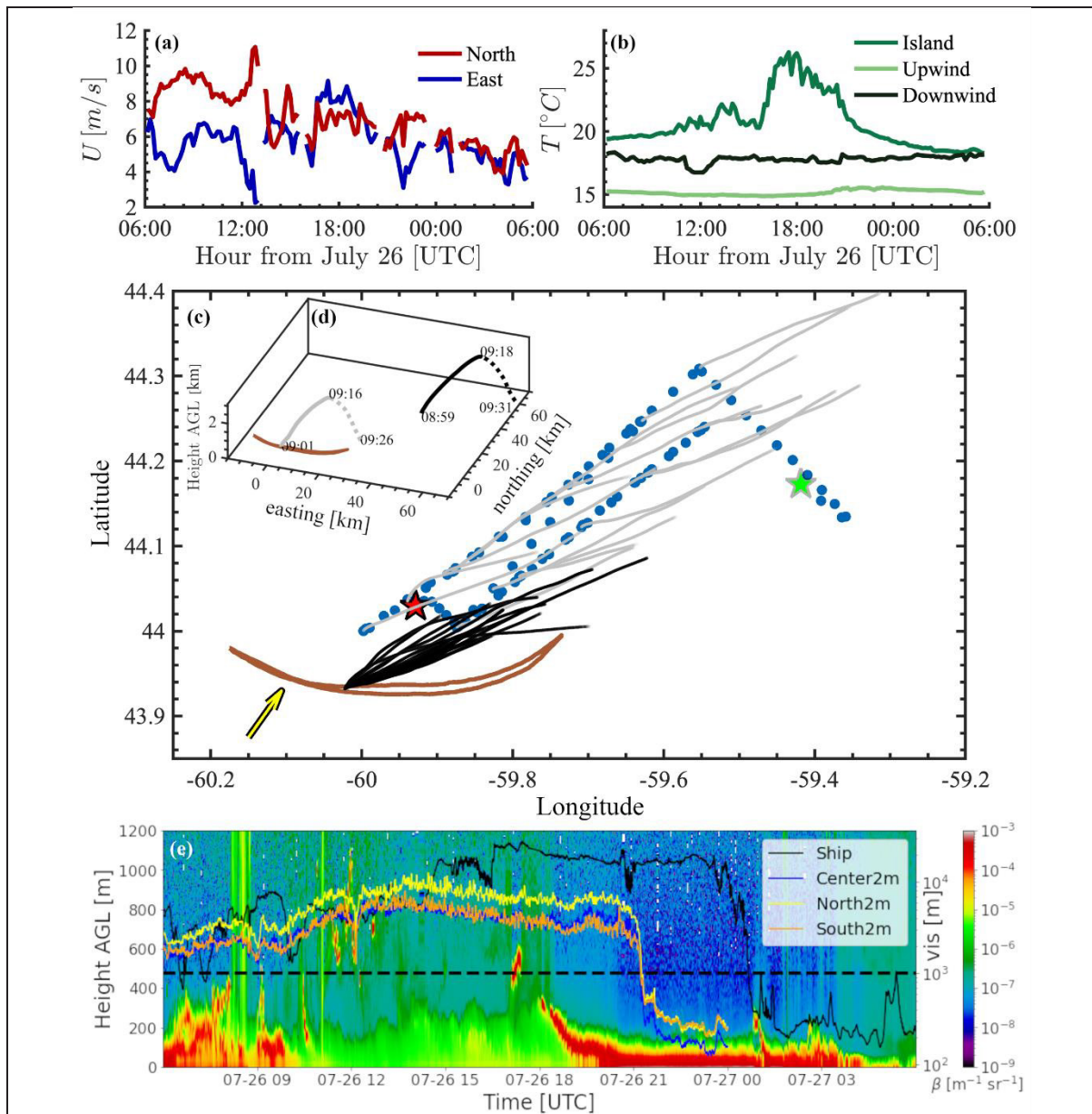
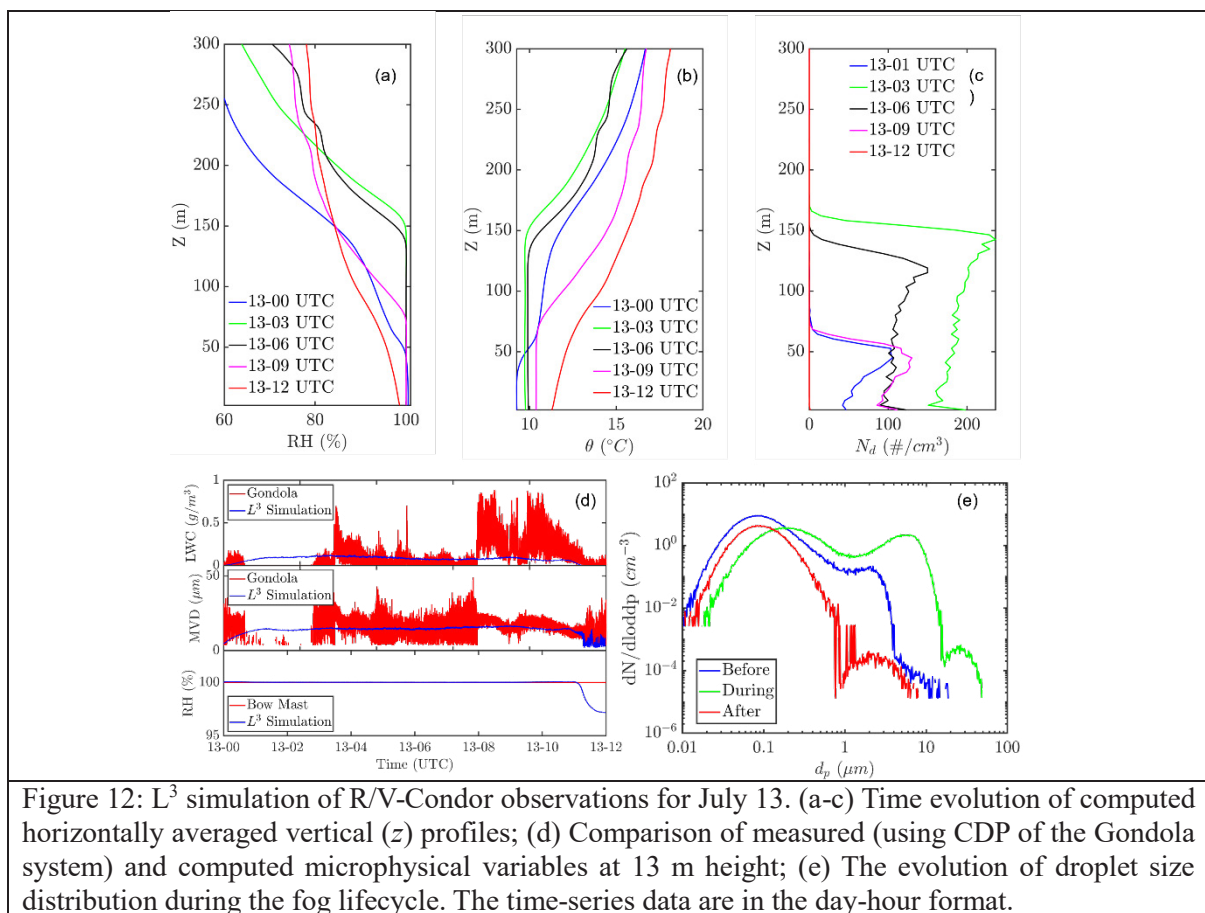


Figure 11: An overview of SLOP case study, 0600 UTC 26 July to 0300 UTC 27 July. (a) From the R/V-Conдор bow mast, southwesterly surface winds driven by low level jet that builds through the local morning and then diminishes steadily through the remainder of the IOP was observed; (b) Surface T records from Sable (radiometric skin T, corrected for DWR), a small wave buoy 3 km south of the island (upwind, thermistor on the buoy hull 10 cm from the surface), and R/V-Conдор (downwind, radiometric skin T via ROSR); (c) Overview of the sampling downstream of Sable, with R/V-Conдор track marked in blue circles. Stars denote the beginning (green) and end (red) positions. The grey/black lines show rawinsonde trajectories from the ship/island, which were deployed in an up-down ABL mode using the controlled leak technique. The black (encircling a white) arrow shows the mean surface wind vector from the ship's bow mast; (d) An example of the coordinated ship (black)-island (gray) up-down rawinsonde launches with distances from West Light station of Sable (brown). (e) Ceilometer backscatter with altitude from R/V-Conдор (colormap) overlaid by FD70 visibility at the ship and PWD-22s on Sable towers.

Fog Microphysics via High Resolution Simulations

A Large-Eddy Simulation (LES) combined with large-scale dynamics (LSD) and Lagrangian Cloud Model (LCM) -- acronymized L^3 coupling -- was used to simulate selected

fog events. As an example, simulation for July 13 (ISP1) is discussed below, with model details briefly in Appendix J and in Barve et al. (2024). At the simulation time, R/V-Condor was on the Hibernia Grid (defined later in Fig.13a). The computations were initialized at 2100 UTC on 11 July with initial meteorological conditions derived from ERA5 (Hersbach et al. 2023). The initial aerosol distribution was approximated as bimodal, the sum of two lognormal distributions with $N_d = 800 \text{ cm}^{-3}$. The simulations continued until 1500 UTC on 13 July. As for observations, the 12 July showed shallow, intermittent (<50 m thick) fog, with visibility fluctuating above and below 1 km, whereas on the 13 July fog was continuous. Figs. 12(a-c) show the computed evolution of horizontally averaged RH, potential temperature (θ) and N_d profiles. Computed LWC, mean volume diameter (MVD) and RH vis-à-vis the direct measurements at R/V-Condor for 13 July are shown in Fig 12(d).



The simulated fog onset occurs ~ 0100 UTC, defined by $LWC > 0.01 \text{ g m}^{-3}$ and RH approaching 100%. This is earlier than the recorded observations (0300 UTC). Notwithstanding, the model well replicates the observed fog dissipation time ($\sim 11:00$ UTC). According to Fig. 12a, fog was initially confined near the surface (<50 m), but later the longwave radiative cooling at the fog top led to top-down convection, contributing to the growth and homogeneity of fog layer, which peaked at 150 m thickness. Fig. 12(e) presents the

evolution of droplet size distribution, which was bimodal before and after the fog, but a third peak (at $\sim 8 \mu\text{m}$) emerged during fog, indicating the activation of the accumulation mode aerosols that are responsible for increased LWC. Overall, the general consistency of field observations and simulations of LWC, MVD and RH trends indicate the promise of L^3 as a simulation tool.

Nexus of Continental Shelf Turbulence and Fog

Guided by the hypothesis that enhanced turbulence over shelf or shelf break favors fog formation due to intensified air-sea interactions and lateral mixing (see Appendix A), and since limited measurements during 2018 C-FOG field campaign to the south of Nova Scotia could not fully verify this hypothesis (Lozovatsky et al. 2021), further measurements were conducted in the Hibernia region of Newfoundland shelf and across the NS shelf not far from the Sable and toward the Gulf Stream cold wall. Up-rising VMP-250 was used for hydro-physical and turbulence measurements at 68 stations (Fig. 13a). The data analysis on the Hibernia Grid reported here consisted of shelf and shelf break stations.

Characteristic station averaged profiles of temperature $T(z)$, salinity $S(z)$, and buoyancy frequency $N^2(z)$ and the profiles of TKE dissipation rate ε and eddy diffusivity estimated using $K_N = 0.2 \varepsilon / N^2$ (Lozovatsky et al. 2021) are shown in Fig. 13b. The near-surface turbulence on the shelf break ($\varepsilon \approx 10^{-5} \text{ m}^2 \text{ s}^{-3}$, $K_N \approx 10^{-1} \text{ m}^2 \text{ s}^{-1}$) was weaker compared to that on the shelf ($10^{-4} \text{ m}^2 \text{ s}^{-3}$, $1 \text{ m}^2 \text{ s}^{-1}$). The cumulative distribution functions of the diffusivity $\text{CDF}(K_N)$ calculated using data sets of 8 shelf (over the depth range $-65 < z < -30 \text{ m}$) and 5 shelf break ($-90 < z < -30 \text{ m}$) stations, with depth ranges encompassing the thermocline, could be approximated by the generalized extreme value distributions, as was for the NS shelf (Lozovatsky et al. 2021), but parameters of the distributions were drastically different (not shown). The median diffusivity for the Hibernia shelf was $4.1 \times 10^{-6} \text{ m}^2 \text{ s}^{-1}$, only slightly below the shelf-break diffusivity $5.3 \times 10^{-6} \text{ m}^2 \text{ s}^{-1}$, and both were much lower than diffusivities at the Nova Scotia shelf ($3 \times 10^{-5} \text{ m}^2 \text{ s}^{-1}$) and shelf break ($5.8 \times 10^{-5} \text{ m}^2 \text{ s}^{-1}$) during C-FOG. RV-Condor encountered fog recurrently within the Hibernia grid (see ISP1 and ISP2), but a definite association of fog prevalence and surface or thermocline turbulence awaits further data analysis.

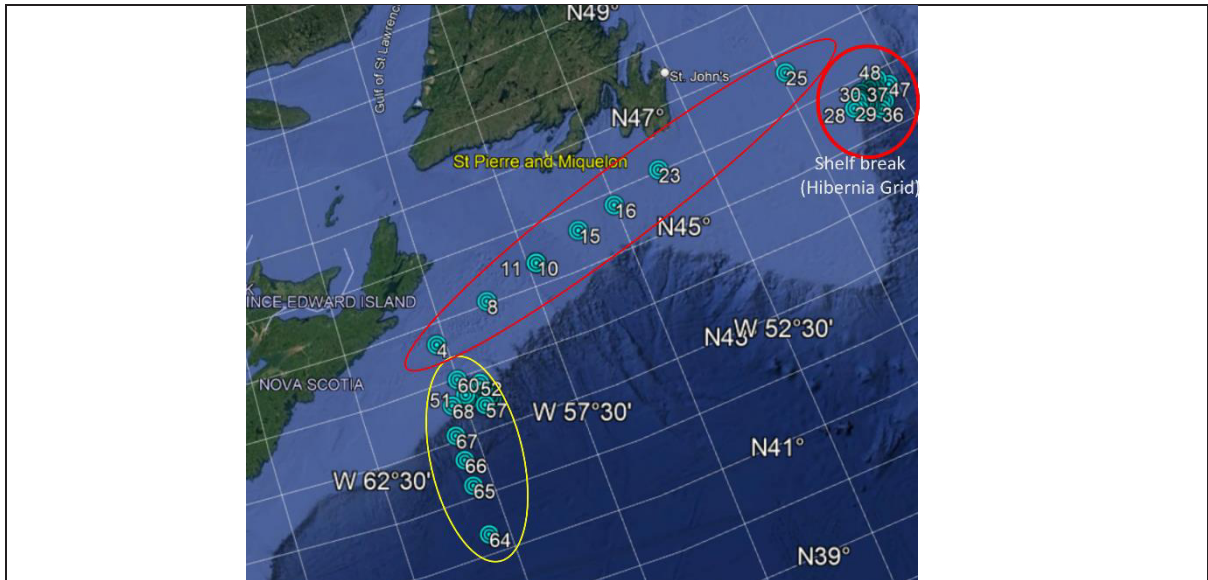


Figure 13(a): Locations of VMP-250 stations covered by R/V-Condor. Stations 4-48 were covered during 8-16 July, with Stations 4-25 (lighter red ellipse) on the shelf, and 26-48 (dubbed Hibernia Grid; dark red circle) on both the shelf and shelf break. R/V-Condor entered Hibernia Grid on ~ 09 July 0600 UTC and left 16 July 1900 UTC. July 21-31 covered stations 50-68 (yellow ellipse) in the Sable area. Within the Hibernia Grid, shelf stations (26, 27, 29-31, 40, 41, and 44) and shelf break (28, 32, 39, 45 and 48) were separately analyzed. Some station numbers are not legible because of overlap.

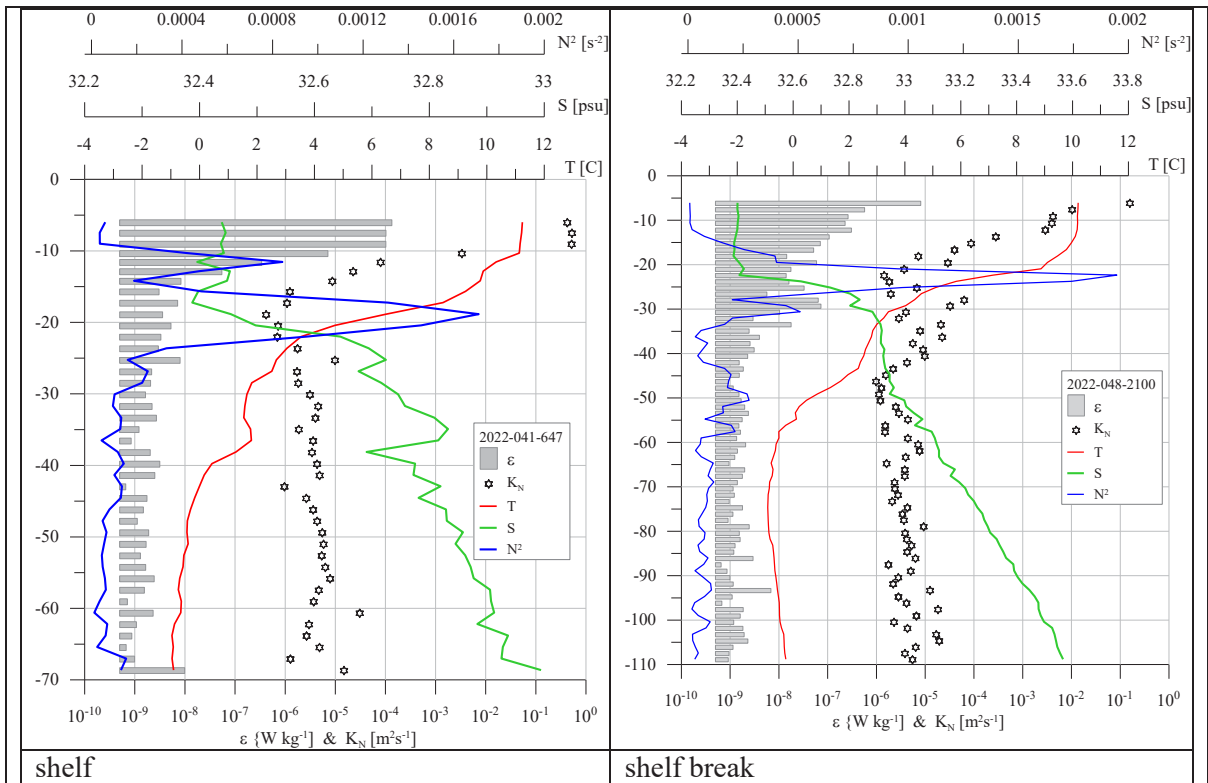


Figure 13b: Stratification profiles T , S , N^2 and turbulent variables ε and K_N at the Hibernia grid (for details see Figure 13(a)). The vertical axis is the depth (in m) below the mean sea surface located at $z = 0$. The T , S , and depth (z) are from the VMP-250, and ε was evaluated using shear profiles. K_N was calculated using the standard techniques (Lozovatsky et al. 2021).

Exploring Frontier Technologies

The following are examples of novel measurement technologies attempted during Fatima-GB: (i) Simultaneous vertical profiling of microphysics and turbulence above the sea surface using C-CAMS (Fig. 2), and (ii) the Super Combo (Fig. 3h,i) for the measurement of TKE (at K scale) and temperature fluctuations dissipation (O-C scale).

C-CAMS

A major design challenge of C-CAMS was to obtain a motion-stable platform to safely mount research-grade sensor payloads of larger size, weight, and power supply tethered to a crane wire to allow sampling at different heights above the sea level at a distance uninfluenced by the ship hull. The solution was a reinforced fiberglass pallet container mounted with a horizontal 10-ft tower section to overhang meteorological instrumentation above the ocean surface. The instrument suite characterized the near-surface visibility, meteorology, thermodynamics, turbulence and microphysics. C-CAMS measurements on 14 July 2022 (Super IOP5) are shown in Fig. 14, highlighting its capability of sampling a range of variables. Also overlaid are the data from D-CAMS (deck-mounted version of C-CAMS) and from the ship bow mast to extend the vertical data coverage.

The visibility measurements show that fog extended above the level of D-CAMS. In fog, C-CAMS visibility increased toward the surface. Of interest are a stably stratified surface layer ($\bar{\theta}$ profile) accompanied by an increase of water vapor with height in both clear and foggy conditions. Since the clear condition is at near saturation (RH = 95-98%), significant increases of T with height resulted in an ‘anomalous’ vertical gradient in the mixing ratio r under stable clear condition, and the increase of r with height is consistent with observed negative latent heat fluxes. In the fog case, the near-surface upward water vapor fluxes are at odds with previous measurements, which call for further study by invoking the role of stable-stratification. Large negative sensible heat fluxes were identified in both conditions, consistent with the stable T gradient near the surface. Significant vertical gradients are evident for all three fluxes, particularly for the momentum flux, in both fog and clear conditions, a clear violation of the constant flux surface layer assumption. Further details on C-CAMS will be presented in Yamaguchi et al. (2025).

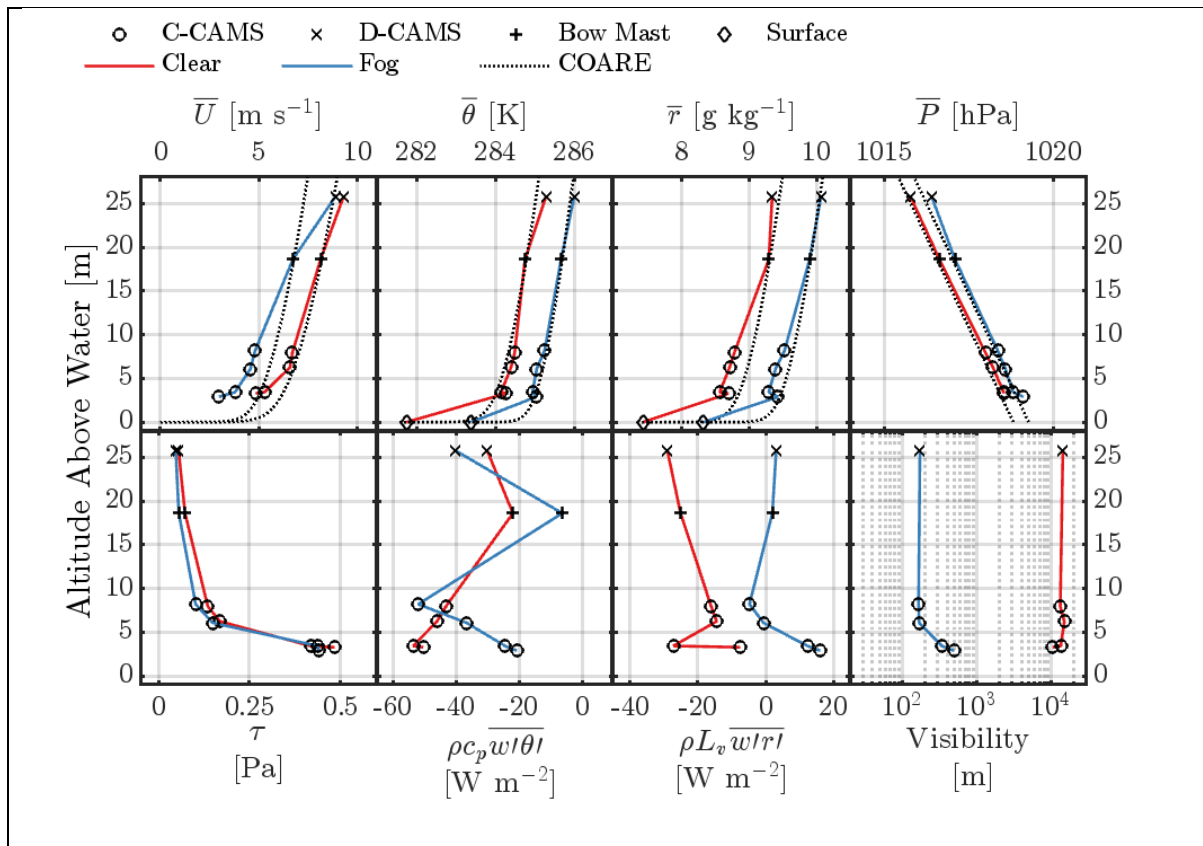


Figure 14: C-CAMS measured vertical profiles of bulk meteorological parameters (mean values of wind speed \bar{U} , potential temperature $\bar{\theta}$, water vapor mixing ratio \bar{r} , pressure \bar{P} , momentum flux τ , sensible heat flux $\rho c_p \overline{w'\theta'}$, latent heat flux $\rho L_v \overline{w'r'}$ and visibility (For C-CAMS details, see Fig. 2, et seq.). The figure shows measurements (circles) on 14 July 2022 during clear (red) and foggy (blue) conditions at 16:02 UTC and 19:50 UTC, respectively, during the nominal 1-hour deployment periods. The bow-mast (+) and D-CAMS (x) data are added to extend the altitude to 18.6 m and 25.4 m above the water level, respectively. The bow-mast and D-CAMS data are time-averaged over the entire C-CAMS sampling period, while each C-CAMS datapoint represents 10 mins averaging during stable and level sampling at three discrete heights. As well, the SST and derived sea surface mixing ratio are shown in the $\bar{\theta}$ and \bar{r} profiles. The bow-mast and shipboard ROSR data were used as inputs to the COARE 3.0 algorithm (Fairall et al. 2003) to obtain canonical mean profiles shown with dotted lines in the top row.

Super Combo – A Probe System for Penetrating Dissipation Scales of MABL Turbulence

The ‘Super Combo’ (Figs. 3h,i) is an assemblage of high-resolution probes for simultaneous direct measurement of dissipating (K and O-C) microscales, with additional information retrievable on LWC, MVD and N_d . The probe system was on a gimbled platform, controlled by a neural network to align the probes in the wind direction, a requirement for hot-wire probe operation (Kit et al. 2017). All hot-wires were operated in constant temperature anemometry (CTA) mode. The technique developed by Goldschmidt & Householder (1969) for wind tunnels was adopted that converts voltage fluctuations needed by CTA to maintain its temperature upon impaction of droplets into droplet parameters.

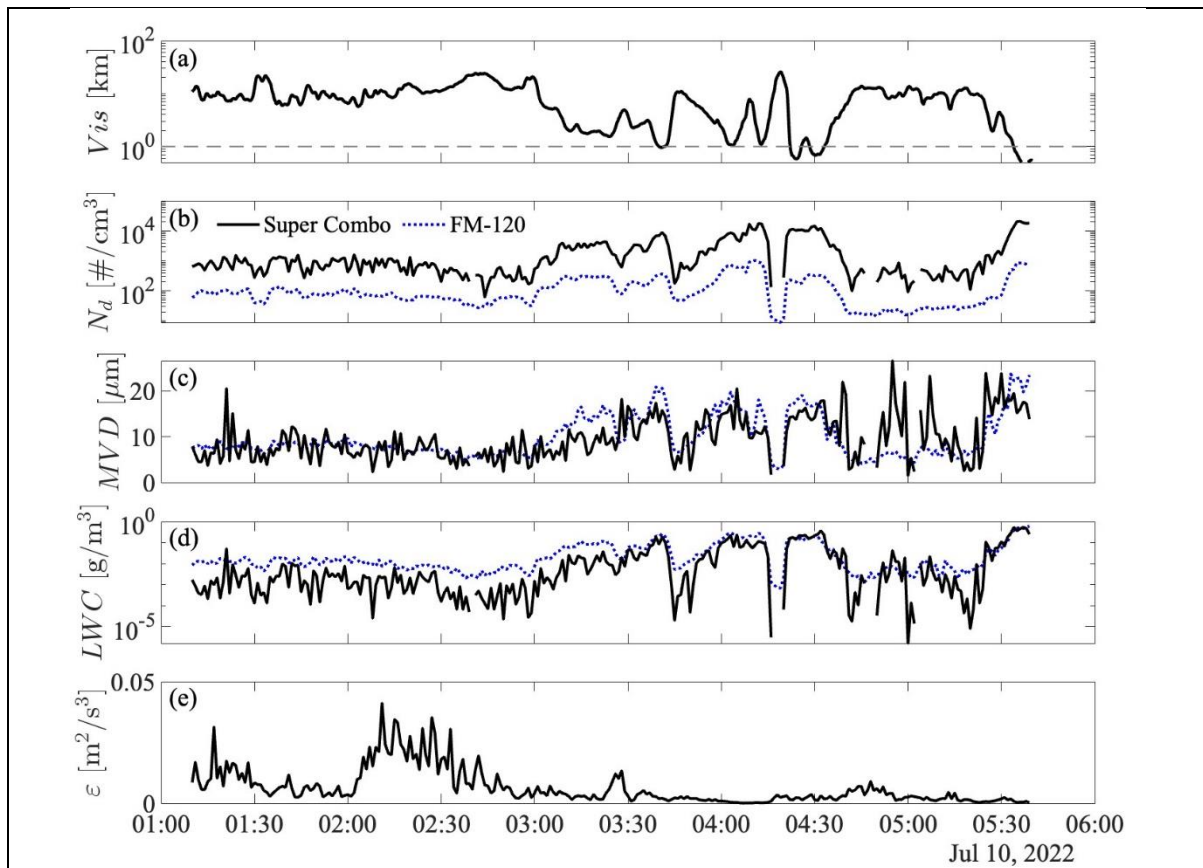


Figure 15: The Super Combo system uses a sonic anemometer to measure larger-scales and a fine-wire probe assembly on a platform that rotates to align with the flow direction to measure the turbulence. The probe assortment consists of high-resolution sensors – two X-wires (TSI 1241-20-film), one parallel array probe (Dantec 55P71-film), and two nano-scale cold-wires (T-NSTAPs) – all collocated with a sonic (RM Young 81000). Shown in the figure are the Visibility (Vis) from FD70 (a) and representative time-series measurements from the Super-Combo system taken on 10 July (IOP3). Gray dashed line in (a) represents the threshold visibility 1 km. For comparison, data from FM120 are included in (b, c, d) with dotted lines. Super combo can resolve droplets ($\sim 1 \mu m$) smaller than that by FM120 ($\sim 2-5 \mu m$), and hence the measurement disparity. As expected, low Vis corresponds to higher N_d and lower levels of turbulence.

Fig. 15 shows a representative dataset of one-minute averaged visibility (teetering at the fog threshold), directly-measured TKE dissipation rate ε and microphysical parameters. Compared with conventional instruments, FM120 in particular, the Super Combo is able to capture trends of microphysical parameters at a higher space-time resolution. Measured MVD and LWC are on comparable scales with FM120. The Super Combo gives N_d approximately one order of magnitude higher than that by the FM120, likely due to its higher sensitivity to small droplet sizes. Further details will be presented in Huang et al. (2024).

Summary and Challenges

Prediction of marine fog is one of the most challenging endeavors in meteorology, due mainly to strong (bio)physicochemical interactions spanning 15-decades of space-time scales that underlie its lifecycle. Paucity of knowledge, lack of adequate relevant high-fidelity data

due to measurement difficulties across synoptic to submicron scales in logistically challenging environments, and non-stationarity and inhomogeneity of marine fog have stymied the progress in fog research, notwithstanding important applications of fog forecasting in transportation, agriculture, industrial and defense sectors. Fatima-GB was a comprehensive multidisciplinary field campaign augmented by NWP modeling and high-resolution (research-grade) simulations to study fog in shallower, non-coastal waters -- categorized as Sea Fog. The study mainly covered the Grand Banks area on North Atlantic shelf, one of the foggiest places on Earth in the summer. Access to an isolated islet (Sable Island) south of Grand Banks, located in the advection pathway of warm Gulf-Stream air toward colder Grand-Banks water conditioned by Labrador current, helped study both sea fog lifecycle and fog-turbulence-land interactions. A ship (R/V-Condor) and the Sable Island were densely instrumented with an unprecedented array of sensors that collected extensive set of data. Some novel sensors/sensor-systems were among those deployed. Data analysis showed that the long-held hypothesis that advection of warm air over colder water causes marine fog was oversimplistic, and a synoptic trigger (e.g., moving high-low systems) is needed for fog genesis. Upper-ocean turbulence measurements cast another hypothesis into doubt, that [intense] shelf-break turbulence may favor air-sea interactions and Sea Fog. Study of cloud lowering events shaped by low-level convergence/divergence illustrated the importance of finer details of meteorological and turbulence structure, highlighting the role of sub-grid microphysical processes of NWP in predicting Sea Fog. First ever long/short wave radiation balance measurements at the fog top using an instrumented tethered balloon system opened up new avenues for future numerical/theoretical studies on fog-top convection and its interaction with surface turbulence during fog evolution. FCNs are imperative for fog, and chemical analyses illustrated that 1-100 micron sized coarse (hygroscopic) Sea Salt Aerosols facilitated Sea Fog but were removed by scavenging during fog evolution, leaving behind compounds that might have formed due to chemical reactions between gases and interstitial aerosols. Novel bioaerosol sensors adumbrated some association between hydrometeors and bioaerosols, and broached future opportunities for delineating the role of (~ 10 nm scale) bioaerosols as FCNs, a topic that has invited debate. Overall, accounting for such biochemophysical processes in microphysical schemes of NWP models will be a captivating research topic for the future. Prompted by NWP modeling, a coordinated sub-campaign between the groups at Sable Island and R/V-Condor uncovered the “Fog Shadow” phenomenon - a clearing in the wake of an island in an otherwise foggy area. The existence of a tens of km sized fog shadow behind the ~ 1 km long Sable Island was confirmed for some days. Fog shadow was a result of differential surface

heating between the island and surrounding ocean, but was sensitively modulated by synoptic conditions and internal boundary layers. While COAMPS® modeling was the first to elicit fog shadow, the onset and disappearance times of fog shadow in model had disparities with observations, which is a topic for future research.

Acknowledgments

Fatima-GB was an ambitious ‘big-science’ project that was only possible through international scientific cooperation, involvement of a bevy of diverse, skilled and dedicated personnel, munificent support of many organizations, and a special multidisciplinary funding mechanism. Daniel Gibson, Rodrigo Menafrá, Gregory Siddall and Scott Simone of Canadian National Network of Centers of Excellence (MEOPAR) shepherded the utilization as well as conversion of deep-sea supply vessel Atlantic Condor to a research vessel. ONR Naval Vessels Program Manager Rob Sparrock facilitated renting of the vessel. The support and beneficence of Jason Surette (Operations Manager) and his colleagues (Mathieu D’Astous, Greg Stoud and Sarah Medill) at the Sable Island National Park Reserve were vital for the Sable Island campaign. The Sable Science Lead Cornelia (Nell) den Heyer of the Bedford Institute of Oceanography for Fisheries and Oceans, Canada helped gaining access to electricity and accommodation resources at the island. Brilliant logistician Marvin Willis carried a heavy load, from renting a hangar at the Halifax Airport as the operations center to arranging charter flights, helicopters and sea-lift/barges (from Sable Air and Air Borealis, Vision Air and Dominion Diving, respectively) to timely replenishing of food supplies and hardware at the Sable Island and R/V-Condor. He was joined by Paul LeBlanc, who resided partly at Sable Island, to ensure smooth operations. Shawn Quinn of Compliance in Motion Inc. (CiM) was relegated with safety and compliance of transported items. Reno Sit of ECCC led instrumented UAV operations, and Alexis Trottier-Pacquet, Evan Newman Lauren Robinson, Phillippe Gauvin-Bourdon, Baban Nagare and Minghong Zhang were part of the Fatima support group. This work was funded by the Grant N00014-21-1-2296 of the Office of Naval Research (see Appendix A). Additional support was provided by the Wayne and Diana Murdy Fund at UND and the administrations of UND and UU. Finally, our sincere appreciation to ONR Program Managers Dan Eleuterio (who also contributed to this manuscript), Josh Cossuth and Kate Mulreany for their crucial assistance in numerous ways.

Sadly, one of the Fatima team members, Professor Iossif Lozovatsky, who prepared Fig. 13, passed away unexpectedly on 23 December 2023. We dedicate this paper to his memory and celebrate his contributions to Physical Oceanography over the past four decades.

Availability Statement

The data used herein have been collected by four research groups (UND/ PSL-NOAA, NPS, UU, Scripps/UCSD) consisting of PIs as well as five collaborating groups (DU, YorkU, AFIT, UMAN, OntTechU); see Appendix A for acronyms. All data are available in a single shared google drive at UND with metadata. A backup drive is also maintained. After an embargo period for the PIs to conduct research, all data will be able to scientific community after 01 August 2025, unrestricted. This data base includes raw, intermediate and QC/QA data, COAMPS® and WRF hourly outputs (plots), satellite data and daily weather forecasts from multiple sources.

Appendices

Appendix A: General Project Information and Summary Hypotheses

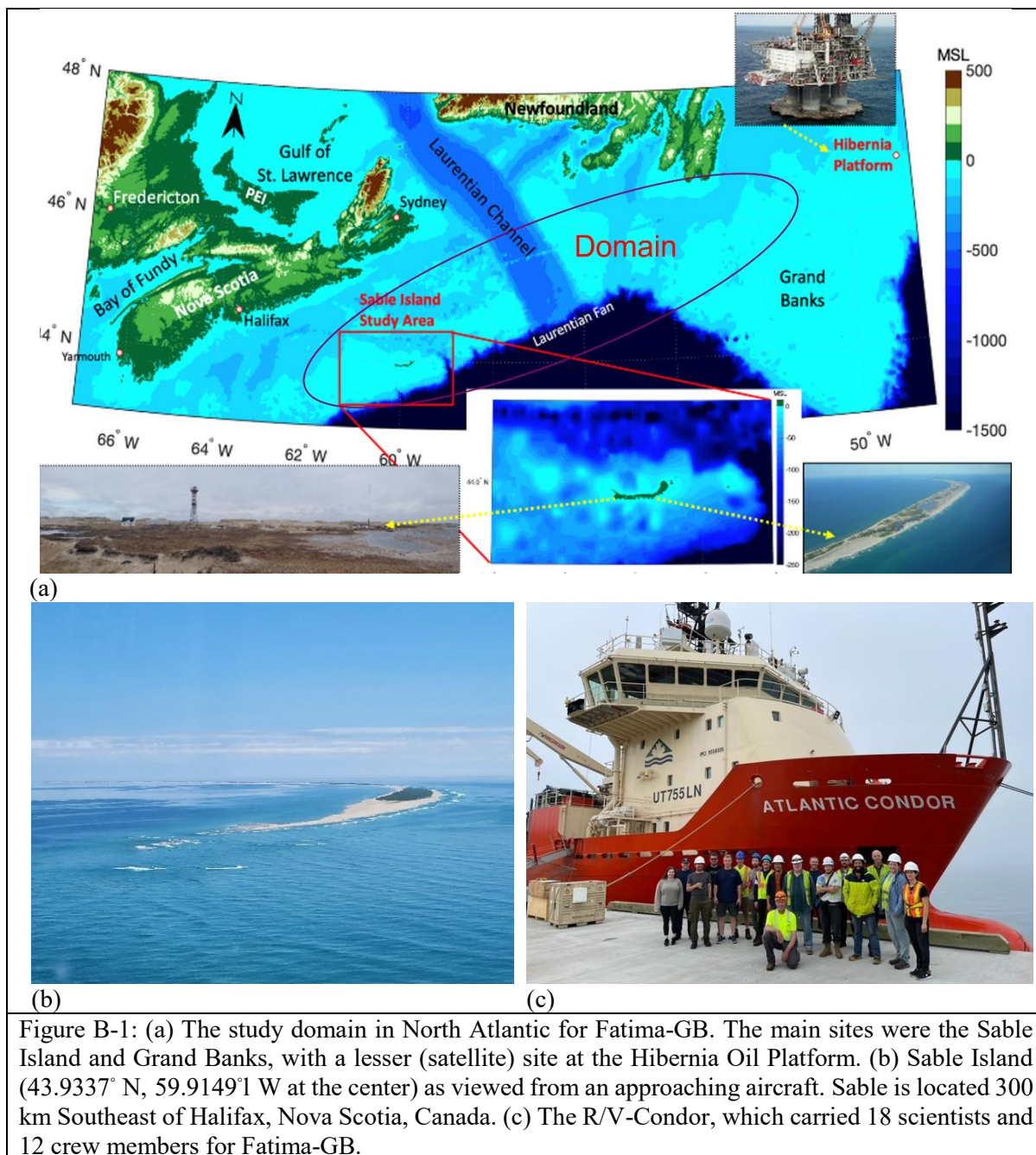
The Fatima project seeks leaps in the fundamental understanding of Sea Fog (SF) via multidisciplinary research. It was funded under a Multidisciplinary University Research Initiative (MURI) of the Marine Meteorology and Space Weather Program of the Office of Naval Research (2021-2026). The *Objectives* are to understand and quantify processes underlying the lifecycle of SF, and represent them in NWP models via: (i) deploying leading-edge instrumentation, including novel measurement technologies, to probe from synoptic to smallest scales of ABL turbulence (i.e., K and O-C scales $\sim 1\text{mm}$) and aerosols ($\sim 10\text{-}100\text{ nm}$); (ii) theoretical/numerical analyses of two-phase turbulence; (iii) delving into droplet/aerosol microphysics and dynamics, thermodynamics, surface processes and forcing; (iv) developing microphysical parameterizations for improved visibility predictions using NWPs; and (iv) studying impacts of fog on electro-optical propagation. Seven guiding hypotheses were used: (1) Warmer humid airflow along negative SST gradients, in collusion with sea-surface cooling by air-sea fluxes, provide favorable conditions for SF. Air-sea interactions is abetted by enhanced upper oceanic turbulence (e.g., shelf/shelf-break mixing). Synoptic forcing on ABL is also a key factor; (2) Unlike for low-level (e.g., stratocumulus) clouds, sea-surface processes control fog lifecycle through air-sea fluxes and ABL dynamics (in particular, wave boundary layer, LW/SW radiation and shear). FCNs are significantly contributed by sea surface aerosols (SSA) produced by wave breaking; (3) Precipitation from clouds above the fog layer has profound impacts on SF lifecycle by moistening the sub-cloud layer, scavenging fog droplets, suppressing SSA production and modifying surface waves and turbulent fluxes;

- (4) While synoptic to microscales strongly affect SF genesis, a critical (rate determining) step is outer (integral) scale eddies feeding TKE to K scales via Kolmogorov (nonlinear) energy cascade down the inertial subrange. It is within K eddies that temperature/moisture homogenizes and spawns fog droplets around embedded FCNs by vapor deposition under specific conditions;
- (5) Radiative cooling and heating are crucial for the lifecycle of SF through their link to microphysical and turbulence processes.
- (6) Optical attenuation in fog can be parameterized using fog-integrated microphysical and turbulence parameters.
- (7) A two-wavelength microwave MW and near infra-red NIR scintillometer can be used to infer microphysical properties of fog, forms of precipitation, and evolutionary stages of fog.

Fatima enlists a multidisciplinary team of researchers for melding theory, simulations, field observations, technological developments and NWP modeling. It is led by five Universities: University of Notre Dame (UND), Naval Postgraduate School (NPS), Scripps Institute of Oceanography, University of California, San Diego (Scripps/UCSD), University of Utah (UU), and University of Minnesota (UM). Collaborating institutions from the US are the Airforce Institute of Technology (AFIT), Argonne National Laboratory (ANL), Army Research Laboratory (ARL), Pacific Northwest National Laboratory (PNNL) and the Physical Sciences Laboratory at NOAA (PSL-NOAA). The international participants are: Bedford Institute of Oceanography (BIO), Canada; Dalhousie University (DU), Canada; Digital Environment, WSP, Canada (WSP); Korea Institute of Ocean Science and Technology (KIOST), Republic of Korea ROK; University of Manchester (UMAN), UK; Ontario Technical University (OntTechU), Canada; Yonsei University (YU), ROK; and York University (YorkU), Canada.

Appendix B: Grand Banks and Sable Island – Domain Covered by R/V

A backdrop of Fatima-GB campaign with ocean and land domains covered is shown in Fig. B-1, including measurement platforms.



Appendix C: Instrument Layout at Sable Island

An extensive array of instruments at Sable was packed into two clusters, as shown in Fig. C1.

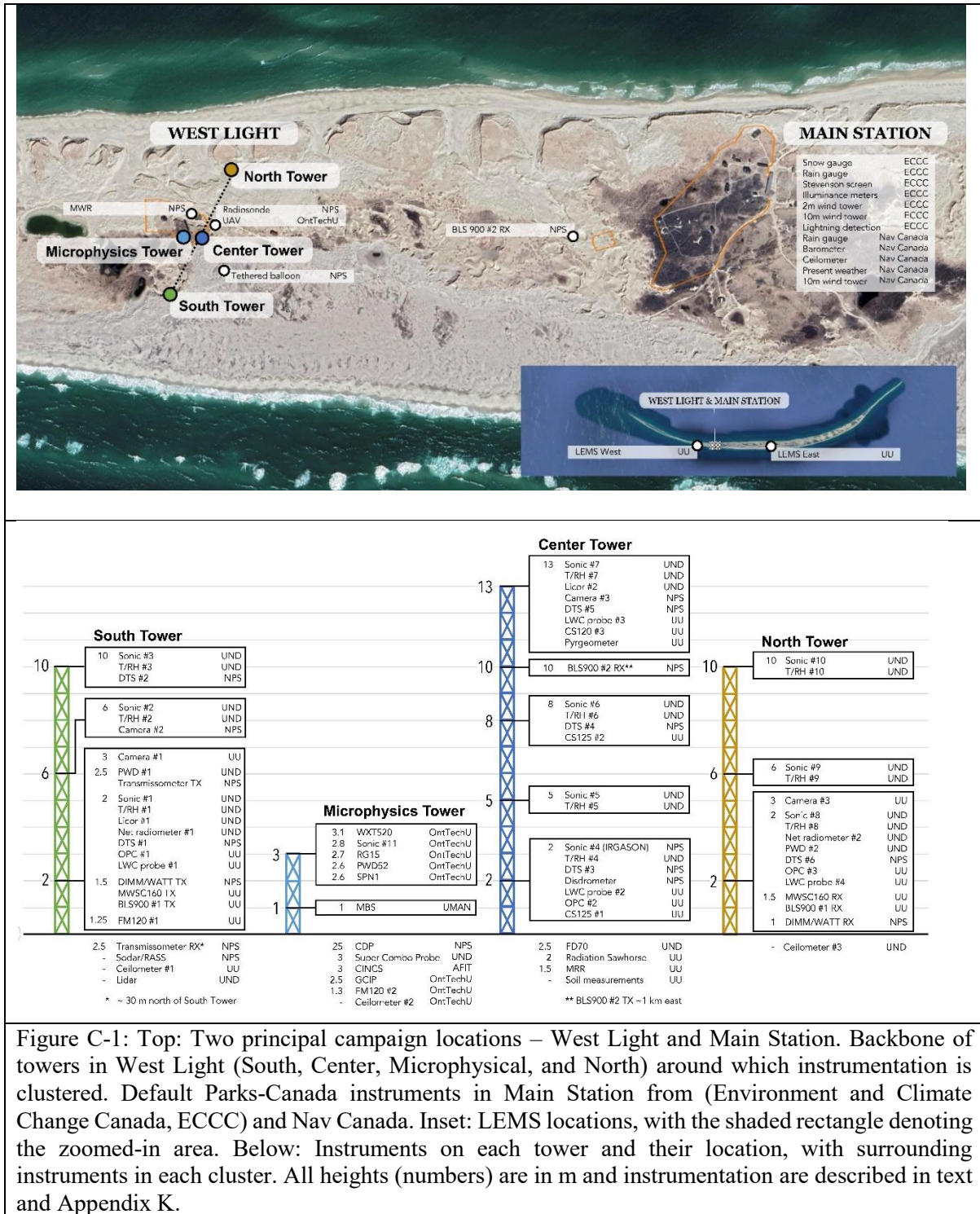


Figure C-1: Top: Two principal campaign locations – West Light and Main Station. Backbone of towers in West Light (South, Center, Microphysical, and North) around which instrumentation is clustered. Default Parks-Canada instruments in Main Station from (Environment and Climate Change Canada, ECCC) and Nav Canada. Inset: LEMS locations, with the shaded rectangle denoting the zoomed-in area. Below: Instruments on each tower and their location, with surrounding instruments in each cluster. All heights (numbers) are in m and instrumentation are described in text and Appendix K.

Appendix D: Hourly Aerosol Concentration Statistics

The 25th percentile (p25), 50th percentile (p50), 75th percentile (p75), mean, and standard deviation (std) of hourly aerosol concentrations for aerosols with diameter larger than 10, 100 and 200 nm during fog and no fog at R/V-Condor are presented in Table D1.

Table D1: Statistical data on hourly aerosol concentration

#/cm ³	N_10_fog	N_10_nofog	N_100_fog	N_100_nofog	N_200_fog	N_200_nofog
	Fog	No fog	Fog	No fog	Fog	No fog
p25	329	358	125	152	33	44
p50	565	828	251	317	85	74
p75	904	1229	448	517	129	115
mean	630	831	300	361	91	94
std	349	517	207	255	66	75

Appendix E: WRF Simulation of IOP1, Illustrating Synoptic Influence on Fog Genesis

Following the identification of synoptic trigger in fog formation during IOP1, WRF V3.9.1 with the Advanced Research WRF (ARW) dynamical solver (Skamarock et al. 2008) was used for detailed studies of relevant physical processes. Therein, six Lambert projection nested domains with parent-to-child horizontal resolution ratio of 3:1 and resolution from 40.5 km to 500 m were used. Modifications were made to the static data of topography and land use to accurately capture the details of Sable Island. Two arc-second digital elevation datasets were implemented: Shuttle Radar Topography Mission SRTM 1 (NASA; <https://lta.cr.usgs.gov/SRTM1Arc>) and North American Land Cover Monitoring System NALCMS_2015_30m data (USGS; <http://www.cec.org/nalcms>). The NALCMS 19 classes were adapted to the modis_landuse_20class_30s_with_lakes land cover data; for a full description of general procedure, see Vladimirov et al. (2018). The model was implemented with 50 pressure-based terrain-following vertical levels with more levels in the lowest 1 km. The model top was set to 50 hPa. The initial and boundary conditions were derived from the 0.25°×0.25° NCEP Final Operational Model Global Tropospheric Analyses (<http://rda.ucar.edu/datasets/ds083.3/>) with datasets available every 6 h. The option for grid nudging (fdda) was used only for the outermost domain 1 (D1) for all vertical levels. The simple ocean mixed-layer model following Pollard et al. (1972) was activated as a model option to provide SST).

The WRF physics package included: the Radiative Transfer Model parametrization (Mlawer et al. 1997) for LW and Dudhia (1989) scheme for SWR to compute radiation at every 1 min; Noah land surface model (Chen and Dudhia 2001); and the Grell-Freitas cumulus

parametrization, for the first two domains only (Grell and Freitas 2014). The same configuration was used in Dimitrova et al. (2021) covering the identical area. Therein different microphysical and PBL parametrizations were compared and the two-double-moment option of the National Severe Storms Laboratory (NSSL) microphysics scheme (Mansell et al. 2010) was found to perform better than alternative schemes tested, when used with both non-local (Yonsei University; Hong et al. 2006) and local (Mellor–Yamada, Nakanishi and Niino level-2.5 parametrizations; Nakanishi and Niino 2006) planetary boundary layer (PBL) schemes. Therefore, the same NSSL microphysics and Shin-Hong PBL schemes (Shin and Hong, 2015), coupled with Revised MM5 Monin-Obukhov surface layer scheme (Jiménez et al. 2012) were selected for Fatima-GB simulations. The new Shin-Hong PBL scheme has been developed to address the so called “grey zone” challenges by using scale aware PBL parametrizations; they implement scale-dependent vertical transport in convective conditions and vertical mixing in the stable PBL and free atmosphere.

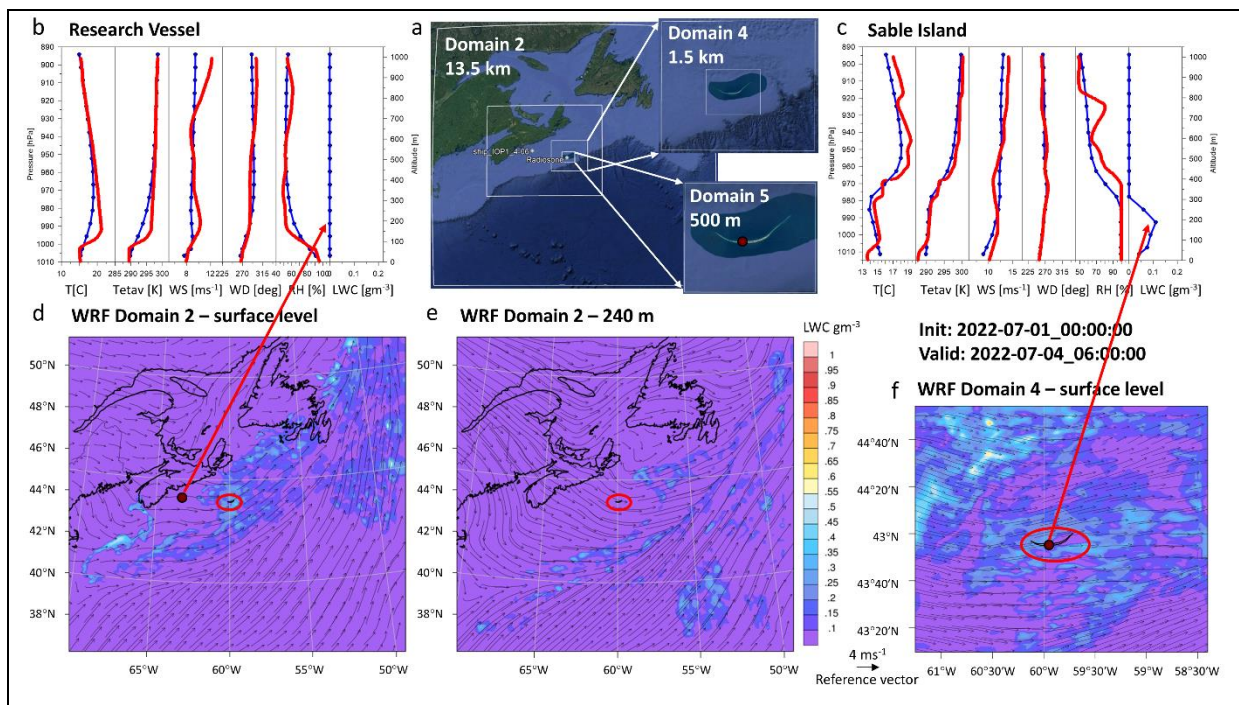


Figure E-1: (a) Domains used for WRF simulations, (b) simulated vertical profiles of main meteorological variables compared with observations from R/V-Condor located in domain 2 (red – observations, blue – simulations); (c) Observations versus simulations from Sable Island located in Domain 5; (d) horizontal sections of LWC at the surface level for Domain 2; (e) LWC for 240 m elevation for Domain 2; (f) Surface level for Domain 4 showing that LWC or fog is confined beneath an inversion layer. The surface velocity vectors are westerly/southwesterly at the Sable Island, (d, f). Simulations were started at 0000 UTC on 01 July, the plots shown are at 0600 UTC 04 July. Sable Island is encircled by a red ellipse and R/V-Condor by a red circle. No fog was observed at R/V-Condor during this IOP at SI (Fig. 4).

WRF results of IOP1 are presented in Figure E-1, in the context of synoptic triggers discussed in Fig. 7 of the paper. For brevity, a time (06:00 UTC, 04 July) between the long and short fog periods are presented. The simulation results are in reasonable agreement with the data taken at R/V-Condor and SI. Synoptic conditions prior to fog formation were a deep low-pressure center over NE Canada with a trough that extended along the Atlantic coast and over the Sable Island with strong southwesterly winds and a broad cloud band, in agreement with Fig. 7 (a,b). An eastbound ridge encroached existing surface moisture and clouds, causing fog. Fog coverage followed the line of convergence below the inversion layer (also see Hintz et al. 2024). Fog formation was most likely due to the convergence of the flow within a thin marine boundary layer topped by an inversion layer (domain 4) as discussed following the Fig. 7(d). The presence of deeper isothermal layers topped by dry inversions as a precursor to the second fog event was also evident from domain d04 simulations.

Appendix F: Delving into Recondite Bioaerosol Connection

(i) AFIT/NPS deployed CINCS, a unique instrument that was specifically adapted for bioaerosols detection. CINCS consists of two primary components: (i) Uniquely engineered Liquid Spot Sampler (LSS) that ‘gently’ ingests ultra-fine through coarse mode aerosols (ranging in size from 5nm through 10um); and (ii) Electro-chemical Detection Sensor (EDS) that employs square-wave voltammetry (SWV) and electrodes treated with antibodies specific to bioaerosol of interest (*Pseudomonas syringae* - *PS*). The LSS operates on the same principles as that associated with standard, nano-aerosol condensation particle counting CPC (Balendra et al. 2024; Deng et al. 2024). The initial SWV data as profiled in the Fig. F-1 suggest an increased presence of *PS* on 29 and 30 July as compared to the other days. It is noted that this is the very first deployment of CINCS, and to evaluate actual quantities of *PS* a controlled calibration series (say with FM120) is necessary, which was not possible in time for Fatima-GB due to scheduling conflicts.

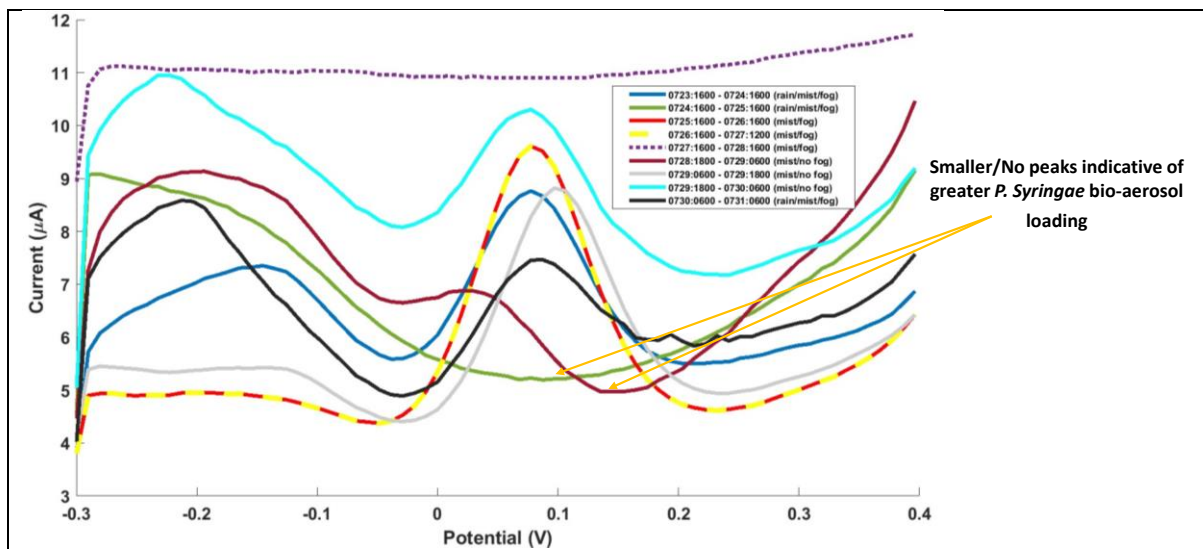


Figure F-1: Initial SWV results. Decreased and/or no peaks in the output current suggest an increased proportion and loading of *PS* in the Sable Island ambient air. Note smaller peaks (greater *PS*) on 29 and 30 July, indicating possible association of rain with *PS* population. Note that during 0727:1600 and 0728:1800 plots represent periods that SWV failed and hence anomalous SWV tests. (Time is in ADT)

(ii) The MBS deployed by UMAN detects primary bioaerosols and fluorescent aerosols in real-time via the interrogation of single particle autofluorescence and morphology. The MBS excites a single particle with a 280 nm filtered Xenon flashlamp and detects resultant fluorescent emissions over 8 channels between 305 and 655 nm. Particle size is resolved via Mie scattering of a 635 nm laser (detection range of 0.5 to 15 μm in diameter) and particle morphology is approximated via recording of two parallel chords of the 2D scattering pattern with a dual CMOS array; for a full description, see Crawford et al. (2023). Classification of particles into representative groups of interest was accomplished using the single particle fluorescent spectra, following Freitas et al. (2022). First, 3-sigma and 9-sigma thresholding is conducted simultaneously to retain weakly fluorescent populations of interest (e.g., sea spray with organic content), clipping all negative values in each channel at 0 after threshold subtraction (Crawford et al. 2020). FSSA are defined as those which exceed the 3-sigma threshold but not the 9-sigma threshold; HFSSA exceeds the 9-sigma threshold where the maximum intensity is not observed in the 2nd channel; and PBAP exceed the 9-sigma threshold with the maximum intensity observed in the 2nd channel. Particles which do not exceed the 3-sigma threshold are classified as non-fluorescent. A timeseries of the different classes is then produced using a 5-minute integration period, which is shown in Fig. F-2 (a,b).

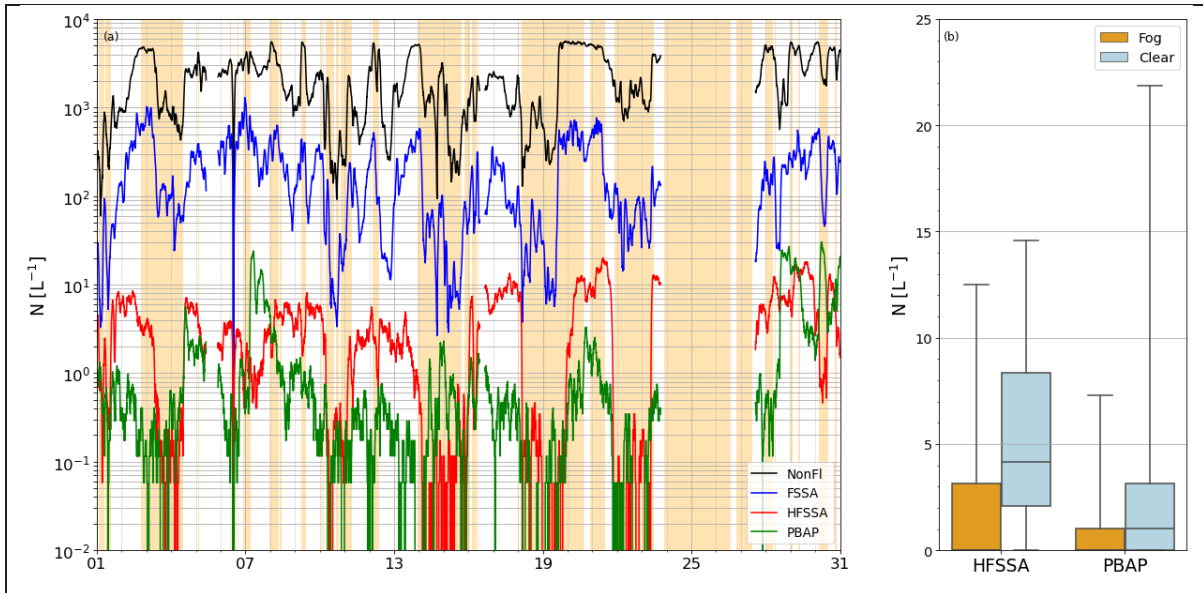


Figure F-2: (a) MBS aerosol concentrations N from 01-31 July based on above characterization. A 3-hourly rolling average has been applied to the 5-minute integrated timeseries for clarity. Shading shows fog periods identified by (1-min averaged) visibility < 1 km. (b) A box and whisker plot showing the impact of fog on the HFSSA and PBAP classes. Whiskers denote 5th and 95th percentile.

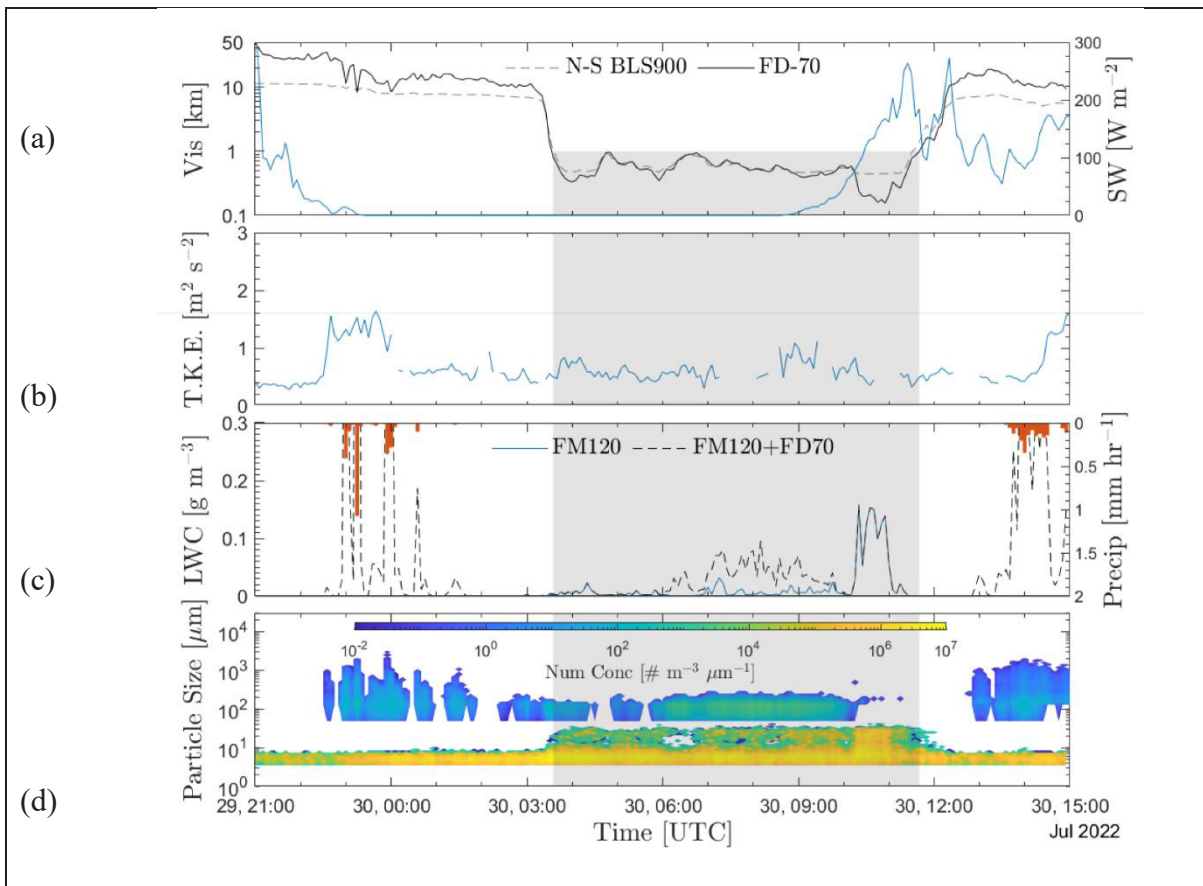


Figure G-1: (a) Timeseries of visibility from FD70 and BLS900 scintillometer along with net SWR (blue). SWR and FD70 were both near the Center tower while scintillometer gave a spatially integrated measurement from the North tower to the South tower. Thus, a disparity between FD70 and BLS900

indicate hydrometeor inhomogeneities. (b) Time series of TKE from the 8-m level at the Center tower. (c) LWC calculated from FM120 as well as the combined LWC from the FM120 and FD70. Red indicates precipitation from FD70. (d) Timeseries of droplet size distribution from FD70 and FM120. Gray highlighted area denotes persistent fog. Note that the number concentration from FD70 is only an estimate, which should be viewed with circumspection along with the corresponding LWC retrievals.

Appendix G: Homogeneity of Fog Across SI and Monitoring Droplet Evolution

Useful microphysical and visibility data that supplement meteorological information in Fig. 9 pertinent to a cloud-lowering fog event is given in Fig. G1.

Appendix H: A Brief Overview of COAMPS® Modeling

Coupled Ocean Atmosphere Mesoscale Prediction System (COAMPS®) was used in real-time to support Fatima-GB, wherein 48-hour forecasts were launched four times a day at 00, 06, 12 and 18 UTC. The numerical setup for the Sable Island utilized three nested domains with decreasing horizontal grid spacing from 9 to 1 km, as shown in Fig. H1. In the vertical direction, there were 23 model levels in the lowest 1 km, starting at 3 m close to the surface, then increasing with height, for a total of 68 layers with the model top at 28 km. The time step for the coarsest mesh was 30 s. The grids encompassing the position of R/V-Condor was also evaluated.

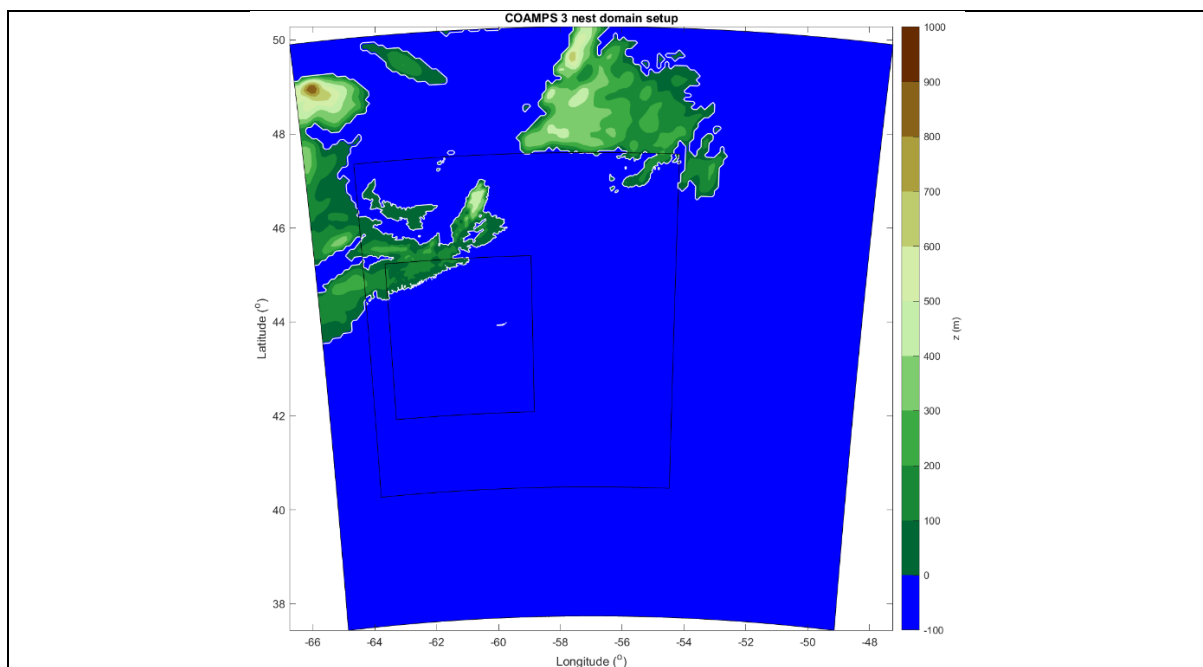


Figure H-1: COAMPS® nests (9, 3, and 1 km) over the Northwestern Atlantic, centered over Sable Island, used for the real time support of Fatima-GB

COAMPS® is a fully compressible, non-hydrostatic limited area model developed and used operationally by the US Navy (Hodur 1997). The initial and lateral boundary conditions for COAMPS® were provided using GFS fields. The sea surface temperature gradient between

the Labrador Current and Gulfstream that plays an important role in fog life cycle is relatively stationary during each forecast (not shown), justifying not coupling the ocean component in COAMPS[®]. The SST was captured by the data assimilation cycle, and provided as the bottom boundary condition for the atmospheric component of COAMPS[®].

Appendix I: Satellite Evidence of Fog Shadow

Brightness Temperature Difference (BTD) fields observed by specific wavelength channels of satellites can be used to roughly identify smaller water droplets (and hence fog or stratus) in the lower atmosphere (Amani et al. 2020). This property was exploited to identify Sable Island's fog shadow in the images of GOES-18 satellite shown in Fig. I-1. Fog shadow extends well beyond the spatial resolution limits of GOES-18.

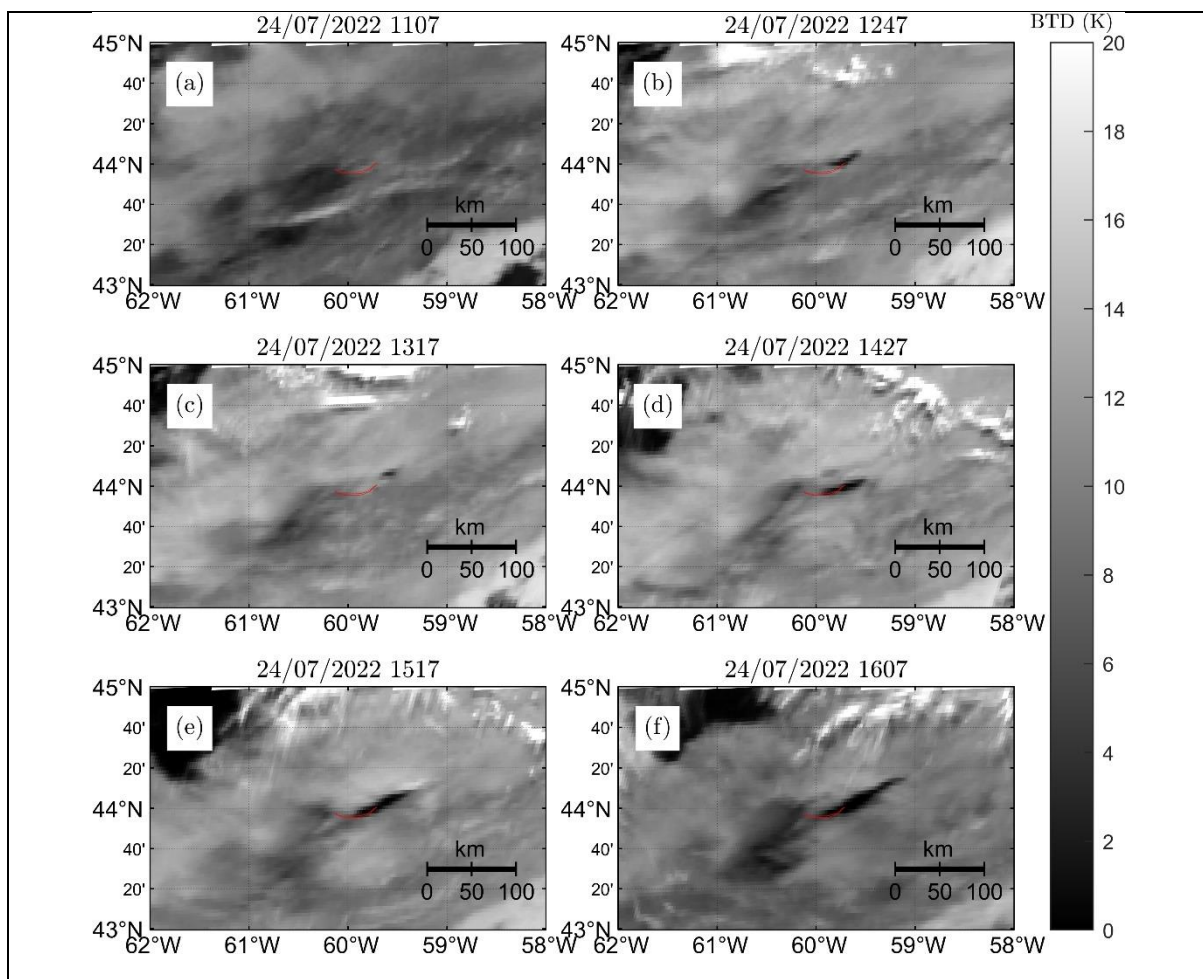


Figure I-1: BTD calculated based on $(10.35 \mu\text{m} - 3.9 \mu\text{m})$ wavelength channels of GOES-18 satellite observed in the vicinity of Sable on July 24, 2022 (IOP10) at different observation times; see Bardeel et al. (2024). The times of images are shown on the top in ADT (Atlantic Daylight Time). A region of improved visibility appears after 1200 ADT on 24 July (dark region) in the lee (northeast) of Sable that persists, with varying intensities, at least until 1600 ADT. The dark region that extends ~ 30 km downstream can be construed as the 'fog shadow' predicted by COAMPS[®].

Appendix J: Simulating Fog Dynamics via Coupled Modeling

LES resolves turbulent eddies down to the scale of grid-size, and provides insights into much smaller microscale conditions that govern the lifecycle of fog. Following Fatima-GB, LES coupled with LSD and LCM models (dubbed L^3) helped understand and predict microscale dynamics of fog. L^3 solves the following governing equations numerically using a finite-difference spatial discretization and second-order time integration. The role of each term is identified beneath the curly brackets.

$$\frac{\partial \tilde{u}_i}{\partial t} = \underbrace{-\tilde{u}_j \frac{\partial \tilde{u}_i}{\partial x_j}}_{\text{resolved}} - \underbrace{\frac{1}{\rho_0} \frac{\partial \tilde{p}}{\partial x_i}}_{\text{pressure}} - \underbrace{\frac{\partial \tau_{ij}}{\partial x_j}}_{\text{subgrid}} + \underbrace{\delta_{i,3} \frac{\tilde{\theta}_v - \langle \tilde{\theta}_v \rangle}{\tilde{\theta}_v}}_{\text{buoyancy}} + \underbrace{\varepsilon_{ij3} f(\tilde{u}_j - \langle u_{g,j}^{LS} \rangle)}_{\text{Coriolis}} - \underbrace{\left\langle u_j^{LS} \frac{\partial u_i^{LS}}{\partial x_j} \right\rangle}_{\text{LS advection}} - \underbrace{\langle w^{LS} \rangle \frac{\partial \tilde{u}_i}{\partial z}}_{\text{LS subsidence}} + \underbrace{\frac{1}{\tau_n} (\langle u_i^{LS} \rangle - \langle \tilde{u}_i \rangle)}_{\text{relaxation}} + \underbrace{\frac{1}{\rho_a} S^m}_{\text{source}} \quad (J1)$$

$$\frac{\partial \tilde{\phi}}{\partial t} = \underbrace{-\tilde{u}_j \frac{\partial \tilde{\phi}}{\partial x_j}}_{\text{resolved}} - \underbrace{\frac{\partial \pi_j}{\partial x_j}}_{\text{subgrid}} - \underbrace{\left\langle u_j^{LS} \frac{\partial \phi^{LS}}{\partial x_j} \right\rangle}_{\text{LS advection}} - \underbrace{\langle w^{LS} \rangle \frac{\partial \tilde{\phi}}{\partial z}}_{\text{LS subsidence}} + \underbrace{\frac{1}{\tau_n} (\langle \phi^{LS} \rangle - \langle \tilde{\phi} \rangle)}_{\text{relaxation}} + \underbrace{\frac{1}{\rho_a} S^h}_{\text{source}} \quad (J2)$$

Here, \tilde{u}_i is the filtered velocity and θ_v the virtual potential temperature. $\tilde{\phi}$ is a generic scalar, which can be either the potential temperature ($\tilde{\theta}$) or the total specific humidity (\tilde{q}). The large-scale advective tendencies and subsidence and the Coriolis term that accounts for the large-scale pressure gradients are the LSD terms. A relaxation term is introduced as a safeguard, nudging the LES toward a true mean state. A dynamic subgrid-scale (SGS) model developed by Germano et al. (1991) is used for modeling SGS stresses. The LCM model addresses the interaction between fog droplets and the background flow, providing a detailed representation of fog formation and growth processes.

The size of the computational domain used to simulate the Hibernia area, a locality covered by R/V-Condor, is 500 m x 500 m x 500 m in the x, y and z (upward) directions, respectively. This domain is divided into 128 x 128 x 128 grid points with 3.9 m grid spacing in each direction. Periodic boundary conditions are applied horizontally, while at the bottom surface the Monin-Obukhov similarity theory defines surface conditions with a roughness length of 3.2×10^{-5} m. The ocean surface is forced by SST derived from ERA5, updated hourly,

and specific humidity is adjusted to maintain 100% relative humidity at the surface. The large-scale tendencies are derived from ERA5 and interpolated on the LES grid. The relaxation time is set to 1 hour. For the LCM, the initial aerosol distribution is based on the C-FOG campaign data (Fernando et al. 2021) and includes accumulation and coarse modes with peaks at 0.1 μm and 1 μm with hygroscopicities of 0.6 and 1.2, respectively.

Appendix K: Instrumentation for Fatima-GB

Instruments and instrument systems used in Fatima-GB are given below.

Table K1: Instrumentation on R/V Atlantic Condor

Instrument	Manufacturer & Model	Measurement	Location	Institution
Microwave Rain Radar (MRR)	METEK MRR-PRO	Vertical profiling of droplet size distribution, rain rate and liquid water content	On ship	UND
Vertical Microstructure Profiler (VMP)	Rockland Scientific Uprising VMP-250	Ocean microstructure, turbulent kinetic energy dissipation evaluation	On ship	UND
Optical Disdrometer	Eigenbrodt ODM 470	Rain drop or snow particle size distribution	On ship	UND
Remote Ocean Sensing Radiometer (ROSR)	Remote Measurements & Research Co.	Sea-surface skin temperature (SSST)	On ship	UND
Microwave Radiometer	Radiometrics MP-3000A	Vertical profile of temperature, water vapor and liquid water	On ship	UND
Visible and Cloud/IR Cameras	Moonglow Technologies SKY Camera; FLIR DUO Pro R IR Thermal Camera	Full color video view of the entire sky; real-time image capture plus MSX multi-spectral imaging enhancement	On ship	UND
Visibility and Present Weather Detection (PWD) Sensor	Vaisala FD70	Meteorological condition code and MOR (visibility), rain drop or snow particle size distribution	On ship	UND
Ceilometer-CL61	Vaisala CL61	Vertical profiles of aerosol backscatter with depolarization; precipitation, differentiation between solid, liquid and mixed-phase clouds	On ship	UND
Scanning Doppler Lidar	Halo Photonics Streamline Allsky	Profiles of Doppler velocity and fluctuations, aerosol backscatter	Motion-Stabilized Platform	UND
W-Band FMCW Cloud Radar	Radiometric Physics RPG-FMCW-94-DP-G1	Vertical profiles of Reflectivity, Doppler Velocity, 2.2 mm wavelength, range resolution 1 m, information of scatterers (rain, clouds, snowflakes, fog)	Motion-Stabilized Platform	UND
CTD	SeaBird SBE 25plus	Conductivity, Temperature and Depth sensors, and	On ship	UND/MEOPAR

		auxiliary sensors — dissolved oxygen, pH, fluorescence, oil, radiance, light transmission, turbidity, nitrates		
300 kHz ADCP	Teledyne Workhorse	Ship mounted, bottom referenced velocity and current profile measurement	On ship	UND/MEOPAR
Sea Snake	Built by NOAA (YSI 46040 precision thermistor in a custom-fabricated floating hose)	Sea surface temperature at ~ 3-5 cm below sea surface	On ship	UND/PSL-NOAA
3D Ultrasonic Anemometer	Gill Gill R3A	3D wind velocity (@20Hz at 18.6m above the surface	(Ship) Bowmast	PSL-NOAA/UND
Fast Water Vapor Infrared Gas Analyzer	LiCOR 7500A	Water vapor (@10Hz) at 18m above the surface	Bowmast	PSL-NOAA/UND
Weather Transmitter	Vaisala WXT520	Temperature, RH, pressure, rain and wind speed/direction (@ 1Hz) at 18m above the surface	Bowmast	PSL-NOAA/UND
GPS Heading System	Hemisphere Crescent VS100	GPS coordinates	Bowmast	PSL-NOAA/UND
HMP Pressure Sensor	Vaisala	Pressure at 16.25 m above the surface	Bowmast	PSL-NOAA/UND
Pyrgeometers	Eppley PIR	Downwelling longwave radiative flux (on the bridge at ~ 16-17 m height)	Bowmast	PSL-NOAA/UND
Pyrometers	Kipp & Zonen CM22 and CMP22	Downwelling shortwave radiative flux (on the bridge at ~ 16-17 m height)	Bowmast	PSL-NOAA/UND
Moored Wave Buoy	Sofar Ocean, Spotter	Ocean wave directional spectra and bulk wave statistics (significant wave height, direction, period), bulk water temperature	3 km south of Sable Island	NPS
Rawinsonde (Vaisala MW41)	Vaisala DigiCORA MW41 Sounding System	Upper air soundings of temperature, relative humidity, pressure, wind speed and wind direction	Off ship	NPS
Ocean Surface and Scene Visualization Cameras	1x Campbell Scientific Field Camera, 2x InVid Technology Bullet Cameras	Optical/Infrared images (full motion video and stills)	On ship	NPS
Integrated CO2 and H2O Open-Path Gas Analyzer and 3-D Sonic Wind Anemometer	Campbell Scientific IRGASON	Perturbation of three-dimensional wind vector, sonic air temperature, H2O/CO2 gas concentration	C-CAMS and D-CAMS	NPS
Dual Antenna GNSS-Aided Inertial Navigation System	VectorNav VN-300	Platform motion (GNSS position, velocity, attitude)	C-CAMS and D-CAMS	

Humidity and Temperature Probe	Vaisala HMP155	Bulk temperature and relative humidity	CCAMS and D-CAMS	NPS
Fast-Response Barometer	Paroscientific MET4A	Pressure perturbation w/ aspirated temperature and relative humidity	C-CAMS	NPS
Upwelling Infrared Pyrometer	Heitronics CT15.85	Radiometric sea surface temperature (9.6 - 11.6 um)	C-CAMS and D-CAMS	NPS
Net Radiometer	Apogee SN-500-SS	Net longwave and shortwave radiation	C-CAMS	NPS
Radar Altimeter	Ainstein US-D1	Surface elevation	C-CAMS	NPS
Soot Photometer	Brechtel Tricolor Absorption Photometer (TAP)	Aerosol absorption (red, green, blue)	C-CAMS	NPS
Portable Optical Particle Spectrometer	Handix Scientific POPS	Aerosol size spectra (120 nm - 3 um)	C-CAMS	NPS
Visibility and Present Weather Detection (PWD) Sensor	Campbell Scientific CS-125	Infrared forward-scattering meteorological optical range (visibility)	C-CAMS and D-CAMS	NPS
Fog Monitor	Droplet Measurement Technologies FM120	Droplet size spectra (2 - 50 microns)	C-CAMS and D-CAMS	NPS
3-Wavelength Integrating Nephelometer	EcoTech Aurora 3000	Aerosol scattering (red, green, blue)	On ship	AFIT/NPS
Black Carbon Aethalometer	Magee Scientific AE33	Aerosol absorption (7 wavelength, UV-NIR)	On ship	AFIT/NPS
(Water-based) Condensation Particle Counter	Aerosol Devices MAGIC210 CPC	Aerosol number concentration (5nm - 2.5 um), moderated aerosol growth with internal water cycling, condensation particle counter	On ship	AFIT/NPS
Pygeometer	Apogee SL-510, SL-610	Longwave down- and upwelling radiation	TLS Mounted on ship	UU
Optical Particle Counter (OPC)	AlphaSense OPC-N3 model	PM1, PM2.5, PM10 and particle size distribution (0.35 to 40 um with 24 bins)	TLS Mounted on ship	UU
Fog Water Collector	Caltech Active Strand Cloud Water Collector 2	Droplets > 3.5 um	On ship	DU
Scanning Mobility Particle Sizer (SMPS)	TSI Inc. 3938 Differential-Mobility Analyzer 3081 + Electrostatic Classifier 3082 + Condensation Particle Counter 3772	Submicrometer particle size distribution: Aerosol size spectra 10 - 500 nm	On ship	DU
Aerodynamic Particle Sizer (APS)	TSI Inc. 3321	Aerosol size spectra (0.36 to 13 um)	On ship	DU
Fog Monitor	DMT FM120	Droplet size spectra (2um - 50 um)	On ship	DU
Back-Scatter Cloud Probe	DMT BCP	Particle size distribution (5um to 75 um)	Gondola	OntTechU

Cloud Droplet Probe	DMT CDP-2	Particle size distribution (2um to 50 µm)	Gondola	OntTechU
Micro Orifice Uniform Deposit Impactor (MOUDI)	Model 100-NR, MSP Corp (A TSI Company), Shoreview, MN	0.1-10 µm, aerosol during fog	On ship	YorkU
Nano-MOUDI-II	Model 122-R, MSP Corp (TSI)	0.01-10 µm, ambient aerosol	On ship	YorkU
Ion Chromatograph	Thermo Scientific ICS-6000	Aerosol major anions and cations	On ship	YorkU
Gas Monitors	Ecotech EC9841, EC9830, S10, S40	CO, NO, NO ₂ , total reactive nitrogen, NH ₃ , and O ₃	On ship	YorkU
Fog Monitor	DMT FM-120	Droplet size spectra (2um - 50 um)	A/V Wallace	Scripps/UCSD
Flux Mast (sonics)	Gill R3-50 (x2)	3D wind speed & fluxes	A/V Wallace	Scripps/UCSD
Towed CTD	RBR Concerto	Ibid, Dissolved Oxygen, Fluorometer	A/V Wallace	Scripps/UCSD
500 Hz ADCP (downward looking)	Nortek Signature 500	Current profiler	A/V Wallace	Scripps/UCSD
Visible and IR 360 Camera	ASV	Surface IR and visible imagery	A/V Wallace	Scripps/UCSD
X-Band Radar	Furuno	X-Band backscatter	A/V Wallace	Scripps/UCSD
3D Ultrasonic Anemometer	Gill R3-50	3D winds and fluxes	Wave Gliders (x3)	Scripps/UCSD
Weather Station	Vaisala WXT530	Temperature, RH, pressure, rain and wind speed/direction (@ 1Hz)	Wave Gliders (x3)	Scripps/UCSD
CTD	Seabird GPCTD	Ibid, at the surface and sub depth (~8-9m)	Wave Gliders (x3)	Scripps/UCSD
300 KHz ADCP	Teledyne Workhorse	Ibid, Current profile	Wave Gliders (x3)	Scripps/UCSD
Upward-Looking Current Profiler	Nortek Signature 1000	Upward-looking current profiler at 8m depth	Wave Gliders (x3)	Scripps/UCSD
Dual GPS Receiver	Hemisphere V104	Position, platform velocity, and directional wave spectra	Wave Gliders (x3)	Scripps/UCSD
CTD	RBR Concerto installed on profiling Winch	Ibid, profiling from 8m to 150m depth (installed on only one Wave Glider)	Wave Gliders (x3)	Scripps/UCSD
GPS-IMU	Novatel SPAN OEM7720 GPS Receiver with Dual GPS Antennas and Epson EG320N IMU	Position, platform attitude and velocity, directional wave spectra	Wave Gliders (x3)	Scripps/UCSD

Table K2: Instrumentation on Sable Island

Instrument	Manufacturer & Model	Measurement	Institution
Visibility and Present Weather Detection (PWD) Sensor	Vaisala FD70	Ibid	UND

Visibility and Present Weather Detection (PWD) Sensor	Vaisala PWD22	Meteorological condition code and MOR (meteorological optical range, or visibility)	UND
Scanning Doppler Lidar	Halo Photonics Streamline Allsky	Ibid	UND
Super Combo Probe	In-House Built (miscellany of hotwire and nanowire sensors aligning with the wind to capture dissipation scales)	High frequency measurement of wind velocity and temperature fluctuations with resolution approaching dissipation scales	UND
Net Radiometers	Campbell Scientific CNR1 Net Radiometer	Net LW/SW radiation	UND
Fast Water Vapor Infrared Gas Analyzer	LI-COR LI-7500A	Ibid	UND
Sonic Anemometers	Gill Gill R3A	ibid	UND
Fine Wire T/Relative Humidity Sensors	Vaisala HMP45C	Temperature and RH	UND
Ceilometer-CL31	Vaisala CL31	Vertical profiles of aerosol backscatter	UND
Microwave Radiometer (MWR)	Radiometrics MP-3000A	ibid	NPS
Wind Profiling Monostatic Sodar	Scintec SFAS	Vertical profiles of wind speed/direction and structure function parameter of temperature (10-500 m)	NPS
Scintillometer	Scintec BLS 900	Fried parameter (r_0), structure function parameter of index of refraction (C_n^2)	NPS
Differential Imaging Motion Monitor	NAWCWD China Lake - DIMM	Fried parameter (r_0), structure function parameter of index of refraction (C_n^2)	NPS
Wide Angle Teleradiometric Transmissometer	NAWCWD China Lake - WATT	Optical transmission	NPS
Non-coherent Extended Source Beacon	NAWCWD China Lake - NESB	Shortwave IR transmitter for DIMM/WATT systems	NPS
Rawinsonde (Vaisala MW41)	Vaisala DigiCORA MW41 Sounding System	Upper air soundings of temperature, relative humidity, pressure, wind speed and wind direction	NPS
Tethered Lifting System (TLS); Balloon and Winch	Allsopp Helikite DS25	Lifting meteorological payload to various elevations	NPS
Visibility and Present Weather Sensor	Campbell Scientific CS-120	Infrared forward-scattering meteorological optical range (visibility)	NPS
Cloud Droplet Probe (CDP) on communication tower	DMT CDP-2	ibid	NPS
Transmissometer	Vaisala LT31	Optical transmission	NPS
Differential Temperature Sensor (DTS)	Omega Type-E Thermocouple	Structure function parameter of temperature (CT_2) from 3 unequally spaced fast-response thermocouples	NPS
Integrated CO ₂ and H ₂ O Open-Path Gas Analyzer and 3-D Sonic Wind Anemometer	Campbell Scientific IRGASON	Ibid	NPS
Video Cameras	Axis Communications M30 Dome Camera	Visual documentation of environmental conditions	NPS

Microwave Rain Radar (MRR)	METEK MRR-PRO	Ibid	UU
Ceilometer-CL31	Vaisala CL31	Ibid	UU
EM Scintillometer (TX and RX: Transmitter and Receiver)	Scintec BLS-900#1TX, BLS-900#1RX,	Atmospheric turbulence, heat flux and crosswind	UU
Microwave Scintillometer (MWS)	Radiometer Physics RPG-MWSC-160 (TX and RX)	Sensible and latent Heat Fluxes	UU
Precision Radiation Balance Sawhorse	CGR4 pyrgeometers, CMP21 pyranometers, up- and downwelling; in-house built	4 components of SW, LW and net radiation	UU
Pyrgeometer (on TLS)	Apogee SL-510, SL-610	Longwave down- and upwelling radiation	UU
Optical Particle Counter	Alphasense OPC	PM1, PM2.5, PM10 and particle size distribution (0.35 to 40 μm with 24 bins N3)	UU
Visibility Cameras (Webcams)	Microseven 5MP	Time lapse photos (1 per minute)	UU
LWC Probes	in house built	liquid water content	UU
Self-Calibrating Soil Heat Flux Sensor	Hukseflux HFP01SC	Soil heat flux	UU
30 cm Soil Moisture and Temperature Sensor	Campbell Scientific CS650	Soil moisture and temperature	UU
Averaging Soil Thermocouple Probe	Campbell Scientific TCAV	Soil temperature	UU
Visibility and Present Weather Sensor	Campbell Scientific CS125	Infrared forward-scattering meteorological optical range (visibility)	UU
LEMS (automated weather station)	In-house assembled	T, RH, wind speed and direction, soil T, surface T, SW and OPC-N3 (0.38 - 17 μm with 24 bins)	UU
Ceilometer	Vaisala CL51	Vertical profiles of aerosol backscatter	OntTechU
Weather Transmitter	Vaisala WXT520	Ibid	OntTechU
Visibility and Present Weather Detection (PWD) Sensor	Vaisala PWD52	Meteorological condition code and MOR (visibility) and rain	OntTechU
Fog Monitor	DMT FM120	Ibid	OntTechU
Ground Cloud Imaging Probe (GCIP)	DMT	Particle size spectra (7.5 μm to 960 μm)	OntTechU
Young 3D Sonic Anemometer (Model 81000)	R.M. Young Company	Horizontal and vertical wind speed and direction and turbulence, 20Hz	OntTechU
Sunshine Pyranometer	Delta-T Devices SPN1	Global (Total) and diffuse irradiance; DNI (Direct Normal Irradiance) calculation	OntTechU
Digital Camera	General	Local pictures looking at the south	OntTechU
CINCS (Cloud Ice Nucleation Characterization System)	Aerosol Devices, Inc.	Bioaerosols tens of nm, possibly of fog/ice condensation nuclei nature	AFIT/NPS
Multi-parameter Bioaerosol Spectrometer (MBS-MR)	University of Hertfordshire	Ultraviolet-light induced fluorescence spectrometer; Primary bioaerosol particles, detection range 0.5-15 μm	UMAN

Table K3: Instrument Systems on R/V Atlantic Condor

System	Location	Institution
Bow Mast	Ship bow	PSL-NOAA/UND
C-CAMS	Crane operated (ship)	NPS
D-CAMS	Deck mounted on ship	NPS
Tethered System+Payload Lifting	Ship and Sable Island	ARL/UU/UND
Gondola	Ship (fixed)	OntTechU
Instrument Wave Glider	Launched from Ship	SCRIPPS/UCSD
R/V Wallace: Autonomous Boat Instrumented for Air-Sea Interaction Research	Launched from Ship	SCRIPPS/UCSD
Flux Towers (Appendix C)	Sable Island	UND/UU
LEMS	Sable Island	UU
Motion Stabilized Doppler Lidar	Ship	UND
Motion Stabilized W-Band Radar	Ship	UND
Super Combo Probe	Sable Island	UND
Radiation Balance Sawhorse	Sable Island	UU
Instrumented UAV (Unmanned Aerial Vehicle)	Sable Island/2 weeks	OntTechU
Microphysical Tower	Sable Island	OntTechU

Appendix L: Commonly Encountered Acronyms

(For acronyms for instruments, see Appendix K)

ABL – Atmospheric Boundary Layer

AGL – Above Ground Level

a.s.l – above sea level

BTD – Brightness Temperature Difference

COAMPS - Coupled Ocean/Atmosphere Mesoscale Prediction System

CTD – Conductivity, Temperature, Depth

DWR – Downwelling Radiation (Irradiance)

ERA5 – Fifth generation ECMWF atmospheric reanalysis

FCN – Fog Condensation Nuclei

FSSA – Fluorescent Sea Spray Aerosols

GFS – Global Forecast System

HFSSA – Highly Fluorescent Sea Spray Aerosols

IBL – Internal Boundary Layer

IOP/ISP – Intense Operational (or Study) Period

K – Kolmogorov

L3 – Coupling of LES, LSD and LCM

LCM – Lagrangian Cloud Model

LES – Large Eddy Simulations
LSD – Large Scale Dynamics
LEMS – Local Energy Budget Measurement System
LWC – Liquid Water Content
LWR – Long Wave Radiation
MABL – Marine Atmospheric Boundary Layer
MSLP – Measured Sea Level Pressure
MVD – Mean Volume Diameter
NWP – Numerical Weather Prediction Model
Nd – Aerosol Number Concentration
O-C – Obukhov-Corrsin Scale
PBAP – Primary Biological Aerosol Particles
RH – Relative Humidity
SLOP – Sable Lee Observing Period
SSA – Sea Surface Aerosols
SST – Sea Surface Temperature
SWR – Short Wave Radiation (Irradiance)
T – Temperature
TKE – Turbulent Kinetic Energy
WRF (ARW) – Weather Research and Forecasting Model (Advanced Research ARW)
WS and WD – Wind Speed and Direction

References:

- Amani, M., Mahdavi, S., Bullock, T. and Beale, S., 2020: Automatic nighttime sea fog detection using GOES-16 imagery. *Atmos. Res.*, 238, 104712.
- Bardoel, S., Hoch, S., Ruiz-Placarte, J., Lenain, L., Gultepe, I., Grachev, A., Gaberšek, S., Wang, Q., and Fernando, H.J.S., 2024: Study of fog dissipation in an internal boundary layer on Sable Island. *Quart. J. Roy. Meteor. Soc.*, Accepted.
- Balendra, S., Kale, A., Pongetti, J., Kazemimanesh, M., Haugen, M., Weller, L. and Boies, A., 2024: Condensation particle counters: Exploring the limits of miniaturization. *J. Aerosol Sci.*, 175, 106266.
- Barve, A., Gultepe, I., Fernando, H.J.S., Wang, Q., and Shen, L., 2024: Large Scale Dynamics · Large-Eddy Simulation · Lagrangian Cloud Modeling (L3) Coupling for Studying the Marine Fog Life Cycle. *Quart. J. Roy. Meteor. Soc.*, Accepted

- Bertram, T.H., Cochran, R.E., Grassian, V.H. and Stone, E.A., 2018: Sea spray aerosol chemical composition: elemental and molecular mimics for laboratory studies of heterogeneous and multiphase reactions. *Chem. Soc. Rev.*, 47(7), 2374-2400.
- Bhushan, B., 2020: Design of water harvesting towers and projections for water collection from fog and condensation. *Phil. Tran. Roy. Soc. A*, 378(2167), 20190440.
- Boutle, I., Price, J., Kudzotsa, I., Kokkola, H. and Romakkaniemi, S., 2018: Aerosol–fog interaction and the transition to well-mixed radiation fog. *Atmos. Chem. Phys.*, 18(11), 7827-7840.
- Chen, F., and Dudhia, J., 2001: Coupling an advanced land surface–hydrology model with the Penn State–NCAR MM5 modeling system. Part I: Model implementation and sensitivity. *Mon. Wea. Rev.*, 129, 569–585. [https://doi.org/10.1175/1520-0493\(2001\)129<0569:CAALSH>2.0.CO;2](https://doi.org/10.1175/1520-0493(2001)129<0569:CAALSH>2.0.CO;2).
- Chisholm, N., Nagare, B., Wainwright, C., Creagan, E., Salehpoor, L., VandenBoer, T.C., Bullock, T., Croft, B., Lesins, G., Osthoff, H. and Fernando, H.J.S., 2021: Characterizing Atmospheric Aerosols off the Atlantic Canadian Coast During C-FOG. *Bound. Layer Meteorol.*, 181, 345-364.
- Crawford, I., Topping, D., Gallagher, M., Forde, E., Lloyd, J.R., Foot, V., Stopford, C., and Kaye, P., 2020: Detection of Airborne Biological Particles in Indoor Air Using a Real-Time Advanced Morphological Parameter Uv-Lif Spectrometer and Gradient Boosting Ensemble Decision Tree Classifiers. *Atmos.*, 11, 1039.
- Crawford, I., Bower, K., Topping, D., Di Piazza, S., Massabò, D., Vernocchi, V., and Gallagher, M., 2023: Towards a UK Airborne Bioaerosol Climatology: Real-Time Monitoring Strategies for High Time Resolution Bioaerosol Classification and Quantification. *Atmos.*, 14, 1214. <https://doi.org/10.3390/atmos14081214>
- Crilley, L.R., Lao, M., Salehpoor, L. and VandenBoer, T.C., 2023: Emerging Investigator Series: An instrument to Measure and Speciate the Total Reactive Nitrogen Budget Indoors: Description and Field Measurements. *Environ. Sci.: Processes & Impacts*, 25(3), 389-404.
- Deng, Z., Ran, L., Xu, X., Yan, P., Tian, P., Lin, W., Wu, Y., Zhang, R., Pan, W. and Lu, D., 2024: Size-resolved Cloud Condensation Nuclei Activity of Aerosol Particles Sampled Above the Mixing Layer. *Aero. Sci. Tech.*, 1-13.
- Dimitrova, R., Sharma, A., Fernando, H.J.S., Gultepe, I., Danchovski, V., Wagh, S., Bardoel, S.L., and Wang, S., 2021: Simulations of Coastal Fog in the Canadian Atlantic with the

- Weather Research and Forecasting Model. *Boundary-Layer Meteor.*, 181, 443–472.
<https://doi.org/10.1007/s10546-021-00662-w>.
- Dorman, C.E., Mejia, J., Koraćin, D. and McEvoy, D., 2020: World marine fog analysis based on 58-years of ship observations. *Intl. J. Climatol.*, 40(1), 145-168.
- Dorman, C.E., Mejia, J., Koraćin, D. and McEvoy, D., 2017: Worldwide marine fog occurrence and climatology. *Marine fog: Challenges and Advancements in Observations, Modeling, and Forecasting*, 7-152, Springer.
- Dudhia, J., 1989: Numerical Study of Convection Observed During the Winter Monsoon Experiment using a Mesoscale Two-Dimensional Model. *J. Atmos. Sci.*, 46(20), 3077–3107. [https://doi.org/10.1175/1520-0469\(1989\)046<3077:NSOCOD>2.0.CO;2](https://doi.org/10.1175/1520-0469(1989)046<3077:NSOCOD>2.0.CO;2).
- Fairall, C.W., Bradley, E.F., Hare, J.E., Grachev, A.A., and Edson, J.B., 2003: Bulk Parameterization of Air-Sea Fluxes: Updates and Verification for the COARE Algorithm. *J. Climate*, 16, pp 571-591.
- Farmer, D.K., Boedicker, E.K. and DeBolt, H.M., 2021: Dry deposition of atmospheric aerosols: Approaches, observations, and mechanisms. *Ann. Rev. Phys. Chem.*, 72, 375-397.
- Fathalli, M., Lac, C., Burnet, F. and Vié, B., 2022: Formation of Fog due to Stratus Lowering: An Observational and Modelling Case Study. *Quar. J. Roy. Meteor. Soc.*, 148(746), 2299-2324.
- Fernando, H.J.S., Gultepe, I., Dorman, C., Pardyjak, E., Wang, Q., Hoch, S., Richter, D., Creegan, E., Gaberšek, S., Bullock, T., Hocut, C., Chang, R., Alappattu, D., Dimitrova, R., Flagg, D., Grachev, A., Krishnamurthy, R., Singh, D.K., Lozovatsky, I., Nagare, B., Sharma, A., Wagh, S., Wainwright, C., Wroblewski, M., Yamaguchi, R., Bardeel, S., Coppersmith, R., Chisholm, N., Gonzalez, E., Gunawardena, N., Hyde, O., Morrison, T., Olson, A., Perelet, A., Perrie, W., Wang, S., and Wauer, B., 2021: C-FOG: Life of Coastal Fog. *Bull. Amer. Meteor. Soc.*, 102(2).
- Freitas, G.P., Stolle, C., Kaye, P.H., Stanley, W., Herlemann, D.P.R., Salter, M.E., and Zieger, P., 2022: Emission of Primary Bioaerosol Particles from Baltic Seawater. *Environ. Sci. Atmos*, 2, 1170–1182.
- Gaberšek, S., Gapp, N., Fernando, H.J.S., Ruiz-Plancarte, J., Ortiz-Suslow, D.G., Wang, Q., Pardyjak E., Hoch, S., Gultepe, I., and Dorman C., 2024: Fog clearing in the lee of an isolated, flat island: A fog shadow. *Quart. J. Roy. Meteor. Soc.*, Submitted.
- Gautam, R. and Singh, M.K., 2018: Urban heat island over Delhi punches holes in widespread fog in the Indo-Gangetic Plains. *Geophys. Res. Letts.* 45(2), 1114-1121.

- Ge, X., Zhang, Q., Sun, Y., Ruehl, C.R. and Setyan, A., 2012: Effect of aqueous-phase processing on aerosol chemistry and size distributions in Fresno, California, during wintertime. *Env. Chem.*, 9(3), 221-235.
- Gerber, H.E., 1981: Microstructure of a radiation fog. *J. Atmos. Sci.*, 38(2), 454-458.
- Goldschmidt, V.W. and Householder, M.K., 1969: The Hot Wire anemometer as an Aerosol Droplet Size Sampler. *Atmos. Env.*, 3(6), pp.643-651.
- Grare, L., Statom, N.M., Pizzo, N. and Lenain, L., 2021: Instrumented wave gliders for air-sea interaction and upper ocean research. *Front. Marine Sci.*, 8, 664728.
- Greenfield, S.M., 1957: Rain scavenging of radioactive particulate matter from the atmosphere. *J. Atmos. Sci.*, 14, 115–125. [https://doi.org/10.1175/1520-0469\(1957\)014<0115:RSORPM>2.0.CO;2](https://doi.org/10.1175/1520-0469(1957)014<0115:RSORPM>2.0.CO;2)
- Grell, G. A. and Freitas, S. R., 2014: A Scale and Aerosol Aware Stochastic Convective Parameterization for Weather and Air Quality Modeling, . *Atmos. Chem. Phys.*, 14, 5233–5250. <https://doi.org/10.5194/acp-14-5233-2014>.
- Gultepe, I., Müller, M.D. and Boybeyi, Z., 2006: A new visibility parameterization for warm-fog applications in numerical weather prediction models. *J. App. Meteor. Climatol.* 45(11): 1469–1480.
- Gultepe, I., Pearson, G., Milbrandt, J.A., Hansen, B., Platnick, S., Taylor, P., Gordon, M., Oakley, J.P. and Cober, S.G., 2009: The fog remote sensing and modeling field project. *Bull. Amer. Meteor. Soc.*, 90, 341–359
- Gultepe, I., Fernando, H.J.S, Pardyjak, E.R., Hoch, S.W., Silver, Z., Creegan, E., Leo, L.S., Pu, Z., De Wekker, S.F.J., and Hang, C., 2016: An Overview of the MATERHORN Fog Project: Observations and Predictability. *Pure App. Geophys.*, 173 (9), 2983–3010.
- Gultepe, I., Heymsfield, A.J., Fernando, H.J.S., Pardyjak, E., Dorman, C.E., Wang, Q., Creegan, E., Hoch, S.W., Flagg, D.D., Yamaguchi, R. and Krishnamurthy, R., 2021: A review of coastal fog microphysics during C-FOG. *Bound. Layer Meteor.*, 181, 227-265.
- Hintz, T.J., Huang, K.Y., Hoch, S.W., Bardoel, S.L., Gaberšek, S., Gultepe, I., Ruiz-Plancarte, J., Pardyjak, E.R., Wang, Q. and Fernando, H.J.S, 2024: A mechanism for coastal fog genesis at evening transition. *Quart. J. Roy. Meteor. Soc.*, 150(762), 2727-2743.
- Hersbach, H., Bell, B., Berrisford, P., Biavati, G., Horányi, A., Muñoz Sabater, J., Nicolas, J., Peubey, C., Radu, R., Rozum, I., Schepers, D., Simmons, A., Soci, C., Dee, and D.,

- Thépaut, J.-N. 2023: ERA5 Hourly Data on Pressure Levels from 1940 to Present. *Copernicus Climate Change Service (C3S) Climate Data Store (CDS)*.
- Hong, S.Y., Noh, Y., and Dudhia, J., 2006: A New Vertical Diffusion Package with an Explicit Treatment of Entrainment Processes. *Mon. Wea. Rev.*, 134, 2318–2341. <https://doi.org/10.1175/MWR3199.1>.
- Hodur, R. M., 1997: The Naval Research Laboratory's Coupled Ocean/Atmosphere Mesoscale Prediction System (COAMPS). *Mon. Wea. Rev.*, 125, 1414–1430.
- Huang, S., Hu, W., Chen, J., Wu, Z., Zhang, D., and Fu, P. 2021: Overview of biological ice nucleating particles in the atmosphere. *Environ. International*, 146, 106197.
- Huang, Kelly, Hintz, T., and Kit, E., and Fernando, H.J.S., 2024: An Equilibrium Radius of Fog Droplets in Turbulent Environments, *In preparation*.
- Isaac, G.A., Bullock, T., Beale, J. and Beale, S., 2020: Characterizing and Predicting Marine Fog Offshore Newfoundland and Labrador. *Wea. Forecast.*, 35(2), 347-365.
- Jiménez, P.A., Dudhia, J., Gonzalez-Rouco, J.F., Navarro, J., Montavez, J.P., Garcia-Bustamante, E., 2012: A revised scheme for the WRF surface layer formulation. *Mon. Wea. Rev.*, 140, 898-918.
- Jumper, E.J. and Gordeyev, S., 2017: Physics and Measurement of Aero-Optical Effects: Past and Present. *Ann. Rev. Fluid Mech.*, 49, 419-441.
- Jung, J., Furutani, H., Uematsu, M., Kim, S. and Yoon, S., 2013: Atmospheric inorganic nitrogen input via dry, wet, and sea fog deposition to the subarctic western North Pacific Ocean. *Atmos. Chem Phys*, 13(1), 411-428.
- Karimi, M., 2020: Direct Numerical Simulation of Fog: The Sensitivity of a Dissipation Phase to Environmental Conditions. *Atmos.*, 11(1), 12 doi:10.3390/atmos11010012.
- Kecorius, S., Hoffmann, E.H., Tilgner, A., Barrientos-Velasco, C., van Pinxteren, M., Zeppenfeld, S., Vogl, T., Madueño, L., Lovrić, M., Wiedensohler, A. and Kulmala, M., 2023: Rapid growth of Aitken-mode particles during Arctic summer by fog chemical processing and its implication. *PNAS nexus*, 2(5), 124.
- Kit, E., Hocut, C.M., Liberzon, D. and Fernando, H.J.S., 2017: Fine-scale turbulent bursts in stable atmospheric boundary layer in complex terrain. *J. Fluid Mech.*, 833, 745-772.
- Köhler, H., 1936: The Nucleus in and the Growth of Hygroscopic Droplets. *Trans. Faraday Soc.*, 32, 1152-1161.
- Koračin, D. and Dorman, C.E. eds., 2017: *Marine fog: Challenges and Advancements in Observations, Modeling, and Forecasting*. Springer.

- Koračin, D., Lewis, J., Thompson, W.T., Dorman, C.E. and Businger, J.A., 2001: Transition of Stratus into Fog along the California Coast: Observations and Modeling. *J. Atmos. Sci.*, 58(13), 1714-1731.
- Koračin, D., Dorman, C.E., Lewis, J.M., Hudson, J.G., Wilcox, E.M. and Torregrosa, A., 2014: Marine Fog: A Review. *Atmos. Res.*, 143, 142-175.
- Knopf, D.A., Alpert, P.A. and Wang, B., 2018: The Role of Organic Aerosol in Atmospheric Ice Nucleation: A Review. *ACS Earth and Space Chem.*, 2(3), 168-202.
- Leipper, D.F., 1994: Fog on the U.S. West Coast, a Review. *Bull. Amer. Meteor. Soc.*, 72, 229–240.
- Lakra, K. and Avishek, K., 2022: A Review on Factors Influencing Fog Formation, Classification, Forecasting, Detection and Impacts. *Rendiconti Lincei. Scienze Fisiche e Naturali*, 33(2), 319-353.
- Lozovatsky, I., Wainwright, C., Creegan, E., and Fernando, H.J.S., 2021: Ocean Turbulence and Mixing near the Shelf Break Southeast of Nova Scotia, *Bound. Layer Meteor.*, 181, 425–441, <https://doi.org/10.1007/s10546-020-00576-z>
- MacDonald, M., Kurowski, M.J. and Teixeira, J., 2020: Direct numerical simulation of the moist stably stratified surface layer: Turbulence and Fog Formation. *Bound. Layer Meteor.*, 175(3), 343-368.
- Mansell, E.R., Ziegler, C. L., and Bruning, E. C., 2010: Simulated electrification of a small thunderstorm with two-moment bulk microphysics. *J. Atmos. Sci.*, 67(1), 171-194, <https://doi.org/10.1175/2009JAS2965.1>.
- Meng, Z. and Seinfeld, J.H., 1994: On the Source of the Submicrometer Droplet Mode of Urban and Regional Aerosols. *Aero. Sci. Tech.*, 20(3), 253-265.
- Mlawer, E.J., Taubman, S.J., Brown, P.D., Iacono, M.J., and Clough, S.A., 1997: Radiative transfer for inhomogeneous atmospheres: RRTM, a validated correlated-k model for the longwave. *J. Geophys. Res.: Atmos.*, 102(D14), 16663–16682, <https://doi.org/10.1029/97JD00237>.
- Myers, J.N., 1968: Fog, *Sci. Amer.*, 219(6), 74-83.
- Nakanishi, M., 2000: Large-eddy Simulation of Radiation Fog. *Bound. Layer Meteor.*, 94(3), 461–493.
- Nakanishi, M., and Nino, H., 2006: An improved Mellor_Yamada level-3 model: its numerical stability and application to a regional prediction of advection fog. *Bound. Layer Meteor.*, 119, 397–407, <https://doi.org/10.1007/s10546-005-9030-8>.

- Niece, M., and Kaiser, C., 2018: Directed Energy Outreach. *Proc. Directed Energy Educational Outreach Campaign*, Directed Energy Professional Society, 11, <https://www.deps.org/DEPSpages/DEoutreach.html>
- NWS 2024: Super Fog, <https://www.weather.gov/safety/fog-super> (Accessed Apr 25, 2024)
- Ortiz-Suslow, D., Ruiz-Plancarte J., Yamaguchi R., Kalogiros, J., Fernando, H.J.S, Creegan, E., Pardyjack, E., Gaberšek, S., Gultepe, I., and Wang, Q., 2024: A Case Study of Boundary Layer Development Downstream of a Small Maritime Island, *Quart. J. Roy. Meteor. Soc.*, Submitted.
- Pawlak, R.J., 2012: Recent developments and near term directions for Navy laser weapons system (LaWS) testbed. *High-Power Lasers 2012: Technology and Systems* (Vol. 8547, p. 854705). International Society for Optics and Photonics. <https://doi.org/10.1117/12.976031>.
- Perram, G.P., Cusumano, S.J., Hengehold, R.L., and Fiorino, S.T., 2010: *An introduction to laser weapon systems*. Hard back Textbook, 463 Pages, Directed Energy Professional Society.
- Place, B.K., Young, C.J., Ziegler, S.E., Edwards, K.A., Salehpoor, L. and VandenBoer, T.C., 2018. Passive sampling capabilities for ultra-trace quantitation of atmospheric nitric acid (HNO₃) in remote environments. *Atmos. Environ.*, 191, 360-369.
- Poku, C., Ross, A.N., Blyth, A.M., Hill, A.A. and Price, J.D., 2019: How important are aerosol–fog interactions for the successful modelling of nocturnal radiation fog? *Wea.*, 74(7), 237-243.
- Pollard, R., Rhines, P., and Thompson, R., 1972: The Deepening of the Wind-Mixed Layer. *Geophys. Fluid Dyn.*, 4(4), 381–404. <https://www.tandfonline.com/doi/abs/10.1080/03091927208236105>
- Pruppacher, H.R. and Klett, J.D., 2010: Microstructure of atmospheric clouds and precipitation. *Microphys. Clouds and Precip.*, 10-73. Springer, Dordrecht.
- Pu, Z., Pardyjak, E.R., Hoch, S.W., Gultepe, I., Hallar, A.G., Perelet, A., Beal, R., Carrillo-Cardenas, G., Li, X., Garcia, M. and Oncley, S., 2023: Cold Fog Amongst Complex Terrain. *Bull. Amer. Meteor. Soc.*, 104(11), E2030-E2052.
- Richter, D.H., MacMillan, T. and Wainwright, C., 2021: A Lagrangian Cloud Model for the Study of Marine Fog. *Bound. Layer Meteor.*, 1-20.
- Rodhe, B., 1962: The Effect of Turbulence on Fog Formation. *Tellus*, 14(1), 49-86.

- Salehpoor, L. and VandenBoer, T.C., 2023: Suppressor and calibration standard limitations in cation chromatography of ammonium and 10 alkylamines in atmospheric samples. *Analy. Methods*, 15(31), 3822-3842.
- Sasakawa, M., Ooki, A. and Uematsu, M., 2003: Aerosol size distribution during sea fog and its scavenge process of chemical substances over the northwestern North Pacific. *J. Geophys. Res.: Atmos.*, 108(D3).
- Schiffer, J.M., Mael, L.E., Prather, K.A., Amaro, R.E. and Grassian, V.H., 2018: Sea Spray Aerosol: Where Marine Biology Meets Atmospheric Chemistry. *ACS Central Sci.*, 4(12), 1617-1623.
- Shin, H H., and Hong, S.Y., 2015: Representation of the Subgridscale Turbulent Transport in Convective Boundary Layers at Gray-Zone Resolutions. *Mon. Wea. Rev.*, 143, 250–271, <https://doi.org/10.1175/MWR-D-14-00116.1>.
- Skamarock, W.C., Klemp, J.B., Dudhia, J., Gill, D.O., Barker, D., Duda, M.G., Huang, X., Wang, W., and Powers, J. G., 2008: A Description of the Advanced Research WRF Version 3. NCAR Tech Rep (NCAR/TN-475+STR), University Corporation for Atmospheric Research, <http://dx.doi.org/10.5065/D68S4MVH>.
- Singh, D.K., Hoch, S.W., Gultepe, I. and Pardyjak, E.R., 2024: A Case study of the Life Cycle of a Stratus-Lowering Coastal-Fog Event in Newfoundland, Canada. *Quart. J. Roy. Meteor. Soc.*, 150(759), 641-662.
- Soveizi, N., Latifi, A.M., Mehrabian, S. and Akhavan Sepahi, A., 2023: Bacterial Ice Nucleation Proteins: Features, Structure, and Applications. *J. App. Biotech. Rep*, 10(3), 1041-1054.
- Spirig, R., Vogt, R., Larsen, J.A., Feigenwinter, C., Wicki, A., Franceschi, J., Parlow, E., Adler, B., Kalthoff, N., Cermak, J. and Andersen, H., 2019: Probing the Fog Life Cycles in the Namib Desert. *Bull. Amer. Meteor. Soc.*, 100(12), 2491-2507.
- Taylor, G.I., 1917: The Formation of Fog and Mist. *Quart. J. Roy. Meteor. Soc.*, 43, 241–268.
- Theethai J., A., Jayakumar, A., Gupta, K., Mohandas, S., Hendry, M.A., Smith, D.K., Francis, T., Bhati, S., Parde, A.N., Mohan, M. and Mitra, A.K., 2023: Implementation of the urban parameterization scheme in the Delhi model with an improved urban morphology. *Quart. J. Roy. Meteor. Soc.*, 149(750), 40-60.
- Torregrosa, A., O'Brien, T.A., and Faloon, I.C., 2014: Coastal Fog, Climate Change, and the Environment. *Eos Trans. AGU*, 95(50), 473–474.
- Vladimirov, E., Dimitrova, R., and Danchovski, V., 2018: Sensitivity of WRF Model Results to Topography and Land Cover: Study for the Sofia Region. *Annuaire de l'Université*

- de Sofia "St. Kliment Ohridski", Faculté de Physique*, **111**, 87-101, https://www.phys.uni-sofia.bg/annual/archive/111/full/GSU-Fizika-111_07_color.pdf.
- Van der Hoven, I., 1957: Power Spectrum of Horizontal Wind Speed in the Frequency Range from 0.0007 to 900 cycles per hour. *J. Atmos. Sci.*, *14*(2), 160-164.
- Van der Velde, I. R., Steeneveld, G. J., Schreur, B. W., and Holtslag, A. A. M., 2010: Modeling and Forecasting the Onset and Duration of Severe Radiation Fog under Frost Conditions. *Monthly Wea. Rev.*, *138*(11), 4237-4253.
- Wagh, S., Krishnamurthy, R., Wainwright, C., Wang, S., Dorman, C.E., Fernando, H.J.S. and Gultepe, I., 2021: Study of Stratus-lowering Marine-Fog Events Observed During C-FOG. *Bound. Layer Meteor.*, *181*, 317-344.
- Wu, S., Tao, J., Ma, N., Kuang, Y., Zhang, Y., He, Y., Sun, Y., Xu, W., Hong, J., Xie, L., Wang, Q., Su, H., and Cheng, Y., 2022: Particle number size distribution of PM1 and PM10 in fogs and implications on fog droplet evolutions. *Atmos. Environ.*, *277*, 119086. <https://doi.org/10.1016/j.atmosenv.2022.119086>.
- WMO, 1992: *International Meteor. Vocabulary*. WMO, Geneva, Switzerland.
- Yamaguchi, R., Ruiz-Plancarte, J., Ortiz-Suslow, D. G., Chang, R., Creegan, E. D., Fernandez, D., Kalogiros, J. A., Fernando, H. J. and Wang, Q., 2024: A shipboard atmospheric surface layer profiling system for air-sea interaction and fog studies. In Preparation for *Quart. Jour. Royal Meteor. Soc.*
- Zhao, S., Yan, J., Lin, Q., Yao, L., Park, K., Jung, J., Chen, L., Xu, S., Sun, M., Wang, S. and Yang, H., 2022. Changes in aerosol particle composition during sea fog formation events in the sea ice regions of the Arctic Ocean. *Atmos. Environ.*, *272*, 118943.6.